Experimental studies of the neutron and proton electromagnetic structure functions

A. Bodek,* M. Breidenbach,† D. L. Dubin, J. E. Elias,‡ J. I. Friedman, H. W. Kendall, J. S. Poucher,§ E. M. Riordan,‖ and M. R. Sogard¶

Physics Department and Laboratory for Nuclear Science, Massachusetts Institute of Technology, Cambridge, Massachusetts 02139

D. H. Coward and D. J. Sherden

Stanford Linear Accelerator Center, Stanford University, Stanford, California 94305

(Received 23 March 1979)

We have carried out an experimental study of the neutron and proton deep-inelastic electromagnetic structure functions. The structure functions were extracted from electron-proton and electron-deuteron differential cross sections measured in three experiments spanning the angles 6°, 10°, 15°, 18°, 19°, 26°, and 34°. We report primarily on the large-angle (15°–34°) measurements. Neutron cross sections were extracted from the deuteron data using an impulse approximation. Our results are consistent with the hypothesis that the nucleon is composed of pointlike constituents. The variation of the cross section with angle suggests that the hypothetical constituents have spin 1/2. The data for σ_n/σ_p, the ratio of the neutron and proton differential cross sections, are in the range 0.25 to 1.0, and are within the limits imposed by the quark model. Detailed studies of the structure functions were made for a range of the scaling variable ω from $\omega = 1.3$ to $\omega = 10.0$, and for a range of invariant four-momentum transfer Q^2 from 1.0 to 20.0 GeV^2. These studies indicate that the structure functions approximately scale in the variable ω, although significant deviations from scaling in ω are apparent in the region $1.3 < \omega < 3.3$. These deviations from scaling are in the same direction and of similar magnitude for both neutron and proton. The interpretation of the data in terms of various theoretical models is discussed.

I. INTRODUCTION

Over the last two decades, the electron has proved to be a highly effective probe of the small-distance structure of the nucleon. As the electromagnetic interaction of the electron is explicitly calculable in quantum electrodynamics,[1] electron-nucleon (e-N) scattering experiments can be unambiguously interpreted in terms of the structure of the probed nucleon. In the latter half of the 1950's the elastic electron-proton (e-p) and quasi-elastic electron-deuteron (e-d) scattering experiments of Hofstadter and collaborators[2] indicated that the proton and neutron had finite sizes of order 10^{-13} cm. Electron-nucleon scattering experiments[3,4] of the middle 1960's established that the nucleon form factors fell rapidly with increasing momentum transfer, suggesting a composite picture of the nucleon. In 1969, results from the first small-angle inelastic e-p scattering experiment[5] at the Stanford Linear Accelerator Center (SLAC) suggested that the proton was composed of hypothetical pointlike constituents.[6] The approximate scaling of the proton structure functions, verified by that experiment and a large-angle inelastic e-p experiment[7] in the region of momentum and energy transfers significantly greater than the proton mass, provided the most straightforward and convincing evidence for this hypothesis. The large-angle experiments reported here repeat the earlier large-angle e-p experiment[7] with improved statistical accuracy and expanded kinematic range; inelastic e-d scattering is also measured for the first time over this expanded kinematic range. These experiments used the SLAC 8-GeV spectrometer and complement an earlier small-angle inelastic e-p and e-d scattering experiment[8] done at SLAC. The data gathered in these experiments permit a detailed comparison of the inelastic electron-proton and electron-neutron (e-n) scattering cross sections. More stringent tests of structure-function scaling are also facilitated by more complete and accurate data for the nucleon structure functions, as defined below.

In these experiments, an electron of incident energy E scatters from a nuclear target through a laboratory angle θ to a final energy E', and only the electron is detected in the final state. In the first Born approximation, the scattering occurs through the exchange of a single virtual photon (Fig. 1) of energy $\nu = E - E'$ and invariant momentum transfer $q^2 = -4EE' \sin^2\theta/2 = -Q^2$, where $\hbar = c = 1$ has been used and the mass of the electron

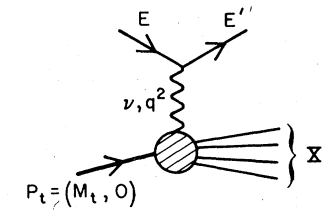

FIG. 1. Feynman diagram for inelastic electron-nucleon scattering in the first Born approximation.

has been neglected. The hadronic final state is unknown except for the invariant mass $W=(M^2+2M\nu-Q^2)^{1/2}$, where M is the proton mass. The differential cross section for electron scattering from the nuclear target is related to the two structure functions W_1 and W_2 according to[9]

$$\frac{d^2\sigma}{d\Omega dE'}(E,E',\theta)=\sigma_M[W_2(\nu,Q^2)+2W_1(\nu,\theta^2)\tan^2\theta/2], \tag{1.1}$$

where

$$\sigma_M=\frac{4\alpha^2E'^2}{Q^4}\cos^2\frac{\theta}{2}$$

is the Mott cross section, and $\alpha=e^2/4\pi=\frac{1}{137}$. The structure functions W_1 and W_2 are similarly defined by Eq. (1.1) for the proton, deuteron, or neutron; they summarize all the information about the structure of these particles obtainable from unpolarized electron scattering.

Within the single-photon-exchange approximation, one may alternatively view inelastic electron scattering as virtual photoproduction. Here, as opposed to photoproduction by real photons, the photon mass q^2 is variable and the exchanged photon may have a longitudinal as well as a transverse polarization. If the final-state hadrons are not observed, the interference between these two components averages to zero, and the differential cross section for inelastic electron scattering is related to the total cross sections for absorption of transverse, σ_T, and longitudinal, σ_L, virtual photons according to[10]

$$\frac{d^2\sigma}{d\Omega dE'}(E,E',\theta)=\Gamma[\sigma_T(\nu,Q^2)+\epsilon\sigma_L(\nu,Q^2)], \tag{1.2}$$

where

$$\Gamma=\frac{\alpha}{4\pi^2}\frac{KE'}{Q^2E}\left(\frac{2}{1-\epsilon}\right),$$

$$\epsilon=[1+2(1+\nu^2/Q^2)\tan^2\theta/2]^{-1},$$

and

$$K=\frac{W^2-M^2}{2M}.$$

The quantity Γ is the flux of transverse virtual photons and ϵ is the degree of longitudinal polarization. Throughout this paper M and M_D are, respectively, the proton and deuteron masses. The cross sections σ_T and σ_L are related to the structure functions W_1 and W_2 by

$$W_1(\nu,Q^2)=\frac{K}{4\pi^2\alpha}\sigma_T(\nu,Q^2),$$

$$W_2(\nu,Q^2)=\frac{K}{4\pi^2\alpha}\left(\frac{Q^2}{Q^2+\nu^2}\right)[\sigma_T(\nu,Q^2)+\sigma_L(\nu,Q^2)]. \tag{1.3}$$

In the limit $Q^2\to 0$, one obtains $\sigma_L\to 0$ and $\sigma_T\to\sigma_\gamma(\nu)$, where $\sigma_\gamma(\nu)$ is the photoproduction cross section for real photons. The quantity R, defined as the ratio σ_L/σ_T, is related to the structure functions by

$$R(\nu,Q^2)\equiv\frac{\sigma_L}{\sigma_T}=\frac{W_2}{W_1}\left(1+\frac{\nu^2}{Q^2}\right)-1. \tag{1.4}$$

Equations (1.2) through (1.4) apply equally well for the proton, deuteron, or neutron.

A separate determination of the two inelastic structure functions W_1 and W_2 (or, equivalently, σ_L and σ_T) requires values of the differential cross section at several values of the angle θ for fixed ν and Q^2. According to Eq. (1.2), σ_L is the slope and σ_T is the intercept of a linear fit to

$$\Sigma=\frac{1}{\Gamma}\frac{d^2\sigma}{d\Omega dE'}(\nu,Q^2,\theta).$$

The structure functions W_1 and W_2 are then directly calculable from Eq. (1.3). Alternatively, one can extract W_1 and W_2 from a single differential-cross-section measurement by inserting a particular functional form for R in the equations

$$W_1=\frac{1}{\sigma_M}\frac{d^2\sigma}{d\Omega dE'}\left[(1+R)\left(\frac{Q^2}{Q^2+\nu^2}\right)+2\tan^2\frac{\theta}{2}\right]^{-1},$$

$$W_2=\frac{1}{\sigma_M}\frac{d^2\sigma}{d\Omega dE'}\left[1+\left(\frac{2}{1+R}\right)\left(\frac{Q^2+\nu^2}{Q^2}\right)\tan^2\frac{\theta}{2}\right]^{-1}. \tag{1.5}$$

The striking feature of the earlier inelastic e-p data[5,7] was the scaling of the proton structure functions. Prior to those experiments, Bjorken had conjectured[11] that W_1 and W_2 might become functions of a single dimensionless variable x, i.e.,

$$2MW_1(\nu,Q^2)\to F_1(x),\quad \nu W_2(\nu,Q^2)\to F_2(x), \tag{1.6}$$

in the limit $\nu\to\infty$ and $Q^2\to\infty$, with $x=1/\omega=Q^2/2M\nu$ held fixed. The earlier inelastic e-p experiments[7] showed that approximate scaling behavior occurs at surprisingly nonasymptotic values of $Q^2\geq 1.0$ GeV^2 and $W\geq 2.6$ GeV. This scaling behavior arises quite naturally from a description of the proton in which the electron scatters from pointlike, quasifree constituents, or partons.[6] In this simple parton model, x is the fraction of the proton's momentum carried by the struck parton in the infinite-momentum frame, and $F_1(x)$ and $F_2(x)$ are unambiguously related to the parton charges and momentum distributions. A number of other models, including Regge-exchange models,[12] vector-meson dominance,[13] and s-channel resonance models[14] can accomodate the observed scaling behavior for at least some range of x and Q^2. Extended parton models[15,16] as well as conventional field theories[17] and asymptotically

free gauge theories,[18] predict small deviations from scaling that would have eluded the earlier inelastic e-p measurements. A more detailed and accurate examination of structure-function scaling, which was one of the objectives of the experiments reported in this paper, can help to distinguish among these hypotheses.

A measurement of the deep-inelastic e-n cross section also is a valuable test of the models that have been proposed to account for the observed scaling of the proton structure functions. Within parton models, predictions for the ratio of neutron to proton cross sections vary according to the assumptions about the parton charges and internal dynamics.[6] A measurement of this ratio, which was the primary objective of these experiments, places constraints upon the possible parton models and other models of nucleon structure. Knowledge of both the neutron and proton cross sections also allows a separate determination of the isovector and isoscalar contributions to the structure functions.

While unbound protons are readily available in liquid hydrogen targets, the simplest available target containing neutrons is deuterium, with a nuclear binding energy of 2.2 MeV. The extraction of neutron cross sections from inelastic e-p and e-d cross sections requires corrections for the effects of the binding of the nucleons in the deuteron. Corrections for the effects of Fermi motion of the nucleons are calculable in an impulse approximation.[19,20] Measurement of inelastic e-p and e-d scattering at identical electron kinematics then permits the calculation of the neutron-to-proton cross-section ratio

$$\frac{\sigma_n}{\sigma_p}=\left(\frac{d^2\sigma}{d\Omega dE'}\right)_n\Big/\left(\frac{d^2\sigma}{d\Omega dE'}\right)_p . \tag{1.7}$$

Within parton models, the behavior of R as a function of Q^2 for fixed x reflects the spin quantum numbers of those charged partons carrying a fraction x of the nucleon's momentum. If the charged partons are purely spin $\frac{1}{2}$, light-cone algebras predict that νR should scale.[6,21,22] For spin-0 partons R itself should scale.[23] The early inelastic e-p measurements[7] showed that R for the proton (R_p) was small and slowly varying, consistent with the constant value 0.18. Within a parton model the small values of R_p measured earlier favored predominantly spin-$\frac{1}{2}$ constituents. However, a convincing test of this hypothesis requires a detailed examination of the kinematic variation of R_p for fixed x. This examination and a comparison of R_p, R_d, and R_n were among the objectives of these experiments.

In summary, a complete picture of the nucleon requires a measurement of the deep-inelastic cross sections for both neutrons and protons. The ratio σ_n/σ_p provides important constraints upon parton models of the nucleon, while R yields information about the spin of the hypothetical constituents. In this paper we report the results of two experiments performed at SLAC in which both electron-proton and electron-deuteron cross sections were measured over wide ranges of E and E' for several scattering angles. Sections II–IV describe the experiments and the methods of analysis used to determine the inelastic e-p and e-d cross sections. Extraction of the inelastic e-n cross sections and the ratio σ_n/σ_p is described in Sec. V. The extraction of R from these cross sections is described in Sec. VI. Tests of structure-function scaling are presented in Sec. VII, and Sec. VIII gives concluding remarks and discussion. Some early results of the two experiments were reported in several Letters,[24,25] and the first experiment is described in detail in two doctoral theses.[20,26]

II. THE EXPERIMENTS

Cross sections for inelastic e-p and e-d scattering were measured over a range of scattering angles in two separate experiments that employed similar experimental apparatus and data analysis methods. Electrons of fixed primary energy were scattered from liquid hydrogen and deuterium targets and were momentum-analyzed in a focusing spectrometer set at fixed scattering angles. A number of momentum spectra, each covering a range of E' for fixed values of E, were measured at each angle to permit model-independent radiative corrections to be made.

In experiment A,[24] cross sections were measured with the SLAC 8-GeV spectrometer at scattering angles of 18, 26, and 34 degrees for primary energies ranging from 4.5 to 18.0 GeV and scattered energies ranging from 1.0 to 8.75 GeV, as shown in Fig. 2. Earlier inelastic e-p cross-

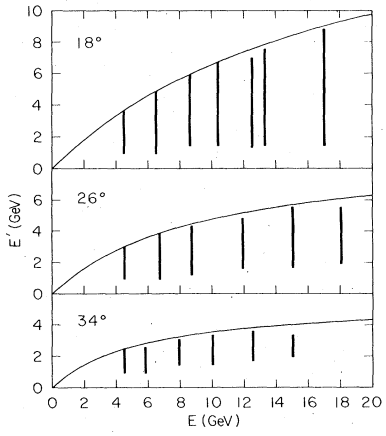

FIG. 2. Ranges of E and E' in experiment A.

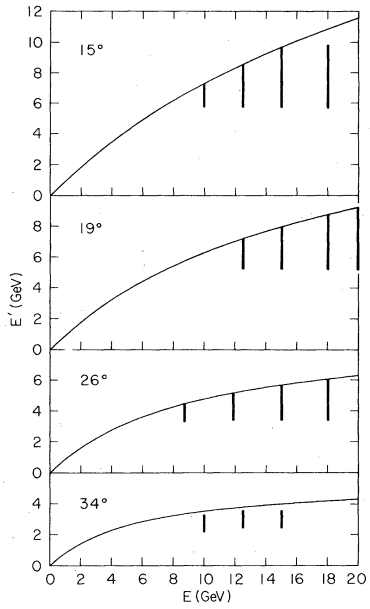

FIG. 3. Ranges of E and E' in experiment B.

section measurements were repeated with improved accuracies. Inelastic e-p and e-d cross sections were measured alternately over the entire kinematic range. Continuous momentum spectra were measured for $W \leq 2.0$ GeV for the three lowest primary energies at 18°; elsewhere cross sections were measured at intervals in E' as large as 0.5 GeV. The momentum transfer Q^2 ranged from 0.5 GeV^2 to 20.0 GeV^2 and W ranged as high as 5.2 GeV in this experiment. In this paper the totality of data for either target measured at a constant scattering angle will be called a "triangle," and a single momentum spectrum at fixed primary energy will be called a "line."

In experiment B,[25] inelastic e-p and e-d cross sections were measured with the 8-GeV spectrometer at scattering angles of 15, 19, 26, and 34 degrees. Primary energies ranged from 8.7 to 20.0 GeV; the ranges of E' measured at each energy and angle are shown in Fig. 3. The momentum transfer Q^2 ranged from 4.0 to 21.8 GeV^2, while W ranged up to 4.1 GeV. This experiment improved the accuracy of the e-p and e-d cross-section measurements for $\omega \leq 2$ at 26° and 34° and provided entirely new data at 15° and 19°. The primary purpose of experiment B was to gain improved accuracy in the measurement of σ_n/σ_p and of the proton, neutron, and deuteron structure functions in the threshold region ($\omega < 2$).

A diagram of the experimental setup is shown in Fig. 4. An essentially monochromatic beam of electrons was focused onto liquid hydrogen and deuterium targets located directly over the spectrometer pivot in end station A. Two precision toroidal charge monitors were used to measure the incident flux, and several fluorescent screen devices served to monitor the beam steering and

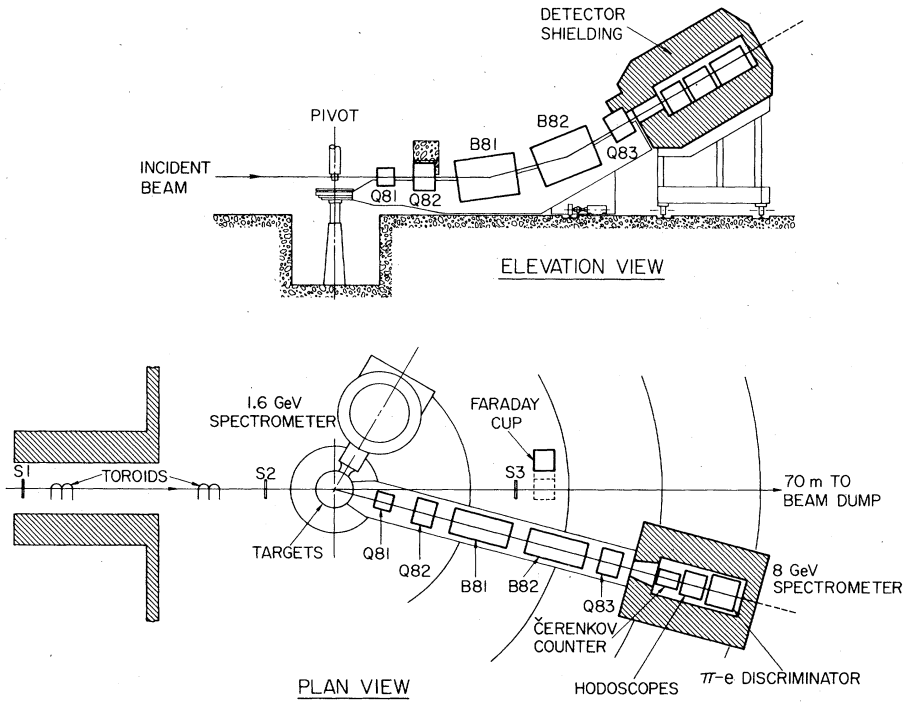

FIG. 4. The experimental setup.

focusing. A remotely movable Faraday cup was periodically inserted into the beam line to calibrate the toroid monitors. The SLAC 1.6-GeV spectrometer, set to detect elastic and quasielastic recoil protons, was used to monitor the target densities. Momentum analysis of the scattered particle flux was accomplished with the SLAC 8-GeV spectrometer set to the desired scattering angle. The focus of the spectrometer was instrumented with trigger counters for event timing and hodoscopes to determine the angle and momentum of the scattered particles. Separation of electrons from the predominantly pion background was accomplished with a threshold Cherenkov detector and a π-e discriminator, which included a multilayered lead-Lucite shower counter and three counters that sampled the early shower development. Signals from the various devices were processed by an on-line SDS 9300 computer, which logged event information from fast electronic logic onto magnetic tape, provided a partial on-line analysis of the data, and monitored the instrumentation during the course of the experiments.

Measured "raw" cross sections were derived from the number of electrons scattered into the spectrometer acceptance for each setting of E, E', and θ. Contributions to the electron yields from the target cell walls were determined using empty replica targets. Measurements with hydrogen, deuterium, and replica targets were interleaved to minimize systematic effects. Contributions from background processes such as π° decay and electron pair production were determined by reversing the spectrometer polarity. Thus the raw cross sections were derived after the contributions from empty target and positrons were subtracted.

Radiative corrections were then applied in two steps to extract the corrected cross sections for inelastic e-p and e-d scattering. In the first step radiative tails from elastic e-p and from elastic and quasielastic e-d scattering were subtracted from the raw e-p and e-d cross sections. Inelastic radiative tails were then calculated and subtracted using a model-independent method. The inelastic e-n cross sections were calculated from the corrected e-p and e-d cross sections, using an impulse-approximation method which included the effects of Fermi motion of the nucleons in the deuteron.

The two structure functions and R were obtained from these cross-section data according to Eqs. (1.1) through (1.5). In order to extend the data to the kinematic region $\omega > 5$, inelastic e-p and e-d cross sections measured with the SLAC 20-GeV spectrometer in an earlier experiment[27,28] (referred to as experiment C) at scattering angles of 6 and 10 degrees were included in the analysis. Separation of the structure functions and R was then possible over the kinematic region $0.1 \leq x \leq 0.8$, with $1 \leq Q^2 \leq 16$ GeV^2 and $1.8 \leq W \leq 5.0$ GeV. The extraction of the structure functions required a careful normalization of these experiments, as all three experiments used different target cells, and experiment C used a different spectrometer. Experiment B was normalized to experiment A by a comparison of the inelastic e-p and e-d cross sections measured at similar E and E' at 26° and 34°. Experiment C was normalized to experiment A by a comparison of the elastic e-p cross sections measured in the two experiments.

The results reported in this paper are derived primarily from the data of experiments A and B. Whenever significant data have been included from experiment C, this fact will be made clear in the text. As the experimental apparatus and data analysis methods of experiments A and B were nearly identical, we report the two experiments in a single paper. In the following two sections, we describe the experimental apparatus and analysis methods of experiment A. Where these differ from those used in experiment B, additional descriptions are included.

III. EXPERIMENTAL APPARATUS

A. Introduction

A detailed description of the experimental apparatus used in experiments A and B is presented in this section. Additional information on the SLAC 8-GeV spectrometer facility may be found in the references describing earlier experiments[7,29] which used this spectrometer.

B. Electron beam and charge monitors

Electrons were accelerated to energies between 4.5 and 18.0 GeV by the Stanford Linear Accelerator,[30] which delivered a maximum of 360 pulses per second to the beam switchyard. The electrons were momentum analyzed, transported to end station A, and focused onto the target cells by the array of magnets and collimators shown in Fig. 5.

Pulsed bending magnets PM1–PM5 deflected electrons 0.5 degrees to the quadrupole doublet Q10-Q11, which imaged the beam profile at the collimator CO upon the energy-defining slits SL10. Two groups of four identical dipole magnets B10–B17 deflected the beam a total of 24 degrees; the first group dispersed the beam for momentum analysis at SL10. The quadrupole magnet Q12 ensured that the beam was achromatic at the target position. The final focusing at the target was pro-

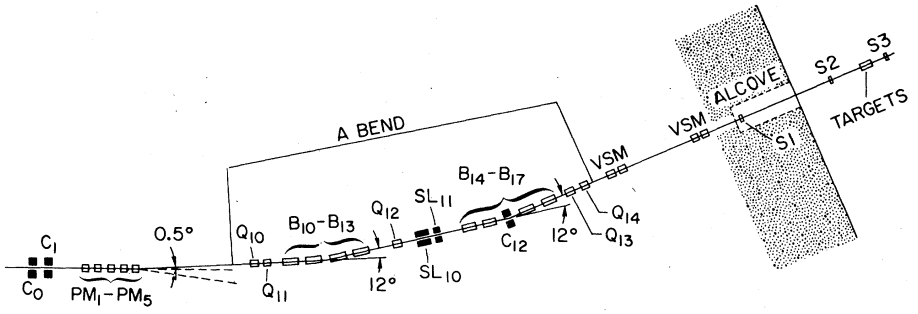

FIG. 5. Beam-line configuration. Notation: B: main bend magnets; C: collimators; PM: pulsed bend magnets; Q: quadrupole magnets; SL: slits; S: fluorescent viewing screens; VSM: vernier steering magnets.

vided by the quadrupole doublet Q13-Q14. Horizontal and vertical vernier steering was obtained from a set of four dipole magnets.

The central energy and total energy spread of the electron beam depended solely upon switchyard parameters and were independent of accelerator performance. Magnet currents in the series string of eight identical dipole magnets B10–B17 were set to the desired values after a standard de-Gaussing cycle. Stability and repeatability of the fields of these magnets were monitored with a rotating-coil field probe located in a ninth identical dipole. This monitor magnet was connected in series with B10–B17, and the "flip-coil" measurements of its field provided a determination of the central beam energy to an absolute accuracy of $\pm 0.1\%$.[30] For each nominal energy the variations in the flip-coil measurements were well below this value. The horizontal opening of the slits SL10 determined the total energy spread of the electron beam. Except for some experimental runs in the resonance region ($W < 2$), a total spread in energy $\delta E/E$ of $\pm 0.25\%$ was allowed. In the resonance region a total energy spread of $\pm 0.1\%$ was used.

The beam halo generated at SL10 was reduced by the collimator C12, consisting of four moveable tungsten jaws followed by four associated ion chambers which monitored beam interactions in the jaws. At each change of incident energy, the four jaws were individually moved into the beam until the corresponding ion chamber indicated 50% of its trip level; the jaw was then moved back 2 mm to prevent frequent beam trips-offs. Experimental runs using a $\frac{1}{8}$-in.- thick aluminum target with a 2-in.-diameter hole about the beam center line showed that singles rates in the trigger counters due to beam halo could be reduced by better than a factor of 2 by using this method. As the distance between two aluminum flanges just above and below the liquid-target cells was approximately 2 inches, these runs provided an estimate of the scattered electron yields from beam halo interactions with the target assembly. Such runs were made frequently at each incident energy, showing nonzero yields only at very low E', where the yields from hydrogen and deuterium are large.

The beam was aligned using the four vernier steering magnets and two zinc-sulfide fluorescent screens (S1 and S2 in Figs. 4 and 5), which were viewed by closed-circuit television monitors. These two screens were rolled out of the beam line after the beam was aligned, while a third screen (S3 in Figs. 4 and 5) remained in the beam line downstream of the target position to monitor the beam steering and beam profile during the experimental runs. Another zinc-sulfide screen included as part of the target assembly was frequently moved into the beam to examine the beam position and profile at the target position. Typically, the profile at the target was an ellipse 2 mm high by 4 mm wide. The uncertainty $\delta\theta$ in the incident electron direction from possible beam misalignment and divergence was ± 0.1 mrad, which is approximately $\frac{2}{3}$ of the angular resolution of the 8-GeV spectrometer.

Two toroidal charge-monitor systems[31] measured the incident charge per pulse and hence monitored the flux of electrons impinging upon the target. The systems each used a ferrite-core toroid encircling the beam coupled directly to a precision capacitor. The wave form produced in this damped resonant circuit by the passage of the electron beam through the central hole in the toroid was amplified and sampled. The sampled signal was digitized and accumulated in a bi-directional accumulator which effectively averaged the noise component of the signal to zero. Each monitor was calibrated internally by discharging a precisely known pulse charge onto a single wire passing through the toroid. Ratios of measured charge to calibrated charge for runs of 10^4 pulses were always within 0.4% of unity. These

internal calibrations were not used to provide an absolute calibration of the monitors, but rather served to monitor gain shifts in the individual monitor systems. The total charge accumulated by the toroid monitor just upstream of the target, when corrected for such gain shifts, gave the electron flux used in the cross-section calculations. The two toroid monitors always agreed to 0.5% or better, and the random error in the flux measured for a run is believed to be ± 0.3%.

Both toroid monitors were periodically calibrated against a Faraday cup[32] which could be moved into the beam at a position 13.5 meters downstream of the target position. Calibration runs were made at representative pulse charges, while pulse repetition rates were limited to 1–10 pulses per second. Ratios of toroid to Faraday-cup measurements in these runs averaged to 0.998 ± 0.005. The results of the Faraday-cup calibrations indicated that the charge accumulated by the downstream toroid monitor gave the electron flux for a run with an absolute uncertainty of ± 0.5%.

Depending upon the counting rate at a given point, beam intensities ranging from 3×10^{10} to 5×10^{11} electrons/pulse were used. A Lucite counter near the target served as a beam-spill monitor. Beam-spill traces viewed on an oscilloscope were kept reasonably flat-topped and had spill widths within the range 1.2–1.6 μsec. Spill-width information as well as the total number of beam pulses was recorded for use in dead-time calculations[20] in the data analysis.

C. Targets and density monitors

The electron beam passed through target cells containing liquid hydrogen or liquid deuterium. As shown in Fig. 6, the two cells were vertical

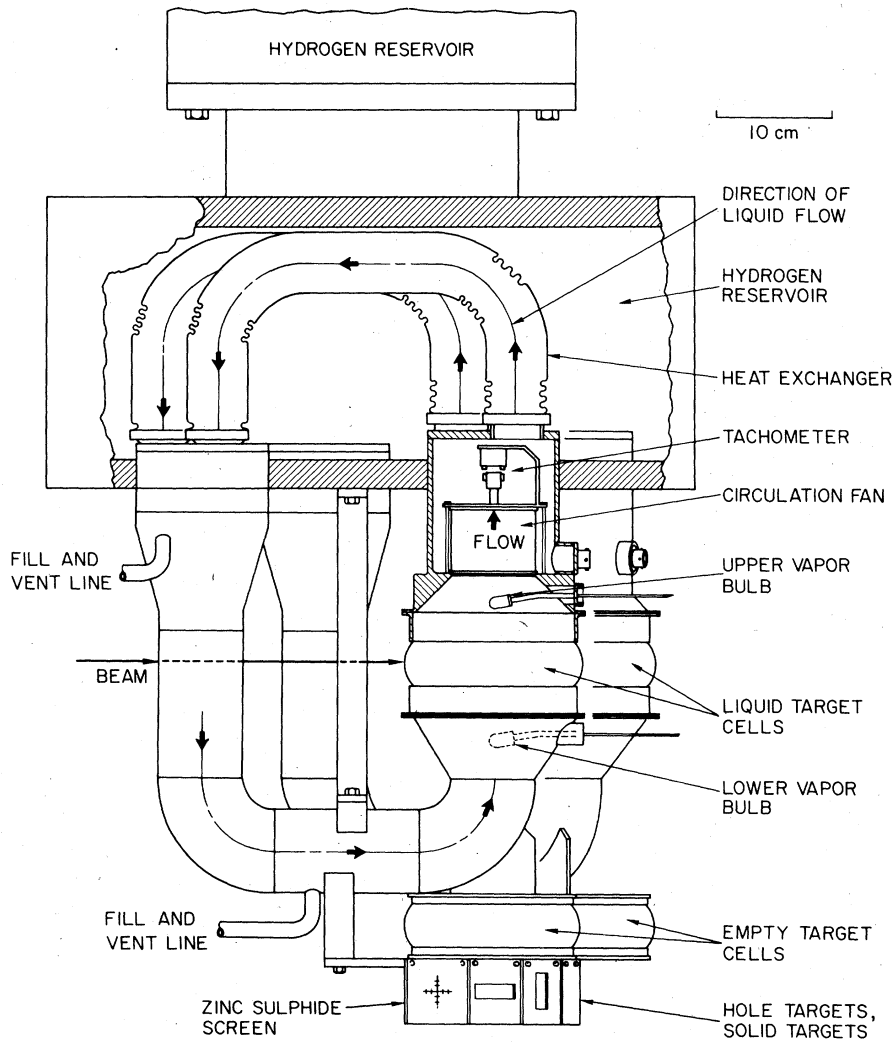

FIG. 6. Target configuration. The array shown here could be rotated about a vertical axis and moved vertically to position the targets available.

cylinders which could be positioned by rotating the entire assembly about its vertical axis so that the beam traversed either cell along a diameter. The cell walls were made of 0.003-in.-thick aluminum for experiment A, and of 0.001-inch-thick stainless steel for experiment B. The length of liquid traversed by the beam was 6.95 cm for hydrogen and 7.12 cm for deuterium in experiment A, and 14.06 cm for hydrogen and 14.11 cm for deuterium in experiment B. Figure 6 shows the target assembly used in experiment B; it was only slightly different from that used in experiment A. Just below each target cell was an empty replica target used for determining cell-wall contributions to the measured cross sections. Below these empty targets was an array of solid targets, the targets having holes of various sizes, and the zinc-sulfide screen. The entire assembly was suspended in a scattering chamber maintained at 10^{-6} Torr. It could be quickly lifted, lowered, or rotated under computer control to bring a specific target into the beam line at its proper position.

Density changes in the liquid targets posed a formidable obstacle that had to be overcome in order to use the high beam currents available at SLAC. The hydrogen and deuterium targets were designed[33] to be cooled by forced convection through closed loops, as shown schematically in Fig. 6. The upper half of each loop formed a heat exchanger in contact with a reservoir of liquid hydrogen at 21° K. Natural convection from beam heating, aided by an electrically driven fan inside each loop, circulated the liquid and presented a fresh segment of liquid to each beam pulse, obviating density changes due to heating by the previous pulse. Test runs showed that the measured scattering yield was independent of beam current and pulse repetition rate (see also Ref. 29), provided the fans were operating. The tachometer shown in Fig. 6 was added to each target for experiment B to give a positive signal that each fan was functioning properly.

The primary target-density monitor employed two hydrogen-vapor-pressure thermometers which indicated the target liquid temperatures above and below the beam line on each of the two target cells. A second density monitor employed the SLAC 1.6-GeV spectrometer[34] which, at each value of E, was set to detect recoil protons from elastic e-p or quasielastic e-d scattering at a fixed recoil-proton momentum and angle. With the target fans operating, the observed changes in the number of protons detected by the 1.6-GeV spectrometer per unit electron flux reflected the known target-density changes as deduced from the small temperature drifts indicated by the upper vapor-pressure thermometer. The hydrogen-target fan operated properly for all the runs of the two experiments. The deuterium-target fan operated properly except for runs at $E = 8.6$, 8.7, 10.4, 11.9, and 13.3 GeV in experiment A.

The target temperatures determined from the upper vapor-pressure thermometer were used in the determination of the target densities for those runs in which the target fans were operating. Conversion tables for liquid temperature to density were readily available from cryogenic data.[35,36] In addition, small corrections (~0.2%) were applied[20] to account for the slow conversion of normal hydrogen to parahydrogen,[36] and for the small change in density resulting from the 1-atm overpressure in the target cells. Similarly, corrections were made for small contaminations (~1%) of HD in the deuterium targets.[20]

Data from the 1.6-GeV spectrometer were used in the determination of the deuterium target density for those runs of experiment A in which the deuterium-target fan was not operating. No such data were available for runs at $\theta = 18°$ and $E = 8.6$ GeV, and no deuteron or neutron cross sections are reported for that line. For each new value of E, normalization runs were made at low beam currents (~3 mA) to ascertain the yield of recoil protons per unit electron flux. Tests had shown that the yield per incident electron at these low currents was independent of whether the target fans were on or off, indicating no significant density changes in the target liquid.[20] Consequently, the density of the target in these normalization runs could be ascertained from the temperature at the upper-vapor-pressure thermometer. The 1.6-GeV-spectrometer proton yield per unit beam flux was then used to monitor the target density in the remaining deuterium runs at that incident energy. Depending upon the instantaneous beam current and repetition rate, target-density corrections at 1%–30% were encountered in those runs in which the deuterium-target fan was not operating. The uncertainty in these corrections is estimated to range from 0.4% to 0.6%.

Careful determination of target lengths and densities was made primarily because the errors in those quantities do not cancel in the ratio of deuterium to hydrogen cross sections and therefore propagate into the error in σ_n/σ_p. Random errors in the effective target density, arising mainly from fluctuations in the beam position and profile, were estimated to be 0.3% in both experiments. The hydrogen target densities were known to an accuracy of ±0.7% in experiment A and ±0.4% in experiment B, with the uncertainty attributable primarily to inaccuracies in the calibration of the vapor-pressure thermometers and a ±0.2% uncertainty in the cryogenic data for liquid hydrogen.

Because the cryogenic data for deuterium are only quoted to an accuracy of ± 0.6%, the deuterium target density was known only to a level of ± 0.9% in experiment A (as long as the fan was operating) and ± 0.7% in experiment B. Target lengths were measured with micrometer calipers, while the targets were warm and pressurized with air. Shrinkage of the targets when cooled to 21° K was surveyed during experiment B, and its effects were included in the calculation of all target lengths. The target lengths were known to ± 0.6% in experiment A and ± 0.4% in experiment B. Samples of gas from the targets were analyzed for purity by mass spectrometry.

Experimental runs with empty replica target cells in the beam line were used to determine the target wall contributions to the measured cross sections. Substantial reductions in running time were realized by using a replica target which had 0.018-in. walls rather than the 0.003-in.-aluminum walls of the liquid targets in experiment A, and 0.0075-in. walls rather than 0.001-in.-stainless-steel walls in experiment B. The extra thickness was selected to simulate the radiative degradation of the electron energy in the full-target liquids.[37] After normalization by the ratio of cell-wall thicknesses, the empty-target background was typically (3–8)% of the full-target yield in experiment A and (2–4)% of the full-target yield in experiment B. The systematic uncertainty in the cross section from uncertainties in target cell-wall thicknesses ranged from 0.1% to 0.6%.

D. Spectrometer

Scattered particles from the target cells were analyzed using the SLAC 8-GeV focusing spectrometer[38-41] shown schematically in Fig. 4. The three quadrupole magnets focused point-to-point in the vertical plane and parallel-to-point in the horizontal plane. The horizontal production angle was displayed in the horizontal focal plane and momentum displayed in the vertical plane. The dipole magnets bent the optic axis a total of 30 degrees in the vertical plane. Scattered particles were delivered to a series of detectors located in a shielded cave just behind Q83. The entire assembly of magnets, detectors, and shielding was supported on a set of rails and could pivot about the target position to the desired scattering angles.

Magnet currents were adjusted under computer control to obtain the desired bending, dispersion, and focusing properties. Small corrections to the magnet currents, established in a series of optics tests[29] allowed the energy of the 8-GeV spectrometer to be normalized to the beam switchyard value for the incident electron energy E. Elastic e-p scattering measured in both experiments indicated that the spectrometer value of E' of the elastically scattered electrons was within 0.05% of the expected value as calculated from E and θ, and this was taken to be the uncertainty in the calibration of E' versus E.

The spectrometer quadrupoles imaged the target at two focal planes located inside the shielded cave. The horizontal-angle, or θ, focal plane was oriented normal to the spectrometer central ray, while the vertical or momentum focal plane was oriented at an angle of 13.7°, as shown in Fig. 7. Two scintillation-counter arrays lying in each focal plane were used to determine the angle, θ, and momentum, P, of a scattered particle. The individual counters overlapped in separate rows to define 54 θ bins and 20 P bins.

Extensive measurements of the optical properties of the 8-GeV spectrometer are described by Kirk *et al.*[29] The detailed calculation of the spectrometer acceptance $\Delta\Omega\Delta P/P$ is presented in Ref. 26 and in Appendix A. The calculation used a TRANSPORT[38] model of the 8-GeV spectrometer (see Table XXII of Appendix A) incorporating measured excitation constants for the magnets. The transformation of charged-particle coordinates from the target to the spectrometer focal planes is described by a matrix of first and second-order coefficients in a Taylor series expansion of the particle coordinates about the spectrometer central ray. Using the matrix coefficients as described in Appendix A, a Monte Carlo ray-tracing program was used to calculate the acceptance of the individual P-θ bins of the spectrometer focal planes. A P-θ bin is defined by the intersection of a P bin and a θ bin, so that ΔP and $\Delta\theta$ were already known from the measured P and θ dispersions. The azimuthal angular acceptance, $\Delta\phi$, for a particular P-θ bin averaged over the target length, was determined by lead apertures downstream of Q81 and B82 and ranged from ± 12 to ± 30 mrad. The total acceptance $\Delta\Omega\Delta P/P$ summed over the 20×54 such P-θ bins was 2.833 msr%; the θ hodoscope covered an angular range $\Delta\theta = \pm 7.95$ mrad, while the momentum hodoscope accepted $\Delta P/P = \pm 2.02\%$. In the off-line analysis of experiment B, all P-θ bins were used while in experiment A the hodoscope lead masks (see Fig. 7) partially shadowed the edge bins and events were accepted only if they fell within θ bins 2–53 and P bins 2–19. This restricted acceptance was 2.492 msr% with $\Delta\theta = \pm 7.65$ mrad and $\Delta P/P = \pm 1.82\%$. The absolute uncertainty in either acceptance was believed to be about ± 1.5%; an additional uncertainty of 1% due to a possible momentum dependence of the acceptance could not be

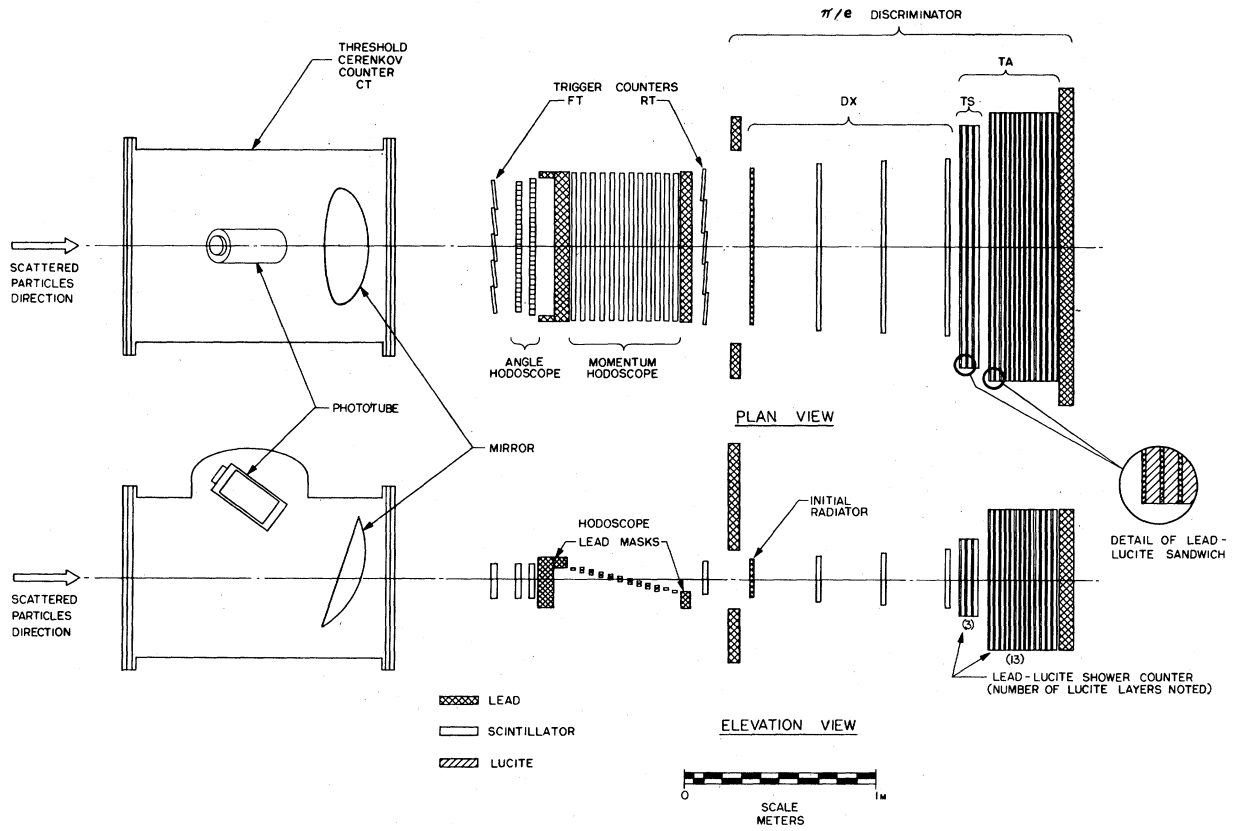

FIG. 7. Magnet-focal-plane detector arrays. Their positioning in the magnetic spectrometer is shown in Fig. 4.

ruled out. A list of the properties of the 8-GeV spectrometer is given in Table I along with estimates of the percentage uncertainties in these figures.

E. Particle detectors

1. Introduction

The particle-detection system provided event triggers for essentially all the electrons scattered into the spectrometer acceptance and discriminated electrons from a background consisting predominantly of pions. All of the particle detectors, shown in Fig. 7, were mounted on a steel boom tilted at 30 degrees to the horizontal. A concrete and lead cave shielded the detectors from backgrounds that would otherwise have swamped the true signals.

Scattered particles, after traversing the last quadrupole magnet, passed through a threshold Cherenkov (CT) counter filled with freon gas. They then traversed track-defining elements consisting of a front trigger (FT) counter followed by angle and momentum hodoscopes and a rear trigger

TABLE I. Properties of the 8-GeV spectrometer.

Property	Expt A	Expt B	% Error
Momentum resolution ($\delta P/P$)	±0.10%	±0.10%	1%
Momentum dispersion	2.91 cm/%	2.91 cm/%	1%
Momentum acceptance ($\Delta P/P$)	±1.82%	±2.02%	1%
θ resolution	±0.14 mrad	±0.14 mrad	1%
θ dispersion	4.58 cm/mrad	4.58 cm/mrad	1%
θ acceptance	±7.65 mrad	±7.95 mrad	1%
ϕ acceptance (max)	±29.6 mrad	±29.6 mrad	
Solid angle ($\Delta\theta\Delta\phi$)	0.685 msr	0.701 msr	1.8%
Acceptance ($\Delta\theta\Delta\phi\Delta P/P$)	2.494 msr%	2.833 msr%	1.5%

(RT) counter. Next, a 1-radiation-length lead slab serving as an initial radiator was followed by a group of three scintillation counters (DX), that measured specific ionization of the resultant particles. This slab was followed by 15 additional 1-radiation-length lead slabs interspersed with Lucite that together formed the total-absorption (TA) counter. The first three segments of the TA counter functioned as another detector, the truncated shower (TS) counter, sampling the early development of an electron shower.

All of the particle-identification techniques exploited the fact that background particles had much larger rest masses than electrons. The TA counter was used to define a good sample of electrons at all values of E', while the DX and TS counters gave additional pion rejection where needed. Particular emphasis in the following discussion is placed upon the functioning of each detector under conditions of high background rates, which were frequently encountered in the two experiments.

2. *The threshold Cherenkov counter*

The threshold Cherenkov counter, used to identify electrons, was 1.14 m long and was pressurized with gaseous freon-12 (CCl_2F_2). It identified electrons by detecting the Cherenkov light emitted in the particle passage. A four-segment mirror reflected the Cherenkov light to a Phillips 58UVP phototube which viewed the interior of the counter through a quartz window. During experiment A, the gas pressure was maintained at 589 mm Hg, corresponding to a threshold for pions at $E' = 3.5$ GeV. During experiment B the gas pressure was maintained at 246 mm Hg corresponding to a threshold for pions $E' = 5.5$ GeV. Pions could still produce light in the counter by the production of secondary electrons, and consequently the CT counter was placed forward of all other detectors to minimize the amount of material in the path of the particles. Events were accepted as electrons if sufficient Cherenkov light was produced in the counter. In experiment A we required that the anode signal from the phototube fire a discriminator circuit. In experiment B we required that the integrated charge from the anode pulse be above a minimum value.

Electrons fired the CT discriminator with an efficiency of 88.1–89.9% in experiment A with circuit dead-time corrections ranging from 0 to 2%. This low efficiency was the result of a poor quality phototube and a misaligned mirror segment and poor optical coupling to the quartz window. This also resulted in a geometrical variation in the efficiency. Replacement of the phototube and realignment of the mirror system raised the electron detection efficiency to 98.0% in experiment B. This efficiency is believed known to better than 0.4% in both experiments. The Cherenkov counter discriminated against pions for $E' \leq 3.5$ GeV in experiment A and for $E' \leq 3.5$ GeV in experiment A and for $E' \leq 5.5$ GeV in experiment B. For energies below pion threshold, 0.3% to 0.7% of the background pions could still masquerade as electrons through the production of knock-on electrons and through chance coincidence.

3. *Trigger counters and hodoscopes*

The trigger counters and hodoscopes were located inside a light-tight, magnetically shielded box. The trigger counters were arranged in two rows of five scintillation counters, one row positioned near the entrance and one near the exit windows of the box. A "fast-trigger" coincidence between any front trigger counter and any rear trigger counter was interpreted as the passage of a particle. Five counters were needed to cover the large horizontal acceptance and yet retain precise timing. In addition, the substantial reduction in front and rear trigger dead times from the use of five counters allowed operation at much higher trigger singles rates than would otherwise have been possible. The loss of events from trigger counter dead times was kept below 3%, and the trigger efficiency was essentially 100% in the limit of zero counting rate.

Each hodoscope consisted of two rows of scintillation counters with the back row offset by one-half a counter width. A typical electron fired a counter in the front row and one or both of the two counters in the back row of each hodoscope that overlapped the one in front. The patterns of fired counters in each hodoscope were decoded to yield horizontal and vertical position, and hence the angle and momentum of a scattered particle. Reference 40 gives a very detailed description of the hodoscope-decoding-system procedure developed for the 8-GeV spectrometer. The adaptation of this procedure to our experiments[20] is summarized in Sec. IV A.

A new momentum hodoscope with 21 counters in two horizontal rows had been fashioned[26] for these experiments. The 20 momentum bins thus defined by the overlaps provided an rms resolution $\delta P/P \simeq \pm 0.1\%$. The θ hodoscope was the same one used in all previous experiments[7,29] with the 8-GeV spectrometer. A total of 55 counters overlapped so as to define 54 θ bins with an rms angular resolution $\delta\theta = \pm 0.14$ mrad. The lead masks at the limits of both hodoscopes ensured that electrons

falling outside the hodoscopes' edges would not shower in the total absorption counter.

4. The π/e discriminator

The total absorption counter was composed of 16 Lucite slabs sandwiched between 1-radiation-length lead slabs as shown in Fig. 7. Each Lucite slab was viewed by four RCA 6342-A phototubes; the anode signals from the 64 phototubes were added and the total signal pulse-height analyzed. For a single event this TA signal was proportional to the shower multiplicity and, consequently, to the electron's energy. A typical spectrum had a pion peak in low channels and a roughly Gaussian electron peak whose position was proportional to E' and whose fractional full width at half-maximum (FWHM) varied roughly according to $(E')^{-1/2}$. A cut placed one FWHM below the peak center divided events into two classes. Electrons fell into the upper class with 99.1% frequency; the lower class was discarded as background. Systematic uncertainty in the total absorption counter efficiency was about ± 0.2%.

The pion peak had an exponential tail attributable mainly to pion-nucleus interactions in the TA counter. This tail typically extended to high channels, making difficult a clean separation of electrons from background. At high E', near pion-electroproduction threshold, where pion rates were low and the electron peak fell in very high channels, separation was straightforward. At lower E', large pion background began to obscure the electron peak and the CT counter had to be used in addition to the TA counter to provide the needed pion rejection. At the very lowest E' where electrons comprised less than 1% of all detected particles and the electron peak was in low channels good signatures in the DX or TS counter were also needed to discern an electron peak. For detection of positrons (i.e., for positive spectrometer polarity) the full array of counters was usually required to give adequate rejection of backgrounds.

The DX counters, individually pulse-height analyzed, were used to determine whether a shower had begun in the initial radiator. In general, a pion would traverse the initial radiator without interaction and would register in each counter as a single-ionizing particle, with a typical Landau distribution. With probability about 70%, an electron would produce fast secondary particles that enhanced the anode signals from each counter. The pulse-height spectrum of a single DX counter for an electron sample showed a Landau peak in low channels followed by a broad continuum corresponding to production of one or more fast particles. A cut placed in the valley between the Landau peak and this continuum, corresponding to a signal about 1.5 times that of a single minimum ionizing particle, ensured moderate insensitivity to gain shifts. The DX condition required an event to have signals above this cut in all three DX counters or it was considered background. The pion rejection of the threefold DX counter was about 97%, while the efficiency for single electrons[26] varied from 60.9% at $E' = 2$ GeV to 80.5% at 8 GeV. A second cut at 2.5 times minimum-ionizing pulse height gave better than 99% pion rejection, but the electron detection efficiency fell to 38.3% at 2 GeV and 65.0% at 8 GeV.

A correlation between the observed DX efficiency and the background singles rates was a potentially serious source of error, as these rates were different for deuterium and hydrogen targets. This correlation arose because chance coincidence with background particles enhanced the observed pulse height and correspondingly enhanced the apparent electron-detection efficiency of the DX system. This enhancement was typically 1–2% in kinetic regions were the DX counter was needed, but was as high as 5% in some very high-rate runs. A rough parametrization[26] of the enhancement was obtained using the fast trigger and DX singles rates. When the base DX efficiency was corrected using this function, the systematic uncertainty in the DX efficiency was less than 0.5%.

Another counter that sampled the early shower development was the truncated shower (TS) counter. Anode signals from the first three Lucite slabs were picked off and summed to produce the TS signal which was independently pulse-height analyzed. A typical TS spectrum for pions showed a peak in the lowest few channels with a greatly foreshortened exponential tail. Electrons registered as a Poisson-distributed peak centered about a pulse height that was roughly proportional to E'. In the analysis of experiment A, a variable cut placed in the valley between the electron and pion peaks ensured a 90.1% efficiency for detection of electrons. In the analysis of experiment B, two different fixed cuts were used in a manner similar to the treatment of the DX counter. Electrons produced a TS signal above the low cut with an efficiency that ranged from 90.1% at $E' = 3.0$ GeV to 97.8% at $E' = 8.0$ GeV. Similarly, the electron detection efficiency using the high cut ranged from 72.5% at $E' = 3$ GeV to 93.0% at $E' = 8$ GeV. Uncertainties in these efficiencies were less than ±0.3%.

The TS counter condition was always used before the DX counter when both were available

to reject backgrounds. The TS counter was much more effective in domains where the singles rates were high. As the counter elements were Lucite instead of scintillator, additional soft-background particles made little difference, and no rate dependence of the efficiency was observed. The TS counter also proved to be superior to the DX counter in general, as two simultaneous pions produced a signal that was usually below the cut in the TS spectrum. There were some runs in which extremely large backgrounds required the use of both the DX and TS counters. Because the two counters both sampled the early shower development, and the DX and TA signals were correlated for a given event, their electron-detection efficiencies were not independent. In those runs an electron-detection efficiency was used[26] for the TS counter that accounted for this correlation.

F. Data logging

Anode signals were routed from the detectors to the counting house and converted by fast logic into digital information. This trigger logic generated an interrupt to an SDS 9300 computer for every likely event and provided digital information about the response of the detectors. The event interrupt directed the computer to scan buffers for the information deposited there by the event logic; this information was written onto magnetic tape for later analysis.

The event interrupt to the computer was derived from the anode signals of the front and rear trigger trigger counters and the CT or TA counters. Signals from the ten trigger counters were independently discriminated and fed to two logical OR circuits as shown in Fig. 8. A coincidence between any front trigger and any rear trigger produced a fast trigger or $C1$. The fast trigger in time with a pulse from either the CT or TA discriminators formed two definitions ($C2$ and $C9$) of a likely electron event. The TA discriminator output signal by itself provided a backup definition of a likely electron event, independent of $C1$ circuit dead-time losses. Thus the event trigger circuit OR4 was virtually 100% efficient for electron events. The output of OR4 set a latch-type flip-flop circuit which was reset only by the accelerator pretrigger just prior to the next beam pulse. This flip-flop set transition in turn generated the hardware interrupt to the computer; only one such interrupt could be generated per beam pulse because the computer could not handle a faster event rate. The output of OR4 was redundantly scaled to allow accurate corrections for the "computer dead time." Event rates were kept below 0.5 events/pulse by adjusting the beam current; this corresponded to a maximum 25% loss of events. The threshold on the TA discriminator was set to minimize the number of pion triggers while ensuring 100% efficiency for electrons. Below $E' = 2$ GeV, however, between 1% and 10% of the electrons would fail to fire this circuit, and a high efficiency for triggering on electron events could be maintained only with the help of the $C2$ coincidence trigger. The chance coincidence contribution to the event triggers was monitored by false coincidence circuits $C2F$ and $C9F$, which were parallel to the trigger circuits $C9$ and $C2$.

Binary characteristics of each event were flagged by DCD (discriminator-coincidence-discriminator) circuits, which timed output signals from the various discriminators and coincidence circuits against gate pulses from the trigger logic. A successful coincidence set a flip-flop that was read by computer via multiplexer interface. The pattern of hodoscope counter events was recorded in much the same manner. An event pulse also triggered linear gate and stretcher circuits that processed the pulses from the TA, CT, DX, and TS counters prior to conversion by a bank of six analog-to-digital converters (ADC'S) whose digitized information was read by computer.

The SDS 9300 Computer,[41] with 32×10^3 24-bit words of core storage, logged the data onto magnetic tape for later analysis. Twelve words of information were written onto magnetic tape for each event. These data included 76 bits for the θ and P hodoscope counters, 32 bits for DCD flags, the outputs of the six ADC's, two target temperature readings, and the beam pulse charge.

In addition to logging events, the computer performed many tasks that were invaluable to the successful execution of the experiment. An on-line analysis of a sample of the events was carried out by the computer. It was extremely helpful in detecting and diagnosing equipment malfunction. Oscilloscope displays of pulse-height spectra and related histograms provided information about the performance of the apparatus, both in the end station and the counting house. Between runs, appropriate targets were positioned into the beam and magnet currents set to desired levels using feedback loops under computer control. Experimental runs were started and stopped with the aid of the computer, which logged scalers and charge monitors at the end of a run and cleared them at the beginning. During a run, when it was not logging events, the computer monitored magnet currents, target temperatures, and the voltages of all photomultipliers and electronics power supplies.

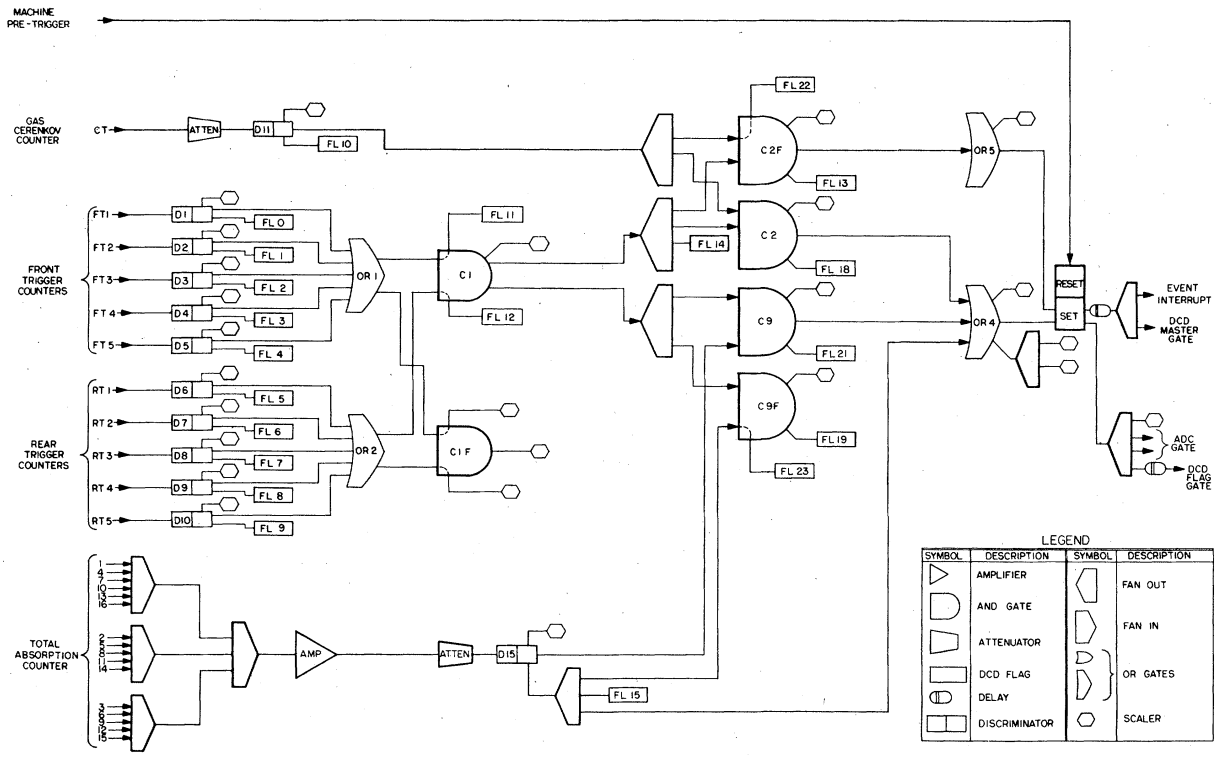

FIG. 8. The fast electronic logic. This array developed the main event interrupt to the computer and the master gate pulse to the discriminator-coincidence-discriminator (DCD) units associated with the hodoscope counters.

IV. DATA ANALYSIS

A. Introduction

After each experiment, the data from the magnetic tapes were reduced in three major steps to differential cross sections for inelastic e-p and e-d scattering. In the first step, or Pass I, electron events were separated from background events, and histograms of these events were compiled for each experimental run. Cross sections were calculated from the histogram data in Pass II, and empty-target π^0-decay, and pair-production contributions were subtracted to yield the raw e-p and e-d cross sections. Corrections for radiative effects were applied in the third step, yielding the final inelastic e-p and e-d cross sections. Event and run information were read from magnetic tape in Pass I, sorted, and stored in condensed form on magnetic disk storage. Subsequent data-analysis programs communicated only with this disk.

Much time and effort were devoted to finding and correcting systematic shifts in the data. As the statistical accuracy was frequently better than 2%, systematic errors were often the dominant uncertainty in the cross section. Of particular interest were systematic shifts between measurements at different scattering angles for the same (ν, Q^2), which could seriously affect the structure-function separations and the comparisons of the proton and deuteron measurements. All known effects of order $\pm 0.1\%$ were consequently included in the analysis.

B. Event analysis

In the Pass I analysis of both experiments, electron events were distinguished from background events and were sorted according to scattering angle and momentum by their signatures in the various detectors. The ideal electron event would show a coincidence between a front and a rear trigger counter, and have at least one counter firing in each row of counters in the two hodoscopes. It would produce a signal in the CT counter that either was above discriminator threshold (in experiment A) or above a cut applied to the CT pulse-height spectrum (in experiment B). The electron usually began to shower in the initial radiator, in which case the signal in each of the three DX counters would at least be above the lower cut on the DX pulse-height spectrum. The signals in the TS and TA counters were also above the electron cuts for those pulse-height spectra. Not all the above criteria were required of every

electron event used for cross section calculations. Only those criteria which were necessary to make a clean separation between electron events and background events were required in a given experimental run.

The angle and momentum of a scattered particle were determined from the signatures in the two hodoscopes. The minimum signature required was a single counter fired in each of the two hodoscopes. Events without at least one counter fired in each hodoscope were considered to have fallen outside the spectrometer acceptance and were rejected. For the remaining events, the pattern of counters fired in either hodoscope fell into one of three categories.[20,40] There were single-track and double-track events, corresponding to one or two clearly definable tracks in either hodoscope and ambiguous events, which had more than two tracks or an undecodable pattern of counters fired. Events were grouped into four classes[20] according to their signatures in the two hodoscopes: Class 1 had a single track in each hodoscope, class 2 had a single track in one hodoscope and a double track in the other, class 3 had a double track in both hodoscopes, and class 4 had an ambiguous pattern in either hodoscope. The angle and momentum of events in class 1 were unambiguously calculated from the horizontal and vertical position of the single track. In a typical experimental run, 95% of the events fell into class 1. Electron events in all four classes were accepted in the analysis, but only events from class 1 could be used to determine the distribution of events in angle and momentum for a given run. These two-dimensional distributions, which were 20×54 arrays called "P-θ planes," were frequently necessary in later analysis for those runs where the cross section varied sharply over the ranges of θ and E' covered by the spectrometer acceptance. For these runs, the events in classes 2–4 provided correction factors (see Sec. IV C) for the cross sections calculated from the events in class 1. The TA and DX spectra were also found to correlate with the event classes described above.

The event signatures in the remaining detectors provided the basis for discrimination of electron events from background[26]:

$C1$, the event had a front-rear trigger coincidence;

TA, the event had a signal above cut in the total absorption counter;

CT, the event had a signal above discriminator threshold (experiment A) or above cut (experiment B) in the gas Cherenkov counter;

TS, the event had a signal above (low) cut in the truncated shower counter;

DX, the event had a signal above (low) cut in all three DX counters.

Two additional event signatures, DXH and TSH, required signals above the high cut in all three DX counters or above the high cut (experiment B only) in the TS counter. Events lacking a few of these signatures (except $C1$ and TA) could still be classified as electron events, as described below.

Combinations of these event signatures formed the definitions of good electron events used in the analysis of the two experiments. All electron events were required to have a fast-trigger coincidence and a signal above cut in the TA counter. Good signatures in the CT, TS, DX counters were required as necessary to reject pion backgrounds. The ten such definitions, or "tribes," used in the analyses of both experiments are given in Table II. The tribes are listed roughly in order of increasing efficiency for the rejection of pion backgrounds. The electron-detection efficiency corresponding to each tribe is estimated for $E' = 2$ GeV to $E' = 8$ GeV in both experiments. Dead-time losses are included in these estimates. Two additional tribes, which required a TSH signature instead of a TS in tribes 4 and 7, were used in the analysis of

TABLE II. Event tribes.

Tribe No.	Tribe signature	Efficiency A (%)	Efficiency B (%)
1	$C1$-TA	96–99	96–99
2	$C1$-TA-CT	83–88	94–97
3	$C1$-TA-DX	58–80	58–80
4	$C1$-TA-TS	86–89	86–97
5	$C1$-TA-DXH	37–64	37–64
6	$C1$-TA-CT-DX	51–71	57–78
7	$C1$-TA-CT-TS	75–79	85–95
8	$C1$-TA-CT-DXH	32–57	36–63
9	$C1$-TA-CT-TS-DX	48–67	54–77
10	$C1$-TA-CT-TS-DXH	31–55	36–62

experiment B, but not experiment A. For each experimental run, the number of events in each tribe was stored on disk along with TA pulse-height spectra and P-θ planes corresponding to each tribe. Pion contamination of the electron sample from each tribe could be estimated and subtracted by examining visually the appropriate TA spectrum. For the calculation of the cross section in a given run, we used the events in that tribe which had the highest electron-detection efficiency, yet provided a clean separation of the electron and pion peaks in the TA spectrum. Pion contamination of the selected tribe was never more than 1.5% of the total yield of electrons, and the error from the pion subtractions was never more than 0.5% of the cross section. Other pertinent information, such as scaler, charge-monitor, and target-density data, were stored on disk in Pass I.

C. Run combination

Differential cross sections were calculated (in units of cm^2/s GeV) for each full-target run according to the formula

$$\frac{d^2\sigma}{d\Omega\, dE'} = \frac{N_{\rm tr}}{N_{\rm in}(\Delta\Omega\Delta P) l_t \rho_t} C_A\left(\prod_i C_i\right) , \qquad (4.1)$$

where $N_{\rm in}$ is the number of electrons incident during the run and $N_{\rm tr}$ is the electron yield in any of the tribes described in the previous section. The appropriate spectrometer acceptance $\Delta\Omega\Delta P$ (in sr GeV) was used (see below), while l_t and ρ_t are the target length (in cm) and density (in nuclei/cm^3) at 21.0°K. The averaging correction factor C_A took into account the kinematic variation of the cross section across the spectrometer acceptance and adjusted the cross section to its appropriate value at the quoted central values of E' and θ. The factors C_i correct for electrons lost in measurement or excluded in the analysis. Empty-target and positron cross sections were calculated in a similar manner and subtracted in Pass II to yield the raw cross sections for inelastic e-p and e-d scattering.

Three definitions of the acceptance were used in the calculation of cross sections. For a fraction of runs in both experiments, the cross sections were calculated using the total electron yields and the full spectrometer acceptance. In this case the deviation from unity of the averaging correction factor C_A, calculated from the P-θ planes of single track events in the selected tribe, ranged from 1% to 10%.

Another definition was employed for some runs in experiment B with sufficiently large numbers of events. Here the full acceptance was divided into four segments in E' in order to provide additional information about the E' dependence of the cross section. The cross section was calculated for each segment using the separate electron yields and the acceptance $\Delta\Omega\Delta P$ of each segment. The averaging correction factor here corrected mainly for the finite angular acceptance of each segment and its deviation from unity was generally less than 3%.

The third definition was used in a subset of runs that overlapped in E' and provided continuous spectra of hydrogen, deuterium, and empty target data for $W \leq 2$ GeV. These were at low E in the 18° measurements of experiment A and at all values of E in the 15°, 19°, and 26° measurements of experiment B. For these runs, events with single tracks in both hodoscopes were binned according to their missing energy $E/\eta - E'$, where

$$\eta = 1 + (2E/M)\sin^2(\tfrac{1}{2}\theta) .$$

Fine-mesh cross sections were calculated for each missing-energy bin, typically 8–10 MeV wide, using the yields in the 20× 54 bins of the P-θ plane stored on disk for the selected tribe and the acceptances $\Delta\Omega\Delta P$ of the individual P-θ bins. Here the deviation from unity of the averaging correction factor was also less than 3%. In all three methods of cross-section calculation, the experimentally measured variation of the cross section, as determined from the P-θ plane of the slected tribe, was always used in the calculation of the averaging correction factor C_A. Systematic uncertainty in C_A was never more than 1% and usually much less.

In Table III are listed the other correction factors that were applied to the measured yields, along with typical values and systematic uncertainties. The correction factors fell into three categories: those that were (a) independent of, (b) related to, the individual tribe definitions, or (c) applied only when a subset of the full spectrometer acceptance was used to calculate a cross section.

Correction factors a.1–a.6 were always applied to the measured yields when calculating a cross section. Correction factors b.1 to b.5 were applied only when the selected tribe required a good signature in the corresponding counter. Embedded in these correction factors are corrections for the singles-rate dependence of the counter efficiencies mentioned in Sec. III. Correction factors c.1–c.3 were applied only when a limited segment of the P-θ plane was used to calculate a cross section. The factors c.2 and c.3 corrected for an observed variation of the CT and DX counter efficiencies with position in the P-θ plane. More detail about

TABLE III. Correction factors.

Factor	Corrects for	Typical value	Uncertainty (%)
a. 1	Computer dead time	1.00–1.40	0.0
a. 2	Trigger dead time	1.00–1.01	0.0
a. 3	Trigger inefficiency[a]	1.00–1.05	0.0–0.5
a. 4	C1 dead time	1.00–1.03	0.0–0.1
a. 5	TA inefficiency	1.01	0.2
a. 6	Target-density fluctuation		
	(a) fan on	0.99–1.00	0.3
	(b) fan off[a]	1.01–1.30[a]	0.4–0.6[a]
b. 1	CT inefficiency	1.12–1.15[a]	0.4
b. 2	DX inefficiency	1.24–1.64	0.3–0.5
b. 3	DXH inefficiency	1.54–2.61	0.3–0.5
b. 4	TS inefficiency	1.11[a]	0.2–0.3
b. 5	TSH inefficiency[b]	1.08–1.38[b]	0.3[b]
b. 6	Residual pion background	0.98–1.00	0.0–0.5
c. 1	Non-single-track events	1.00–1.15	0.2
c. 2	CT inhomogeneity	0.95–1.20[a]	0.5
c. 3	DX inhomogeneity	0.95–1.05[a]	0.5

[a] Experiment A only.

[b] Experiment B only.

these correction factors may be found in the references.[20, 26]

Contributions to the full-target cross sections from electron scattering in the target cell walls were estimated from the electron yields in experimental runs with the "thick" empty replica target in the beam line. Empty-target cross sections were calculated from Eq. (4.1) using the measured yields and the appropriate full-target densities. After suitable normalization for the ratios of cell wall thicknesses, these empty-target cross sections were subtracted from the full-target cross sections. In those kinematic regions where continuous spectra had been measured, the empty-target cross sections were first fit by a polynomial. Empty-target cross sections were then computed from this fit for each missing-energy bin, and subtracted from the full-target cross section for that bin. In experiment A, the empty-target cross sections were typically 6–8% of the hydrogen and 4–5% of the deuterium full-target cross sections. In experiment B, they were, respectively, 4–5% and 3–4% of the hydrogen and deuterium full-target cross sections.

Electron backgrounds from pair production processes, primarily Dalitz decays of neutral π mesons photoproduced or electroproduced in the target, were determined by reversing the spectrometer polarity and measuring the yield of positrons for the same E' and θ. Positron cross sections were calculated from Eq. (4.1) using these measured positron yields and subtracting the cell-wall contributions in the manner described above. These positron cross sections were also subtracted from the full-target cross sections to yield the raw cross sections for inelastic e-p and e-d scattering. In practice, these positron cross sections had to be measured only at low E', where the pair production processes contributed ~ 1% or more to the full-target cross section. At the very lowest E' surveyed, particularly below $E' = 2$ GeV in experiment A, the pair production contribution was as high as 30% of the full-target cross section.

The random errors in the correction factors, which were normally a few tenths of one percent, were added in quadrature with the errors from counting statistics to give the random error in the cross section measured in each run. The random errors in the full-target, empty-target, and positron cross sections were then combined in quadrature to yield the random errors in the raw e-p and e-d cross sections.

D. Radiative corrections

1. Introduction

Corrections were applied to the raw e-p and e-d scattering cross sections to account for the effects of radiation by the electrons. This radiation could occur while the electrons were straggling in the material before or after the scattering, or as internal bremsstrahlung during the scattering process itself.[42, 43] The entire radiative correction procedure for inelastic scattering can be summarized by the equation

$$\frac{d^2\sigma}{d\Omega dE'}(E,E',\theta) = C\left[\frac{d^2\sigma}{d\Omega dE'}(E,E',\theta)_R - I_1 - I_2\right], \tag{4.2}$$

where $(d^2\sigma/d\Omega dE')(E,E',\theta)_R$ is the measured raw cross section and $(d^2\sigma/d\Omega dE')(E,E',\theta)$ is the corrected cross section which can then be related to the structure functions according to Eq. (1.2). For e-p scattering, I_1 is the contribution to the raw cross section from the radiative tail of elastic e-p scattering, and is calculated directly[44] from the well-known proton form factors.[29] For e-d scattering, I_1 is the contribution to the raw cross section from radiative tails of elastic and quasielastic e-d scattering. For both e-p and e-d scattering, the quantity I_2 is the contribution to the raw cross section from radiative tails of inelastic scattering processes. A direct calculation of I_2 would presume a knowledge of the structure functions of the proton and deuteron over large kinematic ranges. As these structure functions had not yet been measured and were assumed to be unknown *a priori* a model-independent unfolding procedure[43,45,46] involving all the measured cross sections at the same angle was used to calculate I_2. The factor C corrects for radiative processes that cause electrons scattered at (E,E',θ) to fall outside the spectrometer momentum acceptance, reducing the measured electron yield. The calculation of I_1, I_2, and C is discussed in the following sections. Exact expressions used in these calculations are given in Appendix B.

2. Radiation lengths

The quantities I_1, I_2, and C are functions of the amount of material, expressed in radiation lengths, in the path of the incident and scattered electrons. The material before scattering included a thin vacuum-separation window, the target cell wall, and, on the average, one-half the target liquid. The material after scattering and before the spectrometer vacuum included the remaining target liquid, the target cell wall, the aluminum scattering-chamber window, a few Mylar windows, and about 54 inches of helium gas at 1 atm. There was a slight angle dependence of the thickness in radiation lengths of target material traversed by the scattered electron. The average thickness in radiation lengths[47] of material before scattering, t_B, and of material after scattering, t_A, used in the radiative corrections of the two experiments are given in Table IV.

3. Elastic e-p radiative tails

Radiative tails I_{1p} from elastic e-p scattering were calculated according to Eq. (B.1) of Appendix B. This expression uses the exact calculation by Tsai[44] of single-photon internal bremsstrahlung. Effects of multiple-photon radiation by the recoiling proton were included in an approximate manner. The proton form factors $G_{Ep}(Q^2)$ and $G_{Mp}(Q^2)$ used in these calculations assumed the dipole form factor modified by a factor due to Miller[41] that is given in Eq. (B.2). The elastic e-p radiative tails ranged from a minimum of 0.2% of the raw cross section near $W = 2.0$ GeV to 33% at the lowest E' measured at 18°.

4. Elastic and quasielastic e-d radiative tails

For the case of inelastic e-d scattering, the quantity I_1 contains contributions from the radiative tails from elastic and quasielastic e-d scattering. The elastic e-d radiative tail was calculated in a manner identical to the elastic e-p radiative tail using deuteron form factors calculated from the Hamada-Johnston wave function.[48,49] In general, the elastic e-d radiative tail was a negligible contribution to the raw e-d cross section.

The quasielastic e-d radiative tail was calculated in a method that utilized the close connection between quasielastic e-d scattering and the sum of elastic e-p and e-n scattering. Because of diffi-

TABLE IV. Radiation lengths used in radiative corrections (uses radiation lengths for the various materials as given in Ref. 47).

Expt.	θ (deg)	t_B^p (10^{-2} r.l.)	t_A^p (10^{-2} r.l.)	t_B^d (10^{-2} r.l.)	t_A^d (10^{-2} r.l.)
A	18	0.4974	0.9842	0.5875	1.1174
A	26	0.4974	0.9795	0.5875	1.1137
A	34	0.4974	0.9733	0.5875	1.1094
B	15	0.9590	1.3937	1.1223	1.5584
B	19	0.9590	1.3886	1.1223	1.5522
B	26	0.9590	1.3757	1.1223	1.5370
B	34	0.9590	1.3551	1.1223	1.5131

culties in the calculation of radiation by bound-target nucleons, an exact calculation of single-photon internal bremsstrahlung was not attempted. Rather, an initial approximation of the quasielastic tail, I_{1d}^{ER}, was obtained using an equivalent-radiator technique[50] to estimate the contribution from internal bremsstrahlung. This technique is a good approximation in the soft-photon limit near the quasielastic peak, but it is known[43] to be inaccurate at low E', where hard-photon radiation dominates. Consequently, the radiative tail calculated in the equivalent radiator method was modified according to

$$I_{1d} = \frac{I_{1d}^{ER}}{I_{1p}^{ER} + I_{1n}^{ER}} (I_{1p} + I_{1n}) . \tag{4.3}$$

The elastic e-p and e-n radiative tails I_{1p} and I_{1n} were calculated from Eq. (B1) which uses the exact formula for single-photon emission[44] with the assumption of form-factor scaling ($G_{Ep}^2 = G_{Mp}^2/\mu_p^2 = G_{Mn}^2/\mu_n^2$; $G_{En} = 0$) and includes modifications for the effects of multiple soft-photon emission from the electrons. Radiation from the hadrons is small and was ignored. The quasielastic tail I_{1d}^{ER} and the elastic e-p and e-n tails I_{1p}^{ER} and I_{1n}^{ER} were calculated in the equivalent-radiator method as given by Eq. (B3) of Appendix B and also include the effects of multiple soft-photon emission. Differential cross sections for elastic e-p and e-n scattering used in these calculations were derived from the Rosenbluth equation[51] under the above assumption of form-factor scaling. Differential cross sections for quasielastic e-d scattering were calculated from the method of Durand[52] using s- and d-state Hamada-Johnston wave functions.[48] The quasielastic e-d radiative tails, as calculated from Eq. (4.3), ranged from 0.2% of the raw cross section near $W = 2.0$ GeV to 25% at low E'. They were roughly the same percentage of the raw cross section as the elastic e-p radiative tails,[20] except at low E'. Uncertainties in the neutron form factor G_{Mn}, which has been measured[53] only up to a Q^2 of 5 GeV^2, had little effect upon the calculation of the quasielastic tail. The neutron contribution to this tail was generally less than 3% of the raw cross section, and most of this contribution arose from low-Q^2 e-n scattering, for which the form factors are fairly well known.

5. *Inelastic radiative corrections*

The cross sections $(d^2\sigma/d\Omega dE')(E, E', \theta)$ remaining after subtraction of the elastic and quasielastic radiative tails were subsequently corrected for radiative processes linked to inelastic scattering. The inelastic radiative tails, which were calculated in the same manner for e-p and e-d scattering, may be expressed in the general form,

$$I_2(E, E', \theta, t) = \int_0^t \frac{dt'}{t} \int_{E_{min}}^{E} dE_1 \int_{E'}^{E'_{max}} dE_2 S(E, E_1, t') \frac{d^2\sigma}{d\Omega dE'}(E_1, E_2, \theta) S(E_2, E', t - t') \tag{4.4}$$

where $S(E_1, E_2, \tau)$ is an appropriate straggling function representing the probability that an electron degrades in energy from E_1 to E_2 in τ radiation lengths, including the effects of internal bremsstrahlung. The cross section $(d^2\sigma/d\Omega dE')(E_1, E_2, \theta)$ is the corrected inelastic cross section, whose measurement was the purpose of these experiments. The calculation of $I_2(E, E', \theta, t)$ consequently presumes a knowledge of the corrected inelastic cross sections throughout the kinematic region $E_{min} \leq E_1 \leq E$ and $E'_{max} \geq E_2 \geq E'$. The roughly triangular regions of E-E' space surveyed in the two experiments (see Figs. 2 and 3) permitted us to calculate this integral, using interpolations and an unfolding technique described below.

In the peaking approximation,[42,43] the two-dimensional integral in Eq. (4.4) reduced to two one-dimensional integrals.

$$I_2(E, E', \theta, t) = I_2^B(E, E', \theta, t_B) + I_2^A(E, E', \theta, t_A). \tag{4.5}$$

The terms I_2^B and I_2^A correspond to radiation before and after scattering and are given explicitly by Eqs. (B5) and (B6) of Appendix B. The contribution to I_2 from radiation both before *and* after scattering is small but not negligible; it was included in these one-dimensional integrals in an approximate manner. Contributions from internal bremsstrahlung were approximated by introducing an equivalent radiator

$$f(k) \frac{\alpha}{\pi} \left(\ln \frac{Q^2}{m_e^2} - 1 \right) .$$

The function $f(k)$ is a spectral function in the energy k of the emitted photon; the particular form used, $f(k) = 1 - (k/E) + 0.5(k/E)^2$ is due to Allton[54] and Bjorken.[55] For the case of single-photon emission, agreement of the Allton-Bjorken approach with the exact calculations of Tsai[44] was usually better than 1%, and never worse than 5%, of the inelastic radiative tail.[56] Multiple-photon emission was treated in an approximate manner, while the effects of radiation by the hadrons were

ignored.

At each scattering angle θ, the integrals I_2^B and I_2^A were first computed on a rectangular mesh of points (E_i, E_j') chosen to reflect the distribution of measured data. The mesh spacings ΔE and $\Delta E'$ ranged from a minimum of 10 MeV in the resonance region to a maximum of 100 MeV in the deep-inelastic region. The inelastic radiative corrections were independent of the mesh spacings used.[26] Uncorrected cross sections were calculated at each mesh point by an interpolation scheme[46] applied to the triangles of uncorrected cross sections $(d^2\sigma/d\Omega dE)(E, E', \theta)_M$. The six or more spectra measured at each angle in experiment A were sufficient to ensure the desired accuracy in the interpolations. Some trouble was encountered in extrapolating to $E < 4$ GeV in experiment A (see Fig. 2) and to $E < 10.0$ GeV at 15° and $E < 12.5$ GeV at 19° in experiment B (see Fig. 3). This difficulty increased the error in the radiative corrections only at the very lowest E' in these triangles. At 26° and 34° in experiment B, additional spectra measured earlier in experiment A were used to obviate this difficulty.

The integral equation that derives from Eqs. (4.2) and (4.5)

$$\frac{d^2\sigma}{d\Omega dE'}(E, E', \theta) = C\left[\frac{d^2\sigma}{d\Omega dE'}(E, E', \theta)_M - I_2^B - I_2^A\right] \tag{4.6}$$

was solved by an unfolding technique[43,46] applied to the mesh of uncorrected interpolations $(d^2\sigma/d\Omega dE')(E_i, E_j', \theta)_M$ at each angle. The corrected cross section was calculated at each mesh point (E_i, E_j') starting at pion electroproduction threshold and proceeding to higher invariant mass W. At threshold the inelastic radiative tail was zero, and the only correction was the factor C [see Eq. (B4)] needed to account for electrons lost from the yield. These corrected cross sections were then used to compute the inelastic radiative tail contributions to the adjacent higher W points according to Eqs. (B5) and (B6); these were subtracted and the correction factor C applied. This differential unfolding procedure continued until the cross section had been corrected at each mesh point at that angle; these points did not generally correspond to the exact kinematic points at which the measurements were made. The mesh of corrected cross sections $(d^2\sigma/d\Omega dE')(E_i, E_j', \theta)$ was then used to correct each uncorrected cross section $(d^2\sigma/d\Omega dE')(E, E', \theta)_M$ measured at that angle. The inelastic radiative correction was applied in the manner of Eq. (4.6). In experiment A, the total correction factor ranged from 1.18–1.78 at electroproduction threshold to 0.60–0.96 at the very lowest E' quoted. In experiment B, it ranged from 1.16–1.83 at threshold to 0.90–1.08 at the lowest E' surveyed. It was generally the same for proton and deuteron data.

6. *Treatment of errors*

Errors in the elastic and quasielastic radiative tails were deemed systematic and were thought not to contribute to the random error in the inelastic e-p and e-d cross sections. Sources of uncertainty in the elastic e-p radiative tails were uncertainties in the proton form factors and approximations in the treatment of multiple-photon radiation. The quasielastic e-d radiative tails had additional uncertainties arising from uncertainties in the neutron form factors and in the modified equivalent radiator technique, and from the theoretical approximation to the quasielastic e-d cross section. Altogether, the uncertainty in the elastic radiative tails was estimated to be 5% of the tail, while the quasielastic radiative tails had an estimated 6% uncertainty. Because of the sharp variation with E' of these tails, the resultant systematic uncertainty in the inelastic cross sections ranges from 0 to 4%. For E' greater than about 2.5 GeV, however, this uncertainty is never greater than 1% of the cross section. Most of this uncertainty is not present in the ratio of deuteron to proton cross sections.

Random errors were propagated through the inelastic radiative-correction procedure. Because of the interpolations needed to compute the inelastic tails, there was some correlation between the error in the inelastic radiative tail $I_2(E, E', \theta)$ and the error in the cross section $(d^2\sigma/d\Omega dE')(E, E', \theta)_M$. In the calculation of the random error in the inelastic cross sections, we accounted for this correlation in an approximate manner.

Systematic uncertainties in the inelastic radiative corrections are believed to arise mainly from the equivalent-radiator approximation and from the treatment of multiple-photon processes; they are similar for e-p and e-d scattering. A second pass of the radiative corrections was made using another spectral function $f(k)$ at each scattering angle that best approximated the exact tails[44] from single-photon radiation[56]; the corrected cross sections from this approach were compared with the nominal cross sections which had been calculated using the Allton-Bjorken method. Where the two methods disagreed by more than one half the random error (which only occurred at the $E' < 2$ GeV), no cross sections are quoted nor were they used in subsequent analyses. The systematic uncertainty in the inelastic radiative tail is believed to vary from 3% near threshold to 10% at low E'.

This amounts to at most 5% of the inelastic e-p and e-d cross sections, and that only at $E' < 2$ GeV.

Hadronic radiation was neglected in this formalism. As is known from work comparing elastic e^+p and e^-p scattering,[57] the presence of hadron as well as electron radiation makes the radiative corrections for the two processes slightly different, so that, in the absence of two-photon exchange processes the difference between e^+p and e^-p cross sections puts an upper limit on the size of this contribution.

Recently measurements of deep-inelastic e^+p and e^-p scattering have been performed.[58] With the above interpretation we can use their results to put an upper limit on two-photon exchange processes plus effects of hadron radiation. Their measurements of the (e^+p)-(e^-p) ratio are consistent with unity within their errors. Assuming no kinematic dependence we can combine their data to yield an overall ratio of $e^+p/e^-p = 1.001 \pm 0.008$. Therefore, we have assigned a fractional systematic error of ± 0.008 to cover these unknown processes.

An estimate of the systematic uncertainty in the entire radiative-correction procedure was obtained from a comparison of the procedure described here and a procedure[7,41] developed by SLAC group A. Both procedures had been applied to the cross sections measured at 6° and 10° in experiment C.[8,27] A comparison[27] of the two methods indicated that the cross sections obtained from the SLAC method were typically 3% larger than those obtained from our method. For a few data points at very low E' and low x the discrepancy was as large as 6%. From these comparisons with the SLAC approach we estimate the total systematic uncertainty in the cross section arising from the radiative corrections to vary as

$$\left(\frac{\Delta\sigma}{\sigma}\right)_R = 0.03 + 0.015\left(\frac{E'_{\text{elast}}(E,\theta)}{E'}\right). \qquad (4.7)$$

Here $E'_{\text{elast}}(E,\theta)$ is the scattered electron energy corresponding to elastic e-p scattering, and $(\Delta\sigma/\sigma)_R$ is the fractional systematic uncertainty in the corrected cross section.

V. CROSS SECTIONS

A. Proton and deuteron cross sections

In the approximation of single-photon exchange, the radiatively corrected cross sections are linear in the two structure functions W_1 and W_2, according to Eq. (1.1). We exploit this fact in presenting the e-p and e-d cross-section data graphically. The data for νW_2^p and νW_2^d are plotted versus W in Figs. 9–16. They were extracted from the measured cross sections assuming $R_p = R_d = 0.18$ in Eq. (1.5). The solid lines represent global fits to νW_2^p and νW_2^d that will be discussed in Sec. V C. As is evident from Figs. 9–16, most of the data of experiment B and some of the 18° data of experiment A exist as "fine-mesh" cross sections computed, as discussed earlier, using the angle and momentum information from the two hodoscopes. This fine resolution was indispensable in the resonance region and also at small $\omega \lesssim 2$ where the magnitude of the deuteron binding correction varies sharply over the spectrometer acceptance. These fine-mesh data were accordingly used in the study of the resonances and in the extraction of the neutron cross sections, as described in Sec. V D. On the other hand, studies of the structure functions and R in the deep-inelastic region did not require such fine resolution. For these studies, the fine-mesh data for $W \geq 1.8$ GeV were combined into statistically more precise cross sections by averaging several neighboring fine-mesh cross sections, as explained in Sec. V E. Treatment of the random and systematic errors is described in the following section.

The two experiments, A and B, were normalized to each other (see Sec. V F, following). In Table V we present the combined cross sections σ_p, σ_d, and σ_n as merged from experiments A and B. The cross sections from experiment B, where they existed for $\omega \lesssim 2$ at 26° and 34°, were used in lieu of those from experiment A. The errors given in Table V are 1-standard-deviation random errors.

The statistical precision of our data in the resonance region is not as good as that of previous low-Q^2 resonance cross-section measurements[27,28,46,59] at 4°, 6°, and 10° using the SLAC 20-GeV spectrometer. However, as these are the only high-Q^2 resonance data currently available, we present some of them in Figs. 17 through 20, which show the structure functions νW_2^p and νW_2^d again extracted from the cross sections assuming $R_p = R_d = 0.18$. Apparently, the cross section for resonance excitation is still relatively significant at the value of Q^2 measured here. The resonances in the vicinity of the $N^*(1520)$ and the $N^*(1688)$ resonances have excitation cross sections that appear to be the same fraction of the total cross section as at lower Q^2. On the other hand, the cross section for the excitation of the $\Delta(1236)$ is dropping more rapidly with Q^2 than the nonresonant background cross section underneath it. The peak in the vicinity of the $N^*(1688)$ resonance appears to shift to higher W with increasing Q^2, indicating that several partial-wave amplitudes are probably contributing to this peak. As is the case

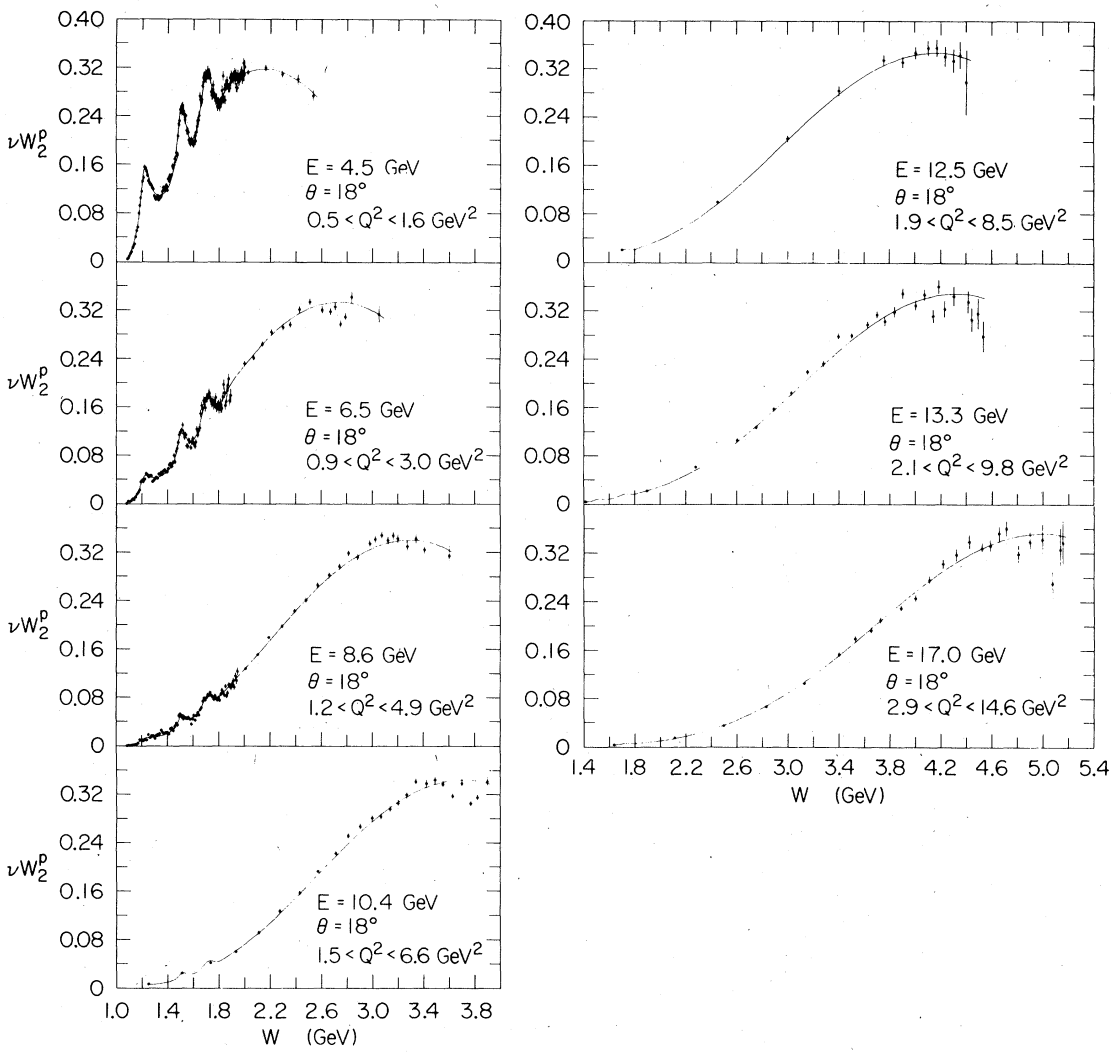

FIG. 9. The quantity νW_2^p extracted from inelastic e-p cross sections measured at 18° in experiment A assuming $R_p = 0.18$.

at low Q^2, no prominent excitation of the $\Delta(1920)$ is seen in these spectra.

B. Error summary

The random errors quoted in Table V arise from counting statistics and the possible random fluctuations in the properties of the beam, target apparatus, spectrometer, and the various monitors. These contributions are summarized in Table VI; percentage errors in the final cross sections arising from these sources are given.

The random error arising from counting statistics normally dominates the error from random fluctuations, which is typically 1% when all the contributions B.a–B.g are added in quadrature. These fluctuation errors were not reduced in the process of combining several experimental runs if the measurements were made over a time span which was short in comparison to the time scale of the fluctuations. Nor were these errors reduced when data from different missing-energy bins of the same run were combined into a single cross section for inclusion in Table V. Only the errors arising from counting statistics were reduced in combining the fine-mesh cross sections (see Sec. V E). As the measurements with hydrogen and deuterium targets had been interleaved in time, only errors from counting statistics and target-density fluctuations were included when calculating the random errors in the ratio σ_d/σ_p.

Systematic uncertainties in the e-p and e-d cross sections also fall into two categories: Those that affect only the overall normalization of either experiment, or those which could also have a kinematic variation. These are listed in Table VII

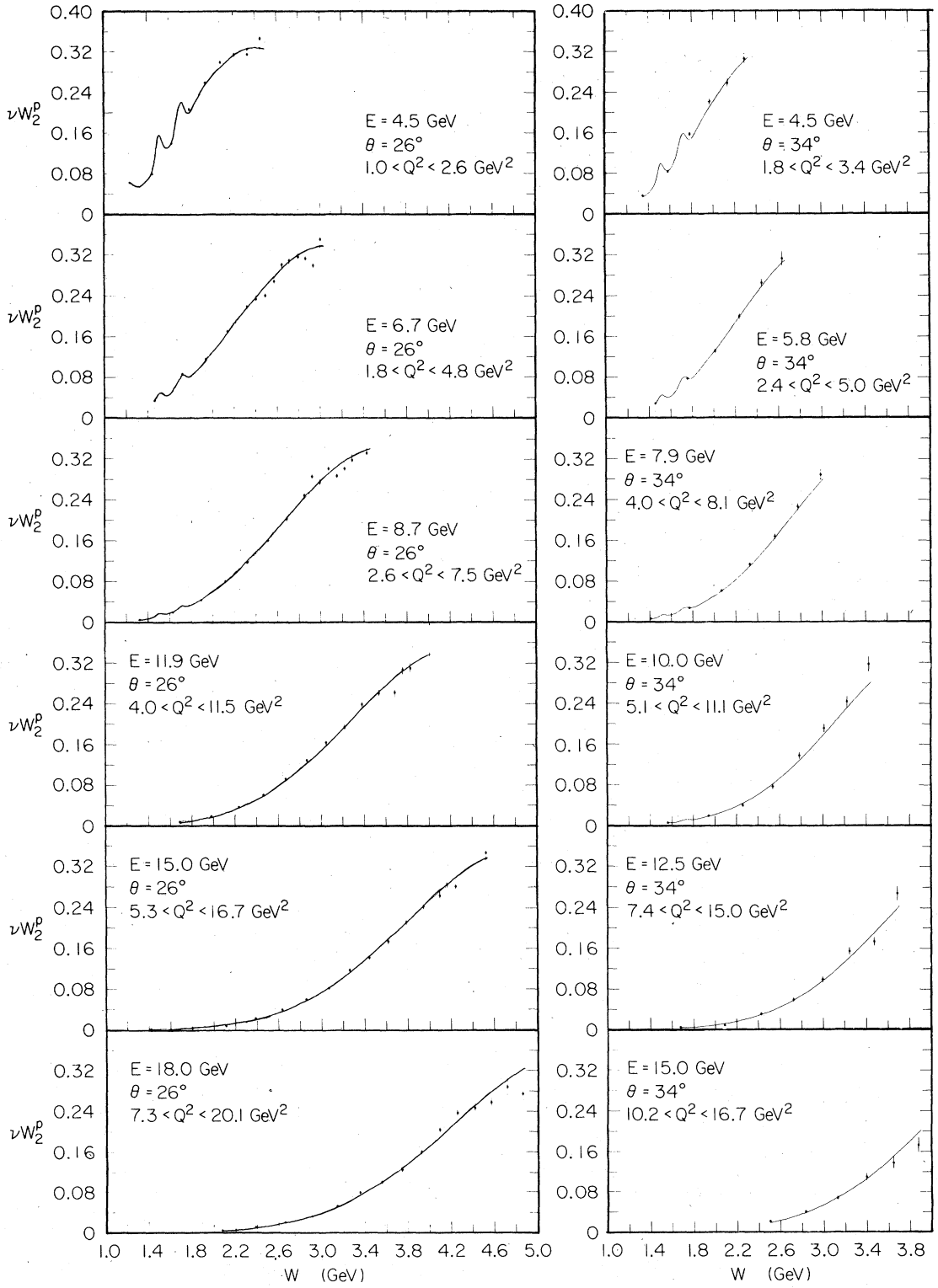

FIG. 10. The quantity νW_2^p extracted from inelastic e-p cross sections measured at 26° and 34° in experiment A assuming $R_p = 0.18$.

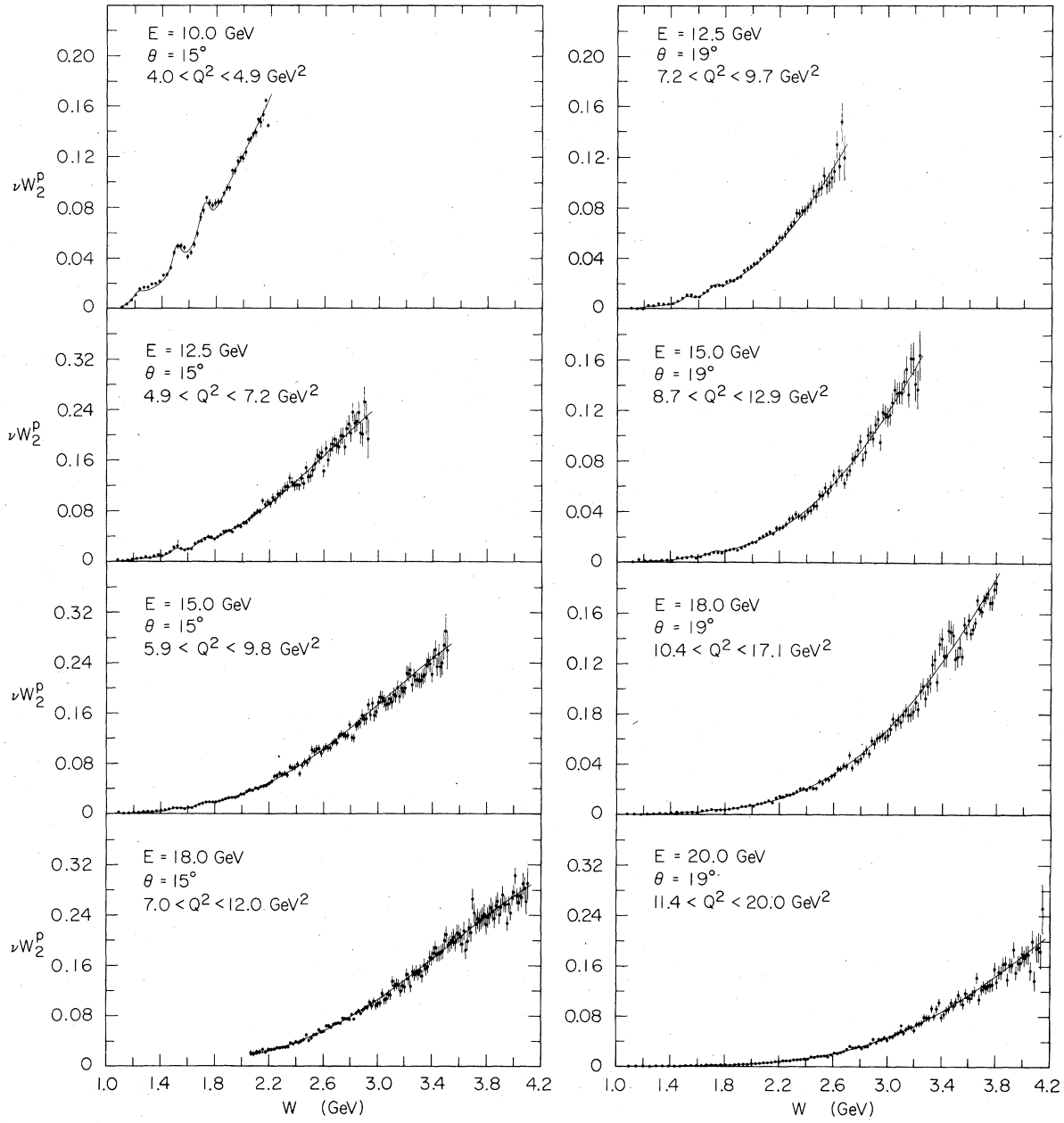

FIG. 11. The quantity νW_2^p extracted from inelastic e-p cross sections measured at 15° and 19° in experiment B assuming $R_p = 0.18$.

with typical estimates of each uncertainty.

Added in quadrature, the above systematic uncertainties yield an overall normalization uncertainty of 3.4–3.6% in the proton and deuteron cross sections. In addition, there is a point-to-point relative uncertainty of not more than 5.5% in these cross sections. When data from experiments A and B were merged for presentation in Table V and then used in conjunction with the 6° and 10° data[27,28] of experiment C to extract R, the cross sections were modified by normalization factors (see Sec. V F) that attempted to account for normalization differences among the three experiments arising from sources A.a–A.f in Table VII. Therefore, the systematic uncertainty in R must arise from the uncertainties in these normalization factors and from the sources B.a–B.f in Table VII. Most of the systematic uncertainties,

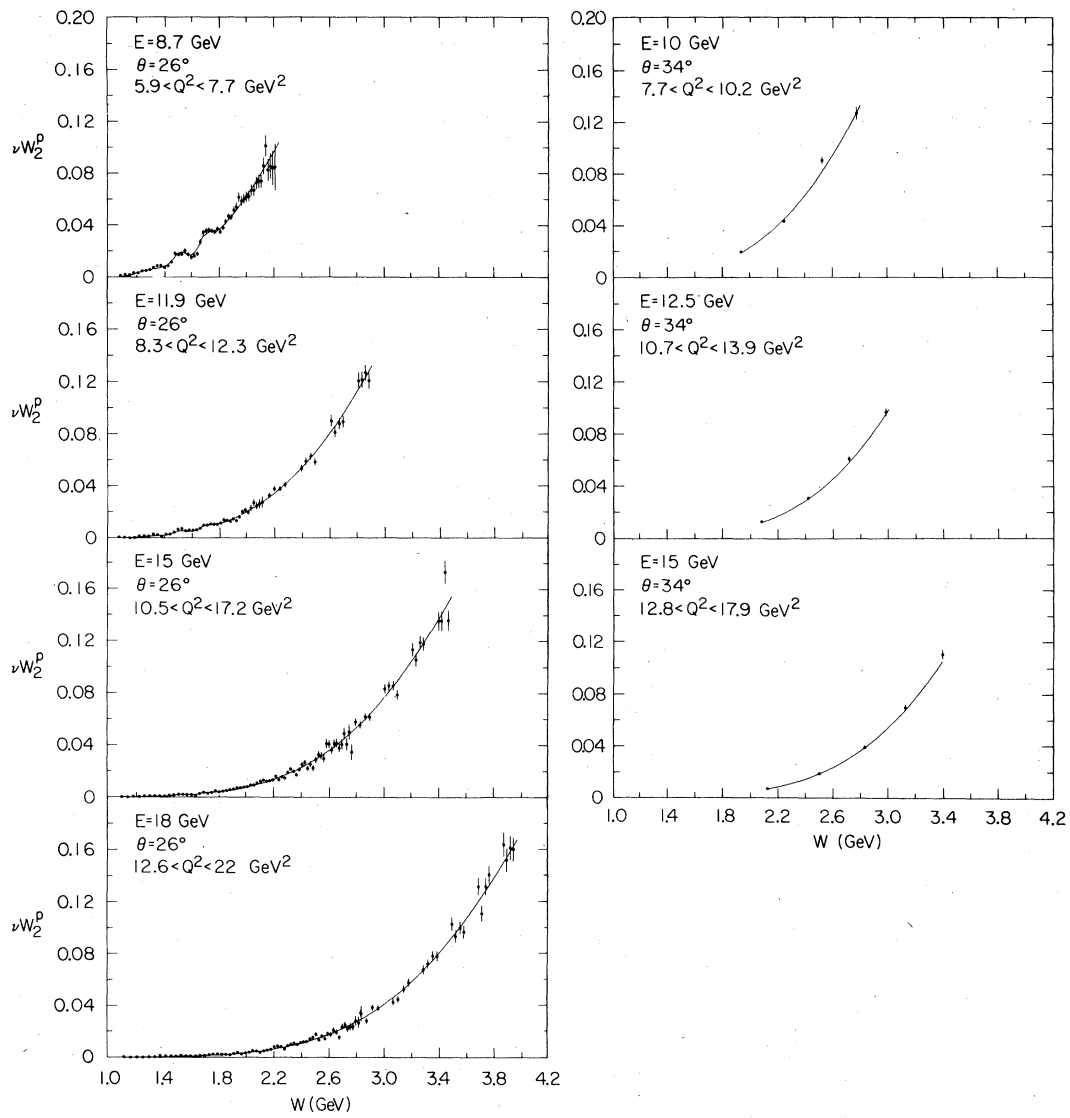

FIG. 12. The quantity νW_2^p extracted from inelastic e-p cross sections measured at 26° and 34° in experiment B assuming $R_p = 0.18$.

however, cancel in the ratio σ_d/σ_p from which σ_n/σ_p is derived (see Sec. V D). Those that do not are the uncertainties in target lengths and densities.

C. Global fit

We have obtained universal fits to the structure functions νW_2^p and νW_2^d, using the data shown in Figs. 9–16 together with similar data[27] from experiment C. As $R_p = R_d = 0.18$ was assumed to extract νW_2 from cross sections for the purpose of the fits, these fits are best used to provide an adequate representation of the inelastic e-p and e-d cross sections in the kinematic regions measured in these three experiments. The fitting program, as well as the explicit functional form of the fits were due to Atwood and Stein.[59,60] The quantity νW_2 was parametrized as follows[61]:

$$\nu W_2(\nu, Q^2) = A(W, Q^2) f(\omega_w)/\omega \ ,$$

where

$$f(\omega_w) = \omega_w \sum_{n=3}^{7} C_n (1 - 1/\omega_w)^n \qquad (5.1)$$

and

$$\omega_w = \frac{2M\nu + a^2}{Q^2 + b^2} .$$

The modulating function $A(W, Q^2)$ contained 12 parameters representing the masses, widths, and

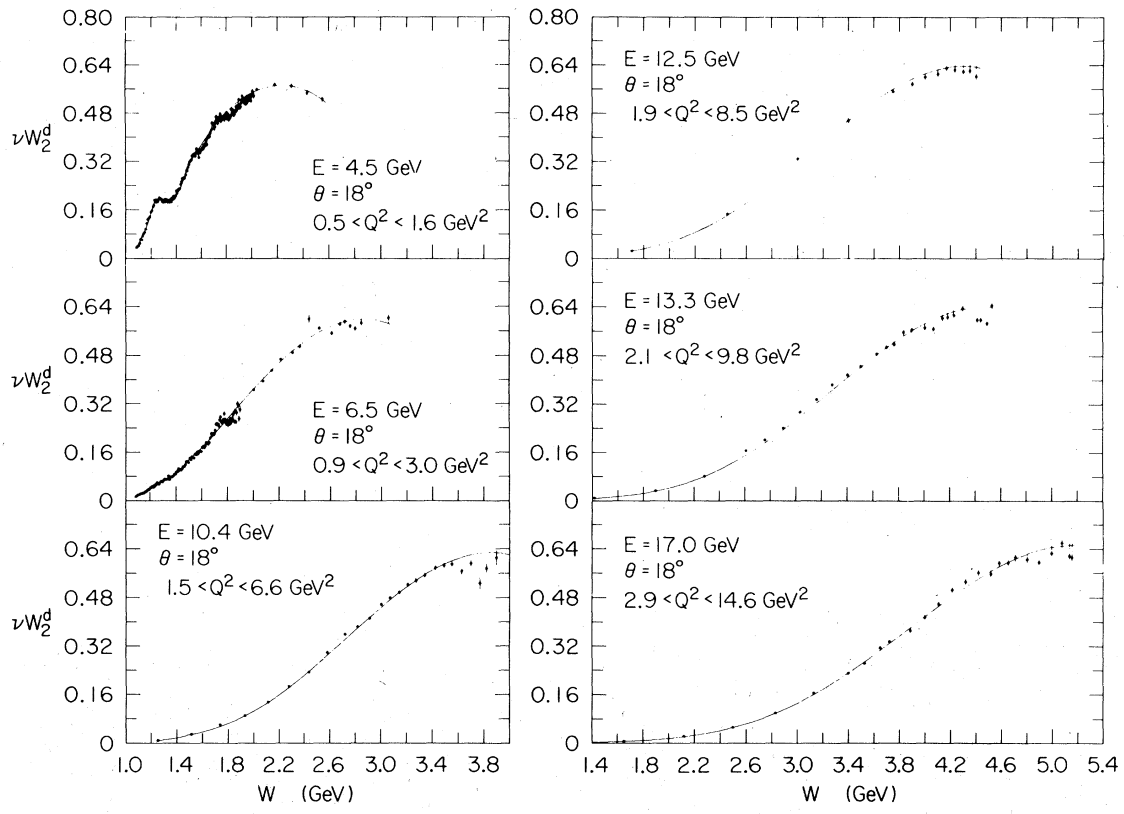

FIG. 13. The quantity νW_2^d extracted from inelastic e-d cross sections measured at 18° in experiment A assuming $R_d = 0.18$.

amplitudes of the cross sections for electroproduction of the four most prominent nucleon resonances, and eight parameters representing the W dependence of the nonresonant background under these resonances. This modulating function was close to unity for $W > 2.0$. Indeed, for $W > 2.5$ GeV, $|[A(W,Q^2)-1]| \leq 0.01$. νW_2 was essentially equal to $f(\omega_w)/\omega$. The scaling variable ω_w, first proposed by Rittenberg and Rubinstein,[62] extends scaling of νW_2 down to values of Q^2 near 0.1 GeV^2. The parameters $C_1 = a^2$, $C_2 = b^2$, C_3 through C_7, and most of the 24 parameters in $A(W,Q^2)$ were determined simultaneously by performing least-squares fits of the form given in Eq. (5.1) to all the data for νW_2^p and νW_2^d from the three experiments. Data from the line of lowest E at each scattering angle in experiments A and C were not included in this sample, however, because of uncertainties in the radiative corrections having to do with extrapolations of the uncorrected cross sections to low E (see Sec. IV D 5). In the case of the deuteron, the function $f(\omega_w)$ had an additional multiplicative factor $(1-e^{-7.7(\omega'-1)})^{-1}$ included to account for deuteron binding effects at small ω' $= \omega + M^2/Q^2$. Best-fit values of C_1 through C_7 are given in Table VIII for the proton and deuteron. Also given in this table are values of these parameters for fits to the neutron data discussed in Sec. V D.

These functional forms provided reasonable fits to the proton and deuteron cross sections, especially in the deep-inelastic region. Values of χ^2 per degree of freedom were 1.59 (2533 data points) for the proton and 1.96 (2303 data points) for the deuteron. Most of the difficulty in fitting the data occurred in the resonance region; the χ^2 per degree of freedom was 1.2 for the proton and 1.4 for the deuteron when the fits were restricted to $W \geq 1.8$ GeV. The accuracy of these fits in modeling the data is seen graphically in Figs. 9–20. Their relevance in regions not yet measured in the SLAC experiments is subject to the assumptions implicit in the fit (mostly the scaling assumption). We emphasize that $R_p = R_d = 0.18$ was assumed to extract νW_2 for these fits, and advise that this assumption should be used with these fits to reconstruct the cross section in the deep-inelastic region.

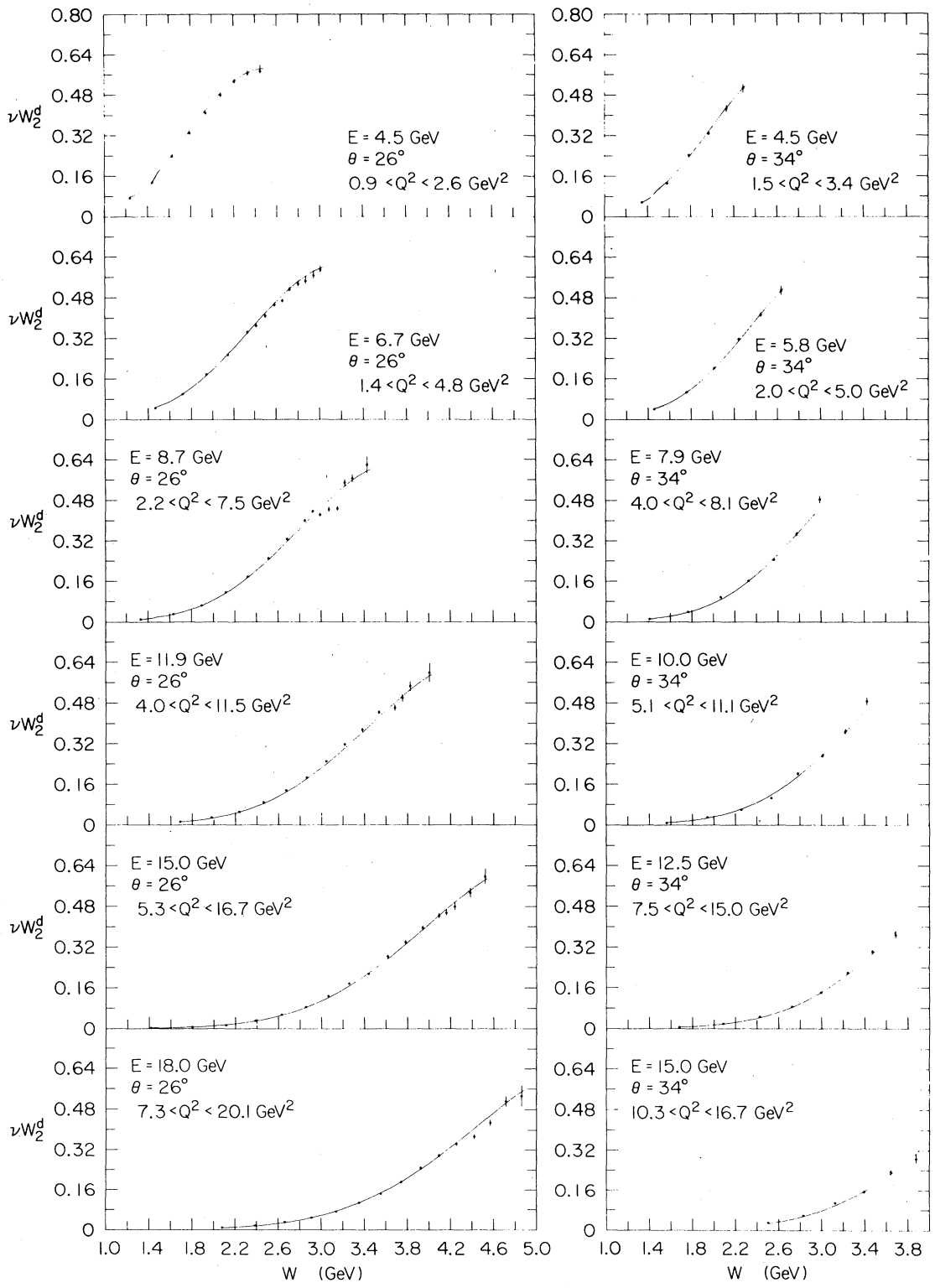

FIG. 14. The quantity νW_2^d extracted from inelastic e-d cross sections measured at 26° and 34° in experiment A assuming $R_d = 0.18$.

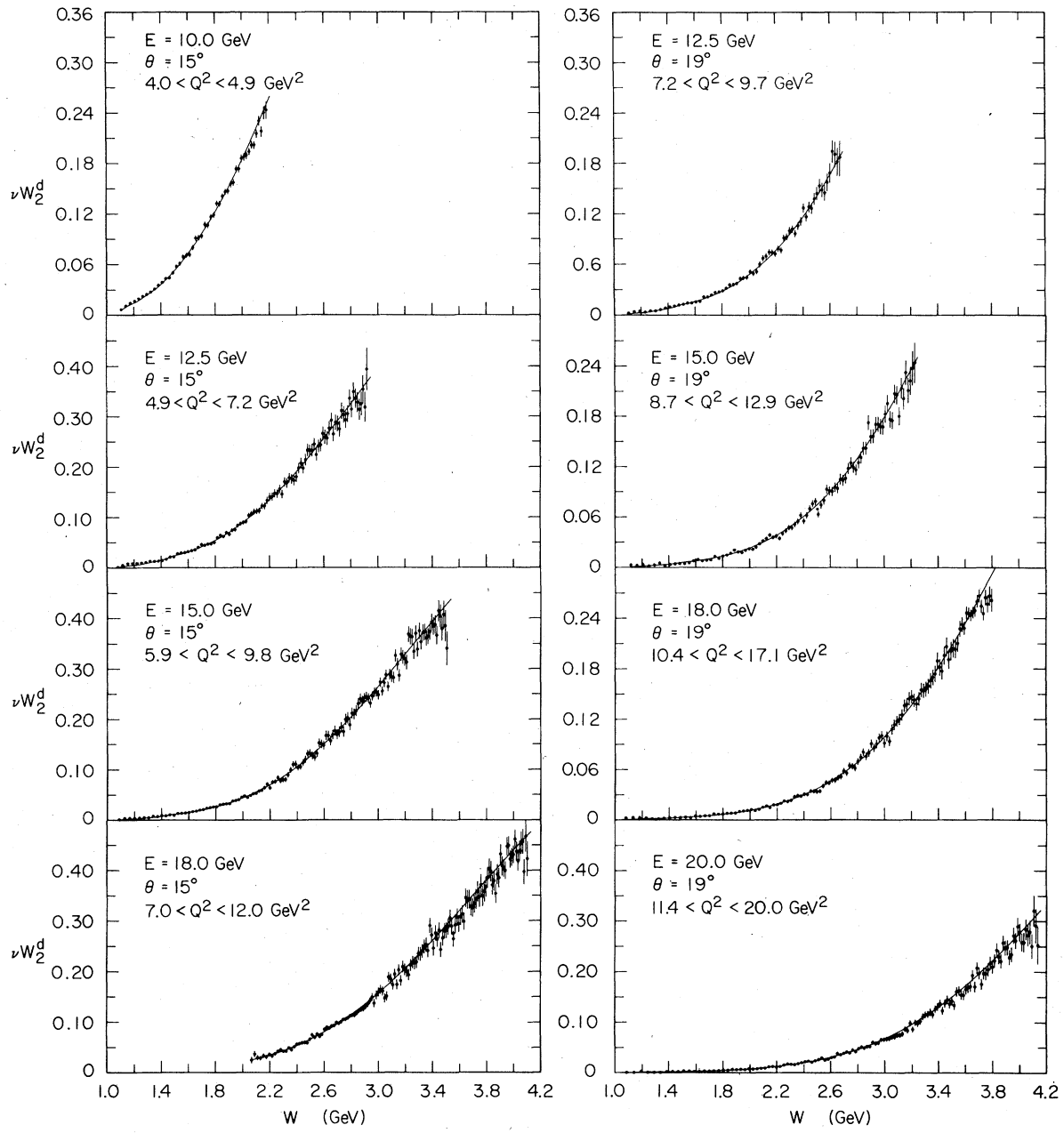

FIG. 15. The quantity νW_2^d extracted from inelastic e-d cross sections measured at 15° and 19° in experiment B assuming $R_d = 0.18$.

D. Neutron cross sections

1. Introduction

Cross sections for inelastic e-n scattering were extracted from the e-d cross sections using an impulse approximation. The method used is that of Atwood and West,[19] with small modifications for off-mass-shell effects.[20,63] In this method, the electron is assumed to scatter incoherently from the proton and neutron, and corrections for Fermi motion of the nucleons within the deuteron, commonly known as smearing corrections, are made. Corrections to the impulse approximation are believed to be small[19,20] at the large values of Q^2 of these experiments. In this section we outline the procedure used in the extraction of e-n cross sections from the e-d data. A detailed discussion of deuteron binding effects is reserved for Appendix C.

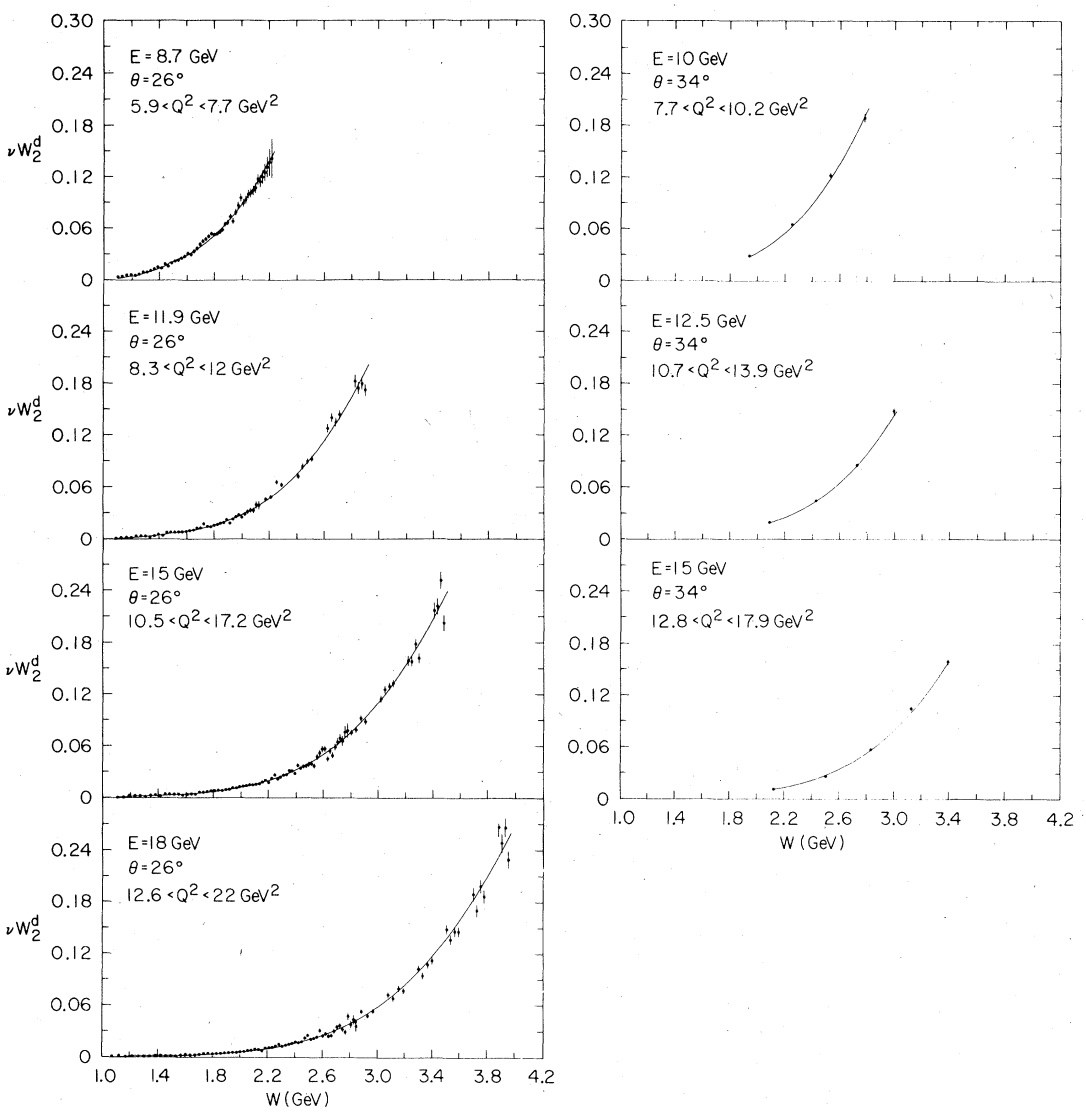

FIG. 16. The quantity νW_2^d extracted from inelastic e-d cross sections measured at 26° and 34° in experiment B assuming $R_d = 0.18$.

2. *Smeared proton cross sections*

The first step in the extraction of the neutron cross sections was the introduction of Fermi-motion effects into the measured proton cross sections. The assumption $R_p = 0.18$ was used together with the global fit to νW_2^p to provide parametrizations of the two-proton structure functions needed in this step. The proton structure functions from this fit were integrated over the momentum distribution of the proton within the deuteron to produce the "smeared" proton structure functions[19,20] W_{1s}^p and W_{2s}^p

$$W_{1s}(\nu,Q^2) = \int d^3p\, |f(\vec{p})|^2 \left(W_1^p(\nu',Q^2,W') + W_2^p(\nu',Q^2,W') \frac{\vec{p}^2 - p_3^2}{2M^2} \right),$$

$$W_{2s}(\nu,Q^2) = \int d^3p\, |f(\vec{p})|^2 \left[\frac{1 - p_3 Q^2}{M\nu' q_3} \left(\frac{\nu'}{\nu}\right)^2 + \left(\frac{\vec{p}^2 - p_3^2}{2M} \right) \frac{Q^2}{q_3^2} \right] W_2(\nu',Q^2,W'). \tag{5.2}$$

As detailed in Appendix C, p is the four-momentum

TABLE V. Combined cross sections from experiments A and B. The cross sections and their errors are in pb/sr GeV.

Point No.	E_p (GeV)	W (GeV)	σ_p	σ_d	σ_n
			$E_0 = 10.00$ GeV $\theta = 14.991°$		
1	6.36	1.84	4 727.8 ± 95.2	7 397.4 ± 124.0	2 590.8 ± 156.1
2	6.26	1.91	5 465.1 ± 96.7	8 120.9 ± 123.0	2 845.8 ± 159.0
3	6.14	1.99	6 237.3 ± 106.7	9 409.3 ± 140.6	3 452.3 ± 182.2
4	6.02	2.06	6 953.9 ± 109.2	10 055.9 ± 143.5	3 404.8 ± 183.2
5	5.88	2.14	7 657.9 ± 134.0	11 432.1 ± 178.4	4 136.5 ± 228.3
			$E_0 = 12.50$ GeV $\theta = 14.991°$		
1	7.64	1.87	1 204.2 ± 28.0	1 752.4 ± 35.2	516.4 ± 43.9
2	7.46	2.00	1 525.1 ± 35.0	2 282.1 ± 45.5	779.6 ± 57.0
3	7.27	2.13	2 100.9 ± 49.8	2 959.5 ± 60.5	918.7 ± 81.3
4	7.06	2.26	2 560.6 ± 66.3	3 678.2 ± 79.6	1 215.5 ± 107.6
5	6.84	2.38	2 975.0 ± 78.2	4 390.8 ± 96.0	1 541.5 ± 127.3
6	6.62	2.51	3 425.5 ± 84.5	5 326.9 ± 108.5	2 059.1 ± 143.0
7	6.38	2.63	3 986.1 ± 98.3	6 149.2 ± 125.7	2 344.8 ± 166.1
8	6.14	2.75	4 573.0 ± 114.4	6 823.3 ± 142.1	2 447.5 ± 188.9
9	5.90	2.87	4 945.8 ± 155.9	7 554.6 ± 191.4	2 820.8 ± 253.7
			$E_0 = 15.00$ GeV $\theta = 14.991°$		
1	8.82	1.87	324.9 ± 6.9	473.1 ± 9.4	119.3 ± 10.6
2	8.64	2.00	441.7 ± 8.9	640.2 ± 12.2	182.1 ± 14.2
3	8.46	2.13	581.8 ± 13.4	842.3 ± 17.2	255.1 ± 21.0
4	8.26	2.26	803.1 ± 19.4	1 076.6 ± 21.8	283.1 ± 29.2
5	8.04	2.40	983.2 ± 25.1	1 456.4 ± 30.4	498.6 ± 40.1
6	7.80	2.54	1 278.6 ± 30.2	1 835.4 ± 39.2	599.7 ± 51.4
7	7.56	2.67	1 476.6 ± 27.9	2 245.0 ± 47.4	827.3 ± 57.2
8	7.32	2.80	1 669.8 ± 33.4	2 653.2 ± 52.8	1 057.4 ± 64.4
9	7.08	2.92	2 010.6 ± 45.9	3 080.7 ± 49.2	1 158.1 ± 69.2
10	6.84	3.04	2 230.4 ± 49.4	3 393.6 ± 51.0	1 260.0 ± 71.8
11	6.60	3.15	2 399.0 ± 52.6	3 853.8 ± 63.8	1 563.3 ± 83.7
12	6.36	3.26	2 694.1 ± 57.4	4 407.5 ± 78.4	1 834.6 ± 101.1
13	6.12	3.36	2 848.8 ± 60.8	4 624.2 ± 81.4	1 899.0 ± 102.9
14	5.88	3.46	3 134.8 ± 86.4	4 875.5 ± 109.4	1 867.1 ± 139.9
			$E_0 = 18.00$ GeV $\theta = 14.991°$		
1	9.68	2.16	183.0 ± 9.0	248.9 ± 11.1	54.9 ± 13.4
2	9.48	2.29	225.3 ± 7.1	338.5 ± 9.2	104.8 ± 10.9
3	9.30	2.41	294.6 ± 7.7	425.8 ± 9.5	127.3 ± 11.8
4	9.12	2.52	373.4 ± 8.6	531.1 ± 10.6	158.8 ± 13.5
5	8.94	2.63	462.2 ± 7.8	662.3 ± 10.7	206.6 ± 13.4
6	8.78	2.73	534.3 ± 8.1	762.9 ± 11.4	240.1 ± 14.2
7	8.61	2.82	594.3 ± 8.8	855.5 ± 12.5	277.3 ± 15.3
8	8.43	2.92	682.9 ± 12.9	991.2 ± 17.6	330.1 ± 21.8
9	8.24	3.02	766.1 ± 19.8	1 130.8 ± 24.8	392.4 ± 31.4
10	8.01	3.13	910.1 ± 22.7	1 380.3 ± 28.1	506.5 ± 37.2
11	7.77	3.25	1 024.4 ± 25.9	1 540.6 ± 32.1	558.4 ± 41.6
12	7.53	3.36	1 164.5 ± 29.5	1 831.6 ± 37.8	718.2 ± 49.8
13	7.29	3.47	1 358.9 ± 33.8	1 964.7 ± 41.4	661.0 ± 55.2
14	7.05	3.58	1 456.7 ± 36.8	2 137.9 ± 45.3	740.7 ± 59.2
15	6.81	3.68	1 590.7 ± 40.3	2 398.1 ± 50.8	873.0 ± 66.5
16	6.57	3.78	1 698.5 ± 42.7	2 660.1 ± 56.6	1 032.8 ± 73.1
17	6.33	3.88	1 830.0 ± 41.8	2 841.6 ± 55.7	1 085.6 ± 71.3
18	6.09	3.97	1 909.3 ± 36.0	3 150.9 ± 53.7	1 321.4 ± 66.8
19	5.85	4.06	2 017.6 ± 45.1	3 243.9 ± 66.7	1 306.2 ± 81.4

TABLE V. *(Continued)*

Point No.	E_p (GeV)	W (GeV)	σ_p	σ_d	σ_n
			$E_0 = 4.50$ GeV $\theta = 18.023°$		
1	2.60	1.81	68 006.2 ± 1180.9	120 966.0 ± 1730.4	51 571.9 ± 2055.7
2	2.55	1.85	71 785.4 ± 1193.3	121 351.0 ± 1735.8	50 518.7 ± 2111.9
3	2.51	1.88	72 604.5 ± 1145.3	124 614.0 ± 1767.5	54 616.3 ± 2141.4
4	2.46	1.90	75 018.4 ± 1173.9	126 486.0 ± 1764.0	54 912.6 ± 2175.4
5	2.41	1.93	72 415.7 ± 1185.4	124 803.0 ± 1736.2	55 876.7 ± 2142.9
6	2.36	1.96	72 584.2 ± 1194.2	126 035.0 ± 1755.5	56 620.4 ± 2163.8
7	2.31	1.99	73 455.8 ± 1292.8	126 512.0 ± 1830.8	55 859.4 ± 2285.4
8	2.25	2.03	72 428.1 ± 1373.0	129 445.0 ± 2116.8	59 594.3 ± 2586.9
9	2.00	2.17	71 258.0 ± 1586.8	127 764.0 ± 2242.9	58 745.6 ± 2816.7
10	1.75	2.30	67 920.3 ± 1620.7	125 274.0 ± 2741.8	59 290.6 ± 3255.8
11	1.50	2.42	67 392.7 ± 2332.0	122 633.0 ± 2962.4	56 963.7 ± 3837.5
12	1.25	2.54	64 626.3 ± 2936.1	124 708.0 ± 5735.9	61 758.2 ± 6606.2
			$E_0 = 6.50$ GeV $\theta = 18.023°$		
1	3.88	1.82	14 770.5 ± 335.5	23 450.4 ± 392.0	8 456.4 ± 501.3
2	3.81	1.87	15 728.5 ± 351.1	24 853.4 ± 412.0	9 582.5 ± 535.7
3	3.61	2.00	19 007.8 ± 421.7	30 058.6 ± 503.4	11 990.1 ± 677.8
4	3.50	2.07	19 315.3 ± 419.5	31 662.8 ± 509.8	13 270.9 ± 671.3
5	3.38	2.14	20 700.3 ± 459.9	33 798.5 ± 565.4	14 052.3 ± 749.5
6	3.26	2.21	21 818.5 ± 486.9	35 895.7 ± 589.5	15 024.8 ± 792.1
7	3.10	2.30	21 936.2 ± 492.9	36 857.3 ± 651.5	15 819.5 ± 833.3
8	2.99	2.36	22 033.2 ± 488.8	37 895.5 ± 646.2	16 737.2 ± 822.9
9	2.85	2.43	23 635.2 ± 517.1	44 096.6 ± 1460.5	21 415.6 ± 1764.7
10	2.70	2.51	24 321.9 ± 533.7	41 515.8 ± 725.8	18 025.9 ± 936.3
11	2.50	2.61	23 333.1 ± 557.6	40 244.8 ± 763.7	17 655.7 ± 944.4
12	2.36	2.67	23 234.0 ± 522.3	42 581.7 ± 824.8	20 101.6 ± 988.4
13	2.28	2.71	23 936.4 ± 598.2	43 414.7 ± 837.7	20 225.0 ± 1046.7
14	2.19	2.75	21 949.9 ± 600.0	42 514.4 ± 866.6	21 279.6 ± 1033.4
15	2.11	2.79	23 030.4 ± 615.7	42 341.8 ± 880.8	20 001.9 ± 1054.3
16	2.00	2.84	25 858.8 ± 790.5	44 367.0 ± 945.6	19 207.1 ± 1260.2
17	1.50	3.05	26 734.3 ± 1296.5	51 515.4 ± 1643.0	25 525.9 ± 2176.7
			$E_0 = 8.60$ GeV $\theta = 18.023°$		
1	5.02	1.83	3 200.4 ± 61.4		
2	4.92	1.91	3 823.1 ± 79.8		
3	4.78	2.01	4 511.4 ± 88.8		
4	4.63	2.10	5 225.9 ± 88.4		
5	4.50	2.19	6 090.3 ± 113.2		
6	4.33	2.29	6 563.5 ± 129.9		
7	4.16	2.39	7 271.3 ± 142.3		
8	4.00	2.48	7 755.9 ± 180.2		
9	3.83	2.57	8 463.9 ± 181.1		
10	3.66	2.66	8 909.8 ± 189.0		
11	3.50	2.74	9 331.6 ± 190.2		
12	3.35	2.81	9 988.9 ± 206.9		
13	3.21	2.88	9 803.0 ± 209.7		
14	3.00	2.98	10 604.6 ± 221.1		
15	2.90	3.02	10 877.0 ± 247.3		
16	2.79	3.07	11 178.4 ± 263.0		
17	2.68	3.12	11 033.5 ± 256.0		
18	2.59	3.16	11 403.5 ± 270.7		
19	2.50	3.20	11 378.1 ± 282.9		
20	2.33	3.27	11 275.2 ± 335.2		
21	2.16	3.34	12 086.9 ± 358.8		
22	2.00	3.40	11 899.0 ± 433.7		
23	1.50	3.60	13 693.7 ± 1032.8		

TABLE V. *(Continued)*

Point No.	E_p (GeV)	W (GeV)	σ_p	σ_d	σ_n
			$E_0 = 10.39$ GeV $\theta = 18.023°$		
1	5.75	1.93	1 208.5 ± 52.5	1 827.7 ± 53.5	642.7 ± 73.2
2	5.49	2.11	1 786.0 ± 67.7	2 633.9 ± 75.7	910.2 ± 102.7
3	5.25	2.28	2 410.6 ± 81.7	3 535.3 ± 82.8	1 228.3 ± 120.5
4	4.99	2.43	2 915.7 ± 79.1	4 356.5 ± 85.1	1 572.6 ± 118.6
5	4.75	2.58	3 523.9 ± 45.3	5 452.7 ± 116.9	2 090.5 ± 133.6
6	4.50	2.71	4 019.8 ± 71.7	6 484.8 ± 109.8	2 649.1 ± 138.7
7	4.31	2.81	4 512.0 ± 100.8	6 896.0 ± 126.9	2 572.0 ± 169.9
8	4.12	2.91	4 773.5 ± 112.9	7 386.3 ± 132.5	2 805.4 ± 180.0
9	3.93	3.00	5 032.6 ± 112.2	8 208.7 ± 142.0	3 380.6 ± 188.2
10	3.79	3.07	5 084.8 ± 108.3	8 589.0 ± 144.9	3 710.5 ± 185.6
11	3.64	3.14	5 340.9 ± 98.8	8 970.3 ± 152.9	3 836.5 ± 186.8
12	3.50	3.20	5 550.7 ± 140.6	9 487.9 ± 173.2	4 148.5 ± 228.6
13	3.35	3.27	5 863.2 ± 143.4	9 846.5 ± 199.2	4 194.2 ± 252.5
14	3.19	3.34	6 330.5 ± 164.6	10 294.4 ± 202.0	4 175.2 ± 270.4
15	3.00	3.42	6 416.8 ± 163.2	10 963.1 ± 211.7	4 761.3 ± 275.1
16	2.84	3.49	6 668.9 ± 152.3	11 344.8 ± 213.9	4 889.9 ± 269.0
17	2.69	3.55	6 674.3 ± 161.4	11 707.9 ± 230.0	5 247.4 ± 284.2
18	2.50	3.63	6 518.8 ± 170.5	11 657.9 ± 296.6	5 343.5 ± 330.7
19	2.32	3.70	7 228.0 ± 193.6	12 657.6 ± 323.2	5 643.3 ± 374.5
20	2.13	3.77	6 824.3 ± 325.6	11 804.2 ± 492.8	5 172.4 ± 525.5
21	2.00	3.82	7 349.1 ± 401.9	13 430.4 ± 453.0	6 296.0 ± 572.5
22	1.79	3.90	8 538.1 ± 421.4	15 295.3 ± 703.9	6 993.9 ± 827.5
23	1.50	4.01	9 184.7 ± 766.8	17 537.8 ± 1161.8	8 615.9 ± 1414.2
			$E_0 = 12.50$ GeV $\theta = 18.023°$		
1	5.91	2.45	1 053.8 ± 29.3	1 539.7 ± 29.2	523.6 ± 42.9
2	4.94	3.00	2 093.9 ± 61.6	3 369.0 ± 67.1	1 370.5 ± 95.8
3	4.12	3.40	2 967.6 ± 94.8	4 775.2 ± 102.8	1 924.9 ± 144.8
4	3.31	3.75	3 768.9 ± 115.4	6 222.2 ± 94.9	2 581.6 ± 153.6
5	2.94	3.90	3 937.0 ± 124.7	6 864.0 ± 158.1	3 058.0 ± 202.1
6	2.69	4.00	4 336.0 ± 144.1	7 502.9 ± 177.1	3 302.8 ± 232.4
7	2.43	4.10	4 715.9 ± 186.1	8 128.6 ± 224.0	3 552.7 ± 297.6
8	2.25	4.17	4 951.7 ± 218.1	8 801.2 ± 271.0	3 996.8 ± 358.8
9	2.07	4.23	5 029.7 ± 259.7	9 214.2 ± 320.6	4 334.5 ± 416.1
10	1.88	4.30	5 265.4 ± 322.2	9 759.9 ± 372.1	4 649.1 ± 490.3
11	1.74	4.35	5 727.5 ± 393.1	10 366.7 ± 662.1	4 800.3 ± 779.8
12	1.60	4.40	5 303.1 ± 968.1	10 725.1 ± 684.9	5 586.8 ± 1095.1
			$E_0 = 13.30$ GeV $\theta = 18.023°$		
1	7.00	1.89	201.0 ± 13.9	307.9 ± 13.2	90.3 ± 17.3
2	6.50	2.27	543.6 ± 23.4	726.6 ± 19.9	190.3 ± 31.9
3	6.00	2.60	915.5 ± 32.5	1 439.0 ± 33.9	559.0 ± 50.5
4	5.75	2.75	1 091.5 ± 29.3	1 729.1 ± 30.8	684.9 ± 44.0
5	5.50	2.89	1 339.3 ± 32.6	2 052.7 ± 35.5	771.9 ± 50.0
6	5.25	3.02	1 564.4 ± 38.5	2 502.9 ± 43.6	1 009.8 ± 61.2
7	5.00	3.15	1 862.6 ± 45.1	2 862.5 ± 53.7	1 080.1 ± 74.7
8	4.75	3.28	1 994.5 ± 55.3	3 298.0 ± 59.4	1 393.0 ± 85.2
9	4.50	3.40	2 400.7 ± 65.5	3 607.6 ± 68.9	1 300.8 ± 102.1
10	4.27	3.50	2 439.0 ± 49.4	3 900.7 ± 62.0	1 559.1 ± 82.1
11	4.00	3.62	2 650.8 ± 55.0	4 329.7 ± 75.1	1 781.4 ± 96.4
12	3.82	3.70	2 838.8 ± 64.8	4 599.4 ± 83.7	1 865.5 ± 109.9
13	3.68	3.76	2 778.4 ± 85.1	4 758.9 ± 99.0	2 086.1 ± 132.1
14	3.50	3.83	2 982.1 ± 93.8	5 227.3 ± 109.1	2 357.0 ± 148.7
15	3.34	3.90	3 332.7 ± 92.5	5 411.1 ± 106.8	2 189.9 ± 148.4
16	3.09	4.00	3 272.9 ± 96.8	5 700.0 ± 129.2	2 538.9 ± 162.9
17	2.92	4.07	3 556.0 ± 104.5	5 836.0 ± 158.1	2 390.1 ± 190.1
18	2.74	4.14	3 319.4 ± 125.1	6 429.8 ± 157.0	3 228.7 ± 198.0
19	2.63	4.18	3 921.5 ± 136.9	6 617.8 ± 203.1	2 814.5 ± 251.8
20	2.50	4.23	3 634.6 ± 164.0	6 907.9 ± 213.1	3 394.6 ± 266.7
21	2.31	4.30	4 077.9 ± 200.1	7 532.9 ± 245.3	3 582.7 ± 323.9

TABLE V. *(Continued)*

Point No.	E_p (GeV)	W (GeV)	σ_p	σ_d	σ_n
			$E_0 = 13.30$ GeV $\theta = 18.023°$		
22	2.00	4.41	4 387.1 ± 248.4	7 846.9 ± 300.3	3 586.2 ± 379.9
23	1.93	4.44	4 114.3 ± 275.8	8 057.3 ± 372.2	4 072.2 ± 437.9
24	1.78	4.49	4 499.3 ± 364.8	8 376.1 ± 506.1	4 008.1 ± 589.7
25	1.67	4.53	4 170.9 ± 389.2	9 679.3 ± 646.9	5 659.6 ± 749.4
			$E_0 = 17.00$ GeV $\theta = 18.023°$		
1	7.99	2.11	62.3 ± 1.7	93.6 ± 2.1	23.1 ± 2.4
2	7.50	2.49	146.6 ± 3.7	213.7 ± 4.2	64.2 ± 5.4
3	7.00	2.83	272.2 ± 7.7	404.2 ± 7.3	137.4 ± 10.5
4	6.50	3.12	430.6 ± 10.1	672.3 ± 12.1	257.7 ± 16.1
5	6.00	3.40	627.4 ± 17.5	942.1 ± 18.2	340.7 ± 25.9
6	5.75	3.52	741.2 ± 21.6	1 086.2 ± 22.0	375.3 ± 31.7
7	5.50	3.65	806.3 ± 22.4	1 308.2 ± 25.9	538.2 ± 35.5
8	5.35	3.72	881.7 ± 25.5	1 405.4 ± 28.8	562.4 ± 39.9
9	5.00	3.88	986.7 ± 24.9	1 594.5 ± 36.7	650.2 ± 45.0
10	4.75	3.99	1 074.4 ± 37.5	1 815.0 ± 41.7	787.4 ± 56.6
11	4.50	4.10	1 233.8 ± 39.2	2 051.1 ± 44.5	868.2 ± 61.5
12	4.25	4.21	1 387.7 ± 43.5	2 315.6 ± 53.1	983.2 ± 73.1
13	4.00	4.31	1 501.7 ± 52.7	2 511.1 ± 58.8	1 066.7 ± 83.6
14	3.75	4.42	1 658.7 ± 61.0	2 746.5 ± 69.2	1 147.8 ± 98.8
15	3.50	4.51	1 670.9 ± 57.8	2 841.6 ± 71.9	1 230.0 ± 94.1
16	3.33	4.58	1 743.0 ± 61.6	3 112.4 ± 83.5	1 432.4 ± 107.8
17	3.15	4.65	1 918.1 ± 69.5	3 229.5 ± 85.6	1 374.5 ± 114.5
18	3.00	4.71	2 023.5 ± 75.9	3 436.4 ± 93.4	1 478.2 ± 126.2
19	2.75	4.80	1 898.1 ± 95.0	3 605.9 ± 113.1	1 773.9 ± 144.4
20	2.50	4.89	2 163.1 ± 111.1	3 797.1 ± 143.7	1 700.2 ± 177.5
21	2.22	4.99	2 383.3 ± 182.9	4 359.4 ± 217.7	2 049.2 ± 283.4
22	2.00	5.07	2 045.2 ± 218.1	4 997.7 ± 273.4	3 034.8 ± 334.2
23	1.82	5.13	2 659.0 ± 292.4	5 017.8 ± 413.9	2 438.4 ± 491.0
24	1.77	5.15	2 822.4 ± 310.2	5 118.7 ± 472.6	2 376.8 ± 551.5
			$E_0 = 12.50$ GeV $\theta = 18.996°$		
1	6.43	1.87	216.5 ± 5.4	319.8 ± 7.0	85.0 ± 8.2
2	6.25	2.02	322.3 ± 7.2	442.7 ± 10.3	112.5 ± 12.1
3	6.07	2.16	433.3 ± 9.8	633.7 ± 13.1	192.2 ± 16.6
4	5.88	2.30	598.3 ± 12.6	820.4 ± 15.3	234.5 ± 20.1
5	5.65	2.45	765.2 ± 16.8	1 115.4 ± 21.3	374.8 ± 27.9
6	5.41	2.61	956.5 ± 30.6	1 443.8 ± 38.8	525.0 ± 50.8
			$E_0 = 15.00$ GeV $\theta = 18.996°$		
1	7.27	1.87	52.3 ± 2.0	86.1 ± 2.5	23.5 ± 2.6
2	7.09	2.03	89.2 ± 2.5	123.3 ± 3.0	25.6 ± 3.4
3	6.91	2.18	131.5 ± 3.9	185.7 ± 4.6	47.4 ± 5.6
4	6.73	2.33	178.9 ± 5.5	252.1 ± 6.5	69.9 ± 8.2
5	6.55	2.46	225.5 ± 7.0	331.7 ± 8.0	106.5 ± 10.2
6	6.36	2.59	313.3 ± 8.4	433.2 ± 10.1	125.0 ± 13.2
7	6.13	2.74	388.0 ± 9.4	560.0 ± 12.1	182.7 ± 15.3
8	5.89	2.89	502.5 ± 12.2	756.3 ± 15.4	271.6 ± 20.4
9	5.65	3.03	619.8 ± 15.4	902.2 ± 19.1	306.3 ± 25.1
10	5.41	3.17	741.9 ± 22.3	1 056.4 ± 27.3	343.8 ± 35.7
			$E_0 = 18.02$ GeV $\theta = 18.996°$		
1	8.15	1.85	12.9 ± 0.5	22.7 ± 0.7	4.5 ± 0.6
2	8.00	2.00	20.8 ± 0.6	33.0 ± 0.8	6.5 ± 0.7
3	7.79	2.19	36.1 ± 0.9	51.7 ± 1.2	10.2 ± 1.2
4	7.55	2.39	55.9 ± 1.5	83.4 ± 1.9	23.0 ± 2.2
5	7.31	2.58	84.6 ± 2.2	119.6 ± 2.7	32.2 ± 3.2
6	7.07	2.75	119.1 ± 3.0	174.8 ± 3.7	54.8 ± 4.6
7	6.83	2.91	162.5 ± 4.1	246.1 ± 5.1	85.3 ± 6.6

TABLE V. *(Continued)*

Point No.	E_p (GeV)	W (GeV)	σ_p	σ_d	σ_n
			$E_0 = 18.02$ GeV $\theta = 18.996°$		
8	6.59	3.07	207.7 ± 5.2	305.5 ± 6.5	102.6 ± 8.3
9	6.35	3.21	250.3 ± 6.5	406.0 ± 8.5	164.0 ± 10.9
10	6.11	3.35	340.6 ± 8.5	481.4 ± 10.2	152.6 ± 13.8
11	5.87	3.49	380.4 ± 9.1	571.7 ± 11.9	206.3 ± 15.1
12	5.63	3.62	446.2 ± 6.4	697.8 ± 10.0	270.6 ± 12.2
13	5.39	3.74	511.0 ± 7.6	774.5 ± 11.8	285.0 ± 14.2
			$E_0 = 20.00$ GeV $\theta = 18.996°$		
1	8.60	1.88	6.3 ± 0.2	12.0 ± 0.3	2.2 ± 0.3
2	8.40	2.08	12.6 ± 0.4	19.0 ± 0.5	2.7 ± 0.4
3	8.19	2.28	20.7 ± 0.6	31.2 ± 0.8	6.4 ± 0.8
4	7.98	2.46	31.1 ± 0.9	48.8 ± 1.2	13.8 ± 1.3
5	7.76	2.64	47.6 ± 1.3	68.2 ± 1.6	17.6 ± 1.9
6	7.52	2.82	69.1 ± 1.8	97.6 ± 2.2	26.7 ± 2.7
7	7.28	2.98	93.6 ± 2.4	133.0 ± 2.9	39.0 ± 3.6
8	7.04	3.14	124.2 ± 3.2	168.7 ± 3.7	46.0 ± 4.7
9	6.80	3.29	166.9 ± 4.3	228.6 ± 5.0	65.4 ± 6.7
10	6.56	3.44	197.6 ± 5.2	283.9 ± 6.2	92.1 ± 8.1
11	6.32	3.58	238.1 ± 6.2	336.4 ± 7.4	106.4 ± 9.7
12	6.08	3.71	274.4 ± 7.4	413.9 ± 9.2	150.2 ± 11.8
13	5.84	3.84	333.6 ± 9.0	501.3 ± 11.2	181.2 ± 14.8
14	5.60	3.96	377.1 ± 10.4	570.6 ± 13.1	209.1 ± 17.0
15	5.36	4.09	404.7 ± 15.9	626.0 ± 20.0	238.6 ± 24.8
			$E_0 = 4.50$ GeV $\theta = 25.993°$		
1	2.00	1.94	13 720.1 ± 366.0	21 740.0 ± 428.7	8 767.8 ± 486.7
2	1.80	2.08	15 673.6 ± 416.5	25 083.4 ± 544.2	10 048.4 ± 600.2
3	1.60	2.21	16 566.3 ± 520.2	28 064.9 ± 684.9	12 126.9 ± 782.2
4	1.40	2.33	17 039.9 ± 674.8	30 607.4 ± 948.1	14 158.0 ± 1105.1
5	1.20	2.45	19 788.4 ± 1234.2	32 754.7 ± 1903.7	13 523.7 ± 2252.8
			$E_0 = 6.70$ GeV $\theta = 25.993°$		
1	3.00	1.94	1 868.1 ± 57.1	2 869.6 ± 60.7	1 090.2 ± 75.0
2	2.75	2.14	2 699.7 ± 84.1	4 016.9 ± 85.5	1 444.0 ± 108.2
3	2.50	2.32	3 466.5 ± 106.9	5 445.2 ± 116.9	2 140.9 ± 142.5
4	2.38	2.40	3 733.7 ± 116.2	5 877.3 ± 134.1	2 310.1 ± 161.2
5	2.25	2.49	3 870.0 ± 128.9	6 564.8 ± 152.2	2 870.4 ± 182.7
6	2.12	2.57	4 383.9 ± 152.8	7 364.2 ± 173.9	3 165.1 ± 212.8
7	2.00	2.64	4 985.8 ± 152.6	7 746.1 ± 176.2	2 943.0 ± 209.7
8	1.89	2.71	5 218.1 ± 165.3	8 650.0 ± 200.1	3 625.9 ± 234.9
9	1.75	2.79	5 519.9 ± 199.6	9 299.8 ± 259.8	3 975.0 ± 306.9
10	1.63	2.86	5 640.8 ± 225.1	9 807.2 ± 315.2	4 361.5 ± 369.7
11	1.50	2.93	5 624.2 ± 308.6	10 636.6 ± 449.4	5 213.2 ± 535.1
12	1.38	3.00	6 902.6 ± 391.8	11 584.3 ± 551.1	4 887.7 ± 665.9
			$E_0 = 8.70$ GeV $\theta = 25.993°$		
1	3.79	1.85	298.6 ± 7.1	431.7 ± 8.6	119.8 ± 10.6
2	3.67	1.96	427.8 ± 12.0	597.6 ± 14.0	173.5 ± 18.8
3	3.54	2.08	523.1 ± 14.9	770.9 ± 18.2	260.3 ± 23.5
4	3.42	2.18	677.2 ± 35.7	952.6 ± 41.1	297.7 ± 55.2
5	3.25	2.32	852.0 ± 24.0	1 289.6 ± 25.8	473.7 ± 31.2
6	3.00	2.51	1 174.8 ± 33.1	1 831.9 ± 36.5	711.4 ± 43.5
7	2.75	2.68	1 506.4 ± 43.9	2 433.1 ± 49.2	996.7 ± 58.5
8	2.50	2.85	1 909.8 ± 54.6	3 071.3 ± 62.4	1 244.2 ± 73.3
9	2.39	2.92	2 236.6 ± 63.5	3 412.6 ± 69.1	1 264.3 ± 82.4
10	2.27	2.99	2 186.1 ± 65.3	3 372.1 ± 81.7	1 269.8 ± 95.2
11	2.14	3.07	2 466.0 ± 75.3	3 646.5 ± 108.4	1 266.5 ± 123.6
12	2.00	3.15	2 427.6 ± 90.5	3 795.6 ± 109.1	1 453.2 ± 133.6
13	1.88	3.22	2 636.4 ± 123.6	4 821.7 ± 157.4	2 289.3 ± 193.0
14	1.75	3.29	2 898.8 ± 158.7	5 161.7 ± 181.3	2 368.6 ± 234.2
15	1.50	3.43	3 332.7 ± 240.4	6 241.1 ± 370.2	3 025.1 ± 440.3

TABLE V. *(Continued)*

Point No.	E_p (GeV)	W (GeV)	σ_p	σ_d	σ_n
			$E_0 = 11.88$ GeV $\theta = 25.993°$		
1	4.61	1.86	36.7 ± 1.7	54.5 ± 2.0	11.8 ± 2.2
2	4.52	1.96	48.9 ± 1.9	68.6 ± 2.2	14.8 ± 2.5
3	4.41	2.07	70.3 ± 3.2	97.4 ± 3.7	22.5 ± 4.5
4	4.25	2.23	107.1 ± 3.2	160.8 ± 3.9	51.4 ± 5.1
5	4.00	2.46	170.8 ± 4.6	246.9 ± 5.5	78.6 ± 7.1
6	3.75	2.67	258.0 ± 7.0	405.0 ± 8.9	155.5 ± 11.8
7	3.50	2.86	370.3 ± 10.3	535.4 ± 12.5	179.3 ± 16.5
8	3.25	3.04	502.6 ± 15.0	770.0 ± 16.0	289.1 ± 19.7
9	3.00	3.21	615.0 ± 18.9	1 005.0 ± 22.0	418.1 ± 26.3
10	2.75	3.38	790.8 ± 25.7	1 244.2 ± 28.6	487.0 ± 35.2
11	2.50	3.53	908.4 ± 30.9	1 551.0 ± 36.6	682.2 ± 44.2
12	2.25	3.68	976.1 ± 44.4	1 718.0 ± 56.7	782.8 ± 69.7
13	2.13	3.75	1 181.3 ± 43.4	1 931.2 ± 67.6	794.0 ± 77.4
14	2.00	3.82	1 243.8 ± 49.8	2 192.9 ± 86.9	997.4 ± 97.7
15	1.67	4.00	1 699.0 ± 189.2	2 736.7 ± 183.3	1 091.3 ± 263.7
			$E_0 = 15.00$ GeV $\theta = 25.993°$		
1	5.18	1.89	8.1 ± 0.3	13.2 ± 0.4	2.5 ± 0.3
2	5.04	2.07	14.3 ± 0.4	20.7 ± 0.5	3.5 ± 0.5
3	4.89	2.24	21.1 ± 0.6	31.8 ± 0.7	8.0 ± 0.8
4	4.73	2.41	32.8 ± 0.9	47.9 ± 1.1	12.8 ± 1.3
5	4.57	2.56	48.2 ± 1.5	68.4 ± 1.8	18.8 ± 2.2
6	4.41	2.71	64.8 ± 2.3	94.2 ± 2.7	28.9 ± 3.4
7	4.25	2.86	89.8 ± 2.4	127.3 ± 2.9	38.6 ± 3.7
8	4.00	3.06	129.9 ± 3.1	196.0 ± 3.9	69.8 ± 5.1
9	3.75	3.26	182.6 ± 4.6	264.1 ± 5.6	88.0 ± 7.4
10	3.50	3.44	240.3 ± 7.2	371.2 ± 9.0	140.9 ± 12.0
11	3.25	3.61	296.2 ± 11.7	482.7 ± 11.9	199.9 ± 15.7
12	3.00	3.78	377.5 ± 14.5	607.6 ± 15.7	246.8 ± 20.1
13	2.75	3.94	454.7 ± 18.5	746.1 ± 20.5	311.1 ± 26.2
14	2.50	4.09	528.1 ± 19.7	891.6 ± 25.8	385.9 ± 30.8
15	2.39	4.16	590.3 ± 27.0	942.9 ± 26.1	375.6 ± 35.8
16	2.25	4.24	607.4 ± 33.0	1 036.2 ± 36.6	453.1 ± 48.1
17	2.00	4.38	620.8 ± 48.5	1 259.2 ± 50.4	666.1 ± 69.1
18	1.75	4.52	905.6 ± 62.6	1 562.8 ± 87.1	688.9 ± 106.7
			$E_0 = 18.02$ GeV $\theta = 25.993°$		
1	5.63	1.89	2.2 ± 0.1	3.9 ± 0.1	0.4 ± 0.1
2	5.49	2.09	3.8 ± 0.2	6.6 ± 0.2	1.2 ± 0.2
3	5.35	2.26	6.8 ± 0.3	10.9 ± 0.3	2.3 ± 0.3
4	5.20	2.44	11.1 ± 0.4	16.5 ± 0.5	3.7 ± 0.5
5	5.04	2.61	14.9 ± 0.5	23.1 ± 0.7	6.7 ± 0.7
6	4.88	2.78	22.8 ± 1.0	33.9 ± 1.2	9.7 ± 1.5
7	4.75	2.91	31.1 ± 1.0	44.2 ± 1.3	12.3 ± 1.6
8	4.50	3.14	45.9 ± 1.4	68.8 ± 1.8	23.0 ± 2.2
9	4.25	3.35	70.7 ± 2.0	99.2 ± 2.3	30.0 ± 3.0
10	4.00	3.55	96.6 ± 2.7	141.9 ± 3.3	48.4 ± 4.2
11	3.75	3.74	131.7 ± 3.7	189.9 ± 4.5	63.0 ± 5.9
12	3.50	3.92	169.9 ± 5.3	268.8 ± 6.5	106.3 ± 8.8
13	3.25	4.09	224.2 ± 8.3	327.6 ± 9.2	112.5 ± 11.8
14	3.00	4.25	274.7 ± 12.2	399.2 ± 11.3	135.4 ± 15.9
15	2.75	4.42	304.9 ± 15.0	460.4 ± 15.0	167.6 ± 20.6
16	2.51	4.57	340.4 ± 18.6	566.0 ± 20.8	239.8 ± 27.3
17	2.26	4.72	411.7 ± 31.1	731.6 ± 33.2	337.1 ± 45.1
18	2.01	4.86	430.8 ± 48.6	837.1 ± 67.4	424.8 ± 83.7

TABLE V. *(Continued)*

Point No.	E_p (GeV)	W (GeV)	σ_p	σ_d	σ_n
			$E_0=4.50$ GeV $\theta=33.992°$		
1	1.60	1.97	4152.7 ± 134.1	6161.4 ± 148.2	2220.5 ± 182.1
2	1.40	2.13	4965.4 ± 198.8	8225.9 ± 287.9	3493.2 ± 337.5
3	1.20	2.29	6216.1 ± 306.1	10296.5 ± 395.1	4327.3 ± 486.5
			$E_0=5.80$ GeV $\theta=33.992°$		
1	2.00	2.01	1149.4 ± 37.8	1771.2 ± 38.6	673.2 ± 48.6
2	1.75	2.24	1805.0 ± 58.7	2872.1 ± 62.7	1156.0 ± 77.2
3	1.50	2.44	2542.8 ± 92.1	3965.4 ± 105.5	1529.6 ± 130.3
4	1.25	2.63	3280.7 ± 170.2	5336.0 ± 229.5	2177.4 ± 280.2
			$E_0=7.90$ GeV $\theta=33.992°$		
1	2.50	2.07	217.0 ± 9.2	343.8 ± 9.4	129.9 ± 12.2
2	2.25	2.33	411.3 ± 14.3	590.4 ± 14.0	195.0 ± 18.3
3	2.00	2.56	642.5 ± 23.4	937.3 ± 24.1	322.4 ± 31.2
4	1.75	2.77	924.6 ± 32.1	1422.0 ± 43.5	537.2 ± 51.2
5	1.48	2.99	1301.6 ± 54.1	2180.1 ± 82.1	932.9 ± 95.4
			$E_0=10.00$ GeV $\theta=33.992°$		
1	3.00	1.94	35.1 ± 1.2	51.5 ± 1.5	13.1 ± 1.8
2	2.75	2.26	80.3 ± 2.5	120.8 ± 3.1	40.1 ± 3.9
3	2.50	2.53	173.9 ± 5.5	236.3 ± 6.3	67.2 ± 8.9
4	2.25	2.78	257.4 ± 10.6	384.3 ± 12.1	137.3 ± 16.4
5	2.00	3.01	409.4 ± 19.9	583.2 ± 18.4	190.4 ± 26.0
6	1.75	3.22	566.2 ± 27.4	857.7 ± 29.7	314.7 ± 39.1
7	1.50	3.42	820.3 ± 40.7	1260.5 ± 47.2	471.2 ± 60.6
			$E_0=12.50$ GeV $\theta=33.992°$		
1	3.25	2.09	12.8 ± 0.5	18.6 ± 0.6	3.8 ± 0.6
2	3.00	2.43	31.3 ± 1.0	44.8 ± 1.2	12.4 ± 1.5
3	2.75	2.73	64.7 ± 2.0	89.9 ± 2.4	26.0 ± 3.1
4	2.50	2.99	107.9 ± 3.7	164.0 ± 4.4	59.7 ± 6.0
5	2.25	3.24	180.5 ± 9.1	255.3 ± 8.3	81.8 ± 11.9
6	2.00	3.47	218.8 ± 11.3	382.2 ± 12.6	174.0 ± 16.4
7	1.75	3.68	372.2 ± 20.5	512.1 ± 21.4	153.5 ± 29.1
			$E_0=15.00$ GeV $\theta=33.992°$		
1	3.50	2.13	4.1 ± 0.2	6.4 ± 0.3	1.2 ± 0.3
2	3.25	2.50	11.5 ± 0.4	16.0 ± 0.5	3.6 ± 0.6
3	3.00	2.83	25.0 ± 0.9	36.7 ± 1.0	11.3 ± 1.3
4	2.75	3.13	47.1 ± 1.6	70.7 ± 1.9	24.4 ± 2.6
5	2.50	3.39	79.8 ± 2.8	114.9 ± 3.5	37.7 ± 4.6
6	2.25	3.64	105.6 ± 8.7	179.8 ± 8.6	79.1 ± 12.1
7	2.00	3.88	144.6 ± 12.8	239.9 ± 16.1	102.0 ± 20.6

of the proton (off the mass shell), $q=(0,0,q_3,\nu)$ is the four-momentum of the virtual photon, $\nu'=p\cdot q/M$, $(W')^2=(p+q)^2$, and $|f(\vec{p})|$ is the momentum distribution of a nucleon within the deuteron, taken to be the square of the Fourier transform of the nonrelativistic wave function. Aside from small off-mass-shell corrections (see Appendix C) the structure functions W_1^p and W_2^p used in Eq. (5.2) are identified with the measured on-shell structure functions at the same values of Q^2 and $W=W'$.

The smeared structure functions were combined as in Eq. (1.1) to yield a smeared fit proton cross section σ_{ps}^f at each experimental point. The ratio of the fit cross section before smearing σ_p^f to the smeared fit cross section, $S_p=\sigma_p^f/\sigma_{ps}^f$, was taken to be the proton smearing correction. The experimental proton cross sections $\sigma_p=(d^2\sigma/d\Omega dE')_p$ were then divided by S_p to yield the smeared proton cross sections $\sigma_{ps}=\sigma_p/S_p$.

The quantity S_p and the corresponding ratios for the individual structure functions $S_{p1}=W_1^p/W_{1s}^p$ and $S_{p2}=W_2^p/W_{2s}^p$ are nearly identical (see Appendix C) and insensitive to the value of R assumed as long

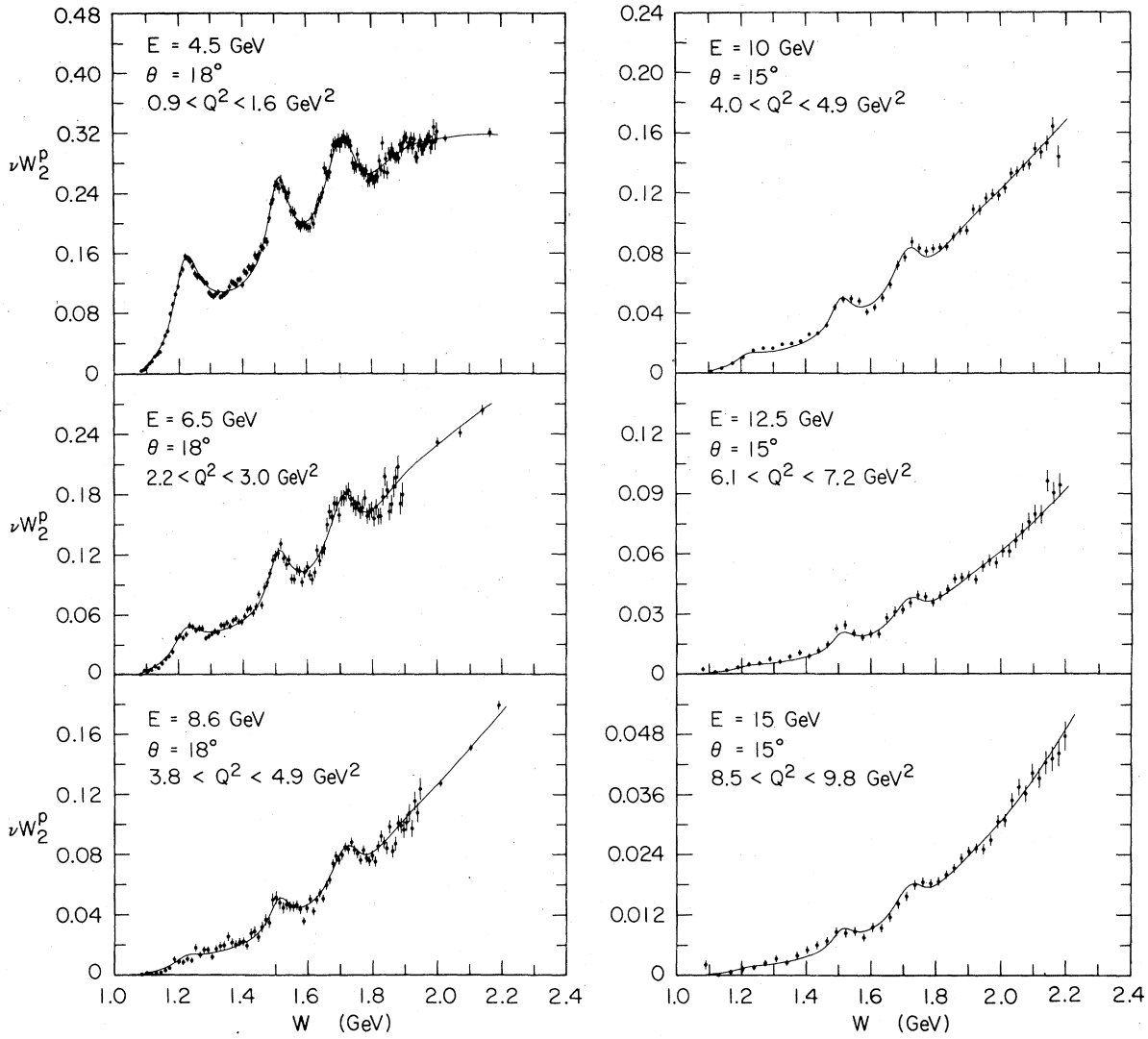

FIG. 17. The quantity νW_2^p measured at 18° and 15° in the resonance region.

as the parametrizations used provide good representations of the two structure functions. The quantity S_p varies sharply with x for $x \geq 0.6$, while for fixed values of x, S_p varies only weakly with Q^2. As an example of the x dependences in the 20 GeV, 19° measurements of experiment B, S_p was 1.028, 1.026, 1.010, 0.982, 0.880, and 0.710 for x of 0.413, 0.538, 0.640, 0.710, 0.810, and 0.883, respectively.

3. *Unsmeared neutron cross sections*

Subtraction of the smeared proton cross section from the deuteron cross section measured at the same kinematics yielded the smeared neutron cross section $\sigma_{ns}=\sigma_d-\sigma_{ps}$. The smeared-cross-section ratio σ_{ns}/σ_{ps} was then

$$\frac{\sigma_{ns}}{\sigma_{ps}}=S_p\frac{\sigma_d}{\sigma_p}-1. \tag{5.3}$$

This smeared ratio is equal to the true ratio σ_n/σ_p only if the neutron-smearing correction $S_n=\sigma_n/\sigma_{ns}$ is equal to S_p. We removed the smearing effects from the smeared neutron cross section and from the smeared ratio by calculating S_n and forming the unsmearing correction factor $U=S_n/S_p$. The unsmeared neutron cross sections were then calculated from

$$\sigma_n=\sigma_{ns}S_n=S_n\sigma_d-U\sigma_p, \tag{5.4}$$

and the unsmeared-cross-section ratio was

$$\frac{\sigma_n}{\sigma_p}=U\left(\frac{\sigma_{ns}}{\sigma_{ps}}\right)=U\left(S_p\frac{\sigma_d}{\sigma_p}-1\right). \tag{5.5}$$

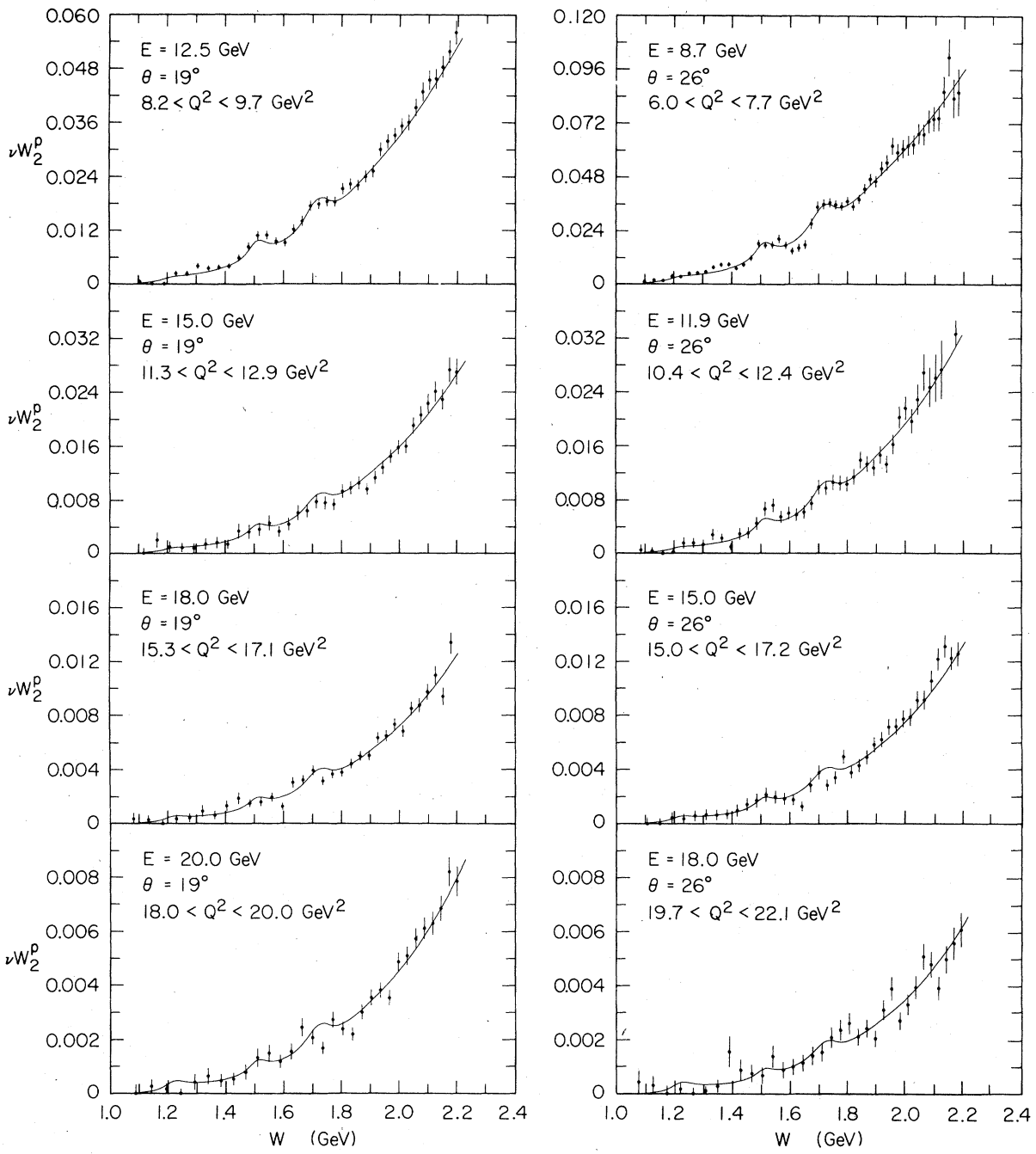

FIG. 18. The quantity νW_2^p measured at 19° and 26° in the resonance region.

Values of the unsmearing correction U and the neutron-smearing correction S_n were calculated by an unfolding procedure that employed a best-fit method. The structure function W_2^n was assumed to have the same general functional form as given for the proton in Eq. (5.1). The 24 parameters in $A(W,Q^2)$ and the parameters $C_1=a^2$ and $C_2=b^2$ in ω_w were assumed to be equal to the corresponding parameters for the proton. As $A(W,Q^2)$ was essentially unity in the deep-inelastic region, this assumption had little effect on our results. Under these assumptions, the structure function W_2^n was represented by a polynomial in $(1-1/\omega_w)$ with five undetermined coefficients. The individual terms in the polynomial were then smeared according to Eq. (5.2) and the coefficients C_3 through C_7 determined by fitting σ_{ns}^f calculated with this smeared structure function to the measured values of σ_{ns}.

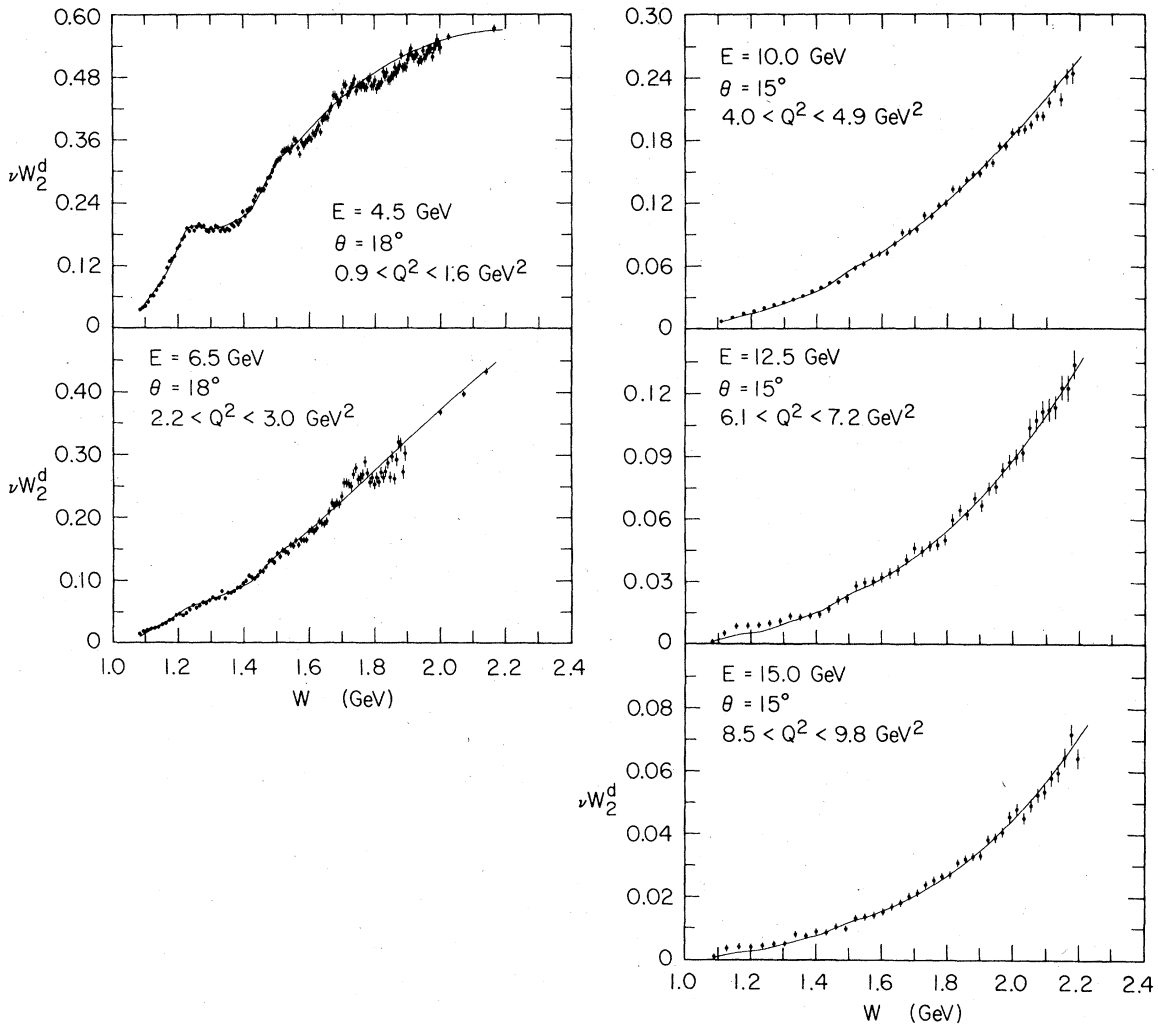

FIG. 19. The quantity νW_2^d measured at 18° and 15° in the resonance region.

The assumption $R_n = R_{ns} = 0.18$ was also used in these calculations to get σ_n^f and σ_{ns}^f from fits to the structure functions W_2^n and W_{2s}^n, but the results were insensitive to the particular form of R_n used. The constraints $\sigma_n^f/\sigma_p^f = 1.0$ at $1/\omega_w = 0$ and $\sigma_n^f/\sigma_p^f = 0.25$ at $\omega_w = 1$ were also imposed during the fitting procedure to ensure a representation of σ_n^f that could be extrapolated reliably. These constraints, however, had insignificant effects on the results. The extracted values of the cross-section ratios σ_n/σ_p and the associated uncertainties due to the various assumptions in the unsmearing fit are given in Tables IX and X. The correction factors $S_n = \sigma_n^f/\sigma_{ns}^f$ and $U = S_n/S_p$ were finally evaluated at the kinematic values of the e-p and e-d measurements using the values of the fit cross sections there. The unsmearing correction, U, was not far from unity, varying from 0.90 ± 0.02 at the smallest value of ω measured in the deep-inelastic region to 1.002 ± 0.003 at the largest measured value of ω.

This unsmearing procedure was reliable only in the deep-inelastic region where the structure functions vary smoothly with no resonant structure. The above method was not used in the resonance region because the structure functions are nonlinear in the undetermined resonance parameters and we could not solve for these parameters by smearing a linear set of functions. Only when the parametrization of the structure functions is linear in the undetermined coefficients can they be taken out of the smearing integrals, and the smearing process decoupled from the fitting procedure. We therefore quote neutron cross sections only for $W \geq 1.8$ GeV. The neutron cross sections are represented in Figs. 21–24 by the neutron structure function νW_2^n extracted from σ_n under the assumption $R_n = 0.18$. The neutron cross sections

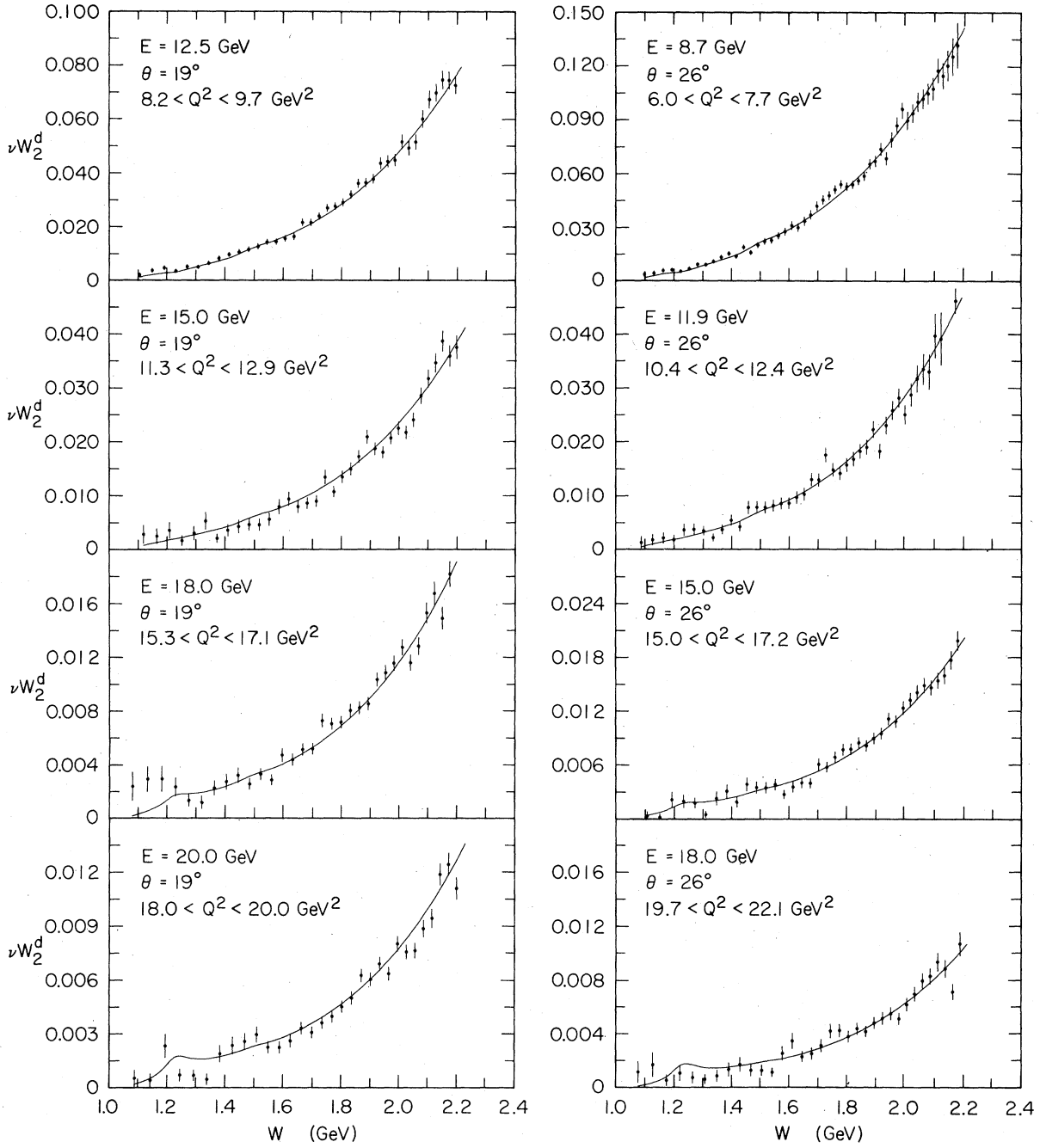

FIG. 20. The quantity νW_2^d measured at 19° and 26° in the resonance region.

themselves are presented in Table V, along with the proton and deuteron cross sections. As is the case for e-p and e-d cross sections, only combined cross sections are given in the tables. The combination of fine-mesh neutron cross sections used a procedure similar to that used for the proton and deuteron, as discussed in the next section. The cross-section ratios σ_n/σ_p were calculated directly from the fine-mesh deuteron and proton cross sections according to Eq. (5.5), and later combined according to the procedure described below.

The values of σ_n/σ_p as functions of x, and separately x', given in Tables IX and X, are shown in Fig. 25. The ratios were calculated at all measured kinematic points with $W \geq 1.8$ GeV and $Q^2 \geq 1.0$ GeV^2 (see Figs. 9–12 and 21–24) and averaged in small intervals of x or $x' = 1/\omega'$ ($\Delta x = 0.03$). In

TABLE VI. Random errors in cross sections.

Source of error	Percentage error in σ
A. Counting statistics	
a. Statistical errors in full target e-p and e-d cross sections	1.0–15.0
b. Statistical errors in empty replica target cross sections	0.1– 1.5
c. Statistical errors in positron cross sections	0.0– 0.3
d. Statistical errors in detector efficiencies	0.5– 1.5
B. Random fluctuations in apparatus	
a. Target density fluctuations	0.3
b. Charge monitor fluctuations	0.3
c. Fluctuations in incident beam energy	0.1– 0.8
d. Fluctuations in incident beam direction	0.1– 1.1
e. Errors in setting spectrometer angle	0.1– 0.5
f. Fluctuations in spectrometer magnet currents	0.0– 0.5
g. Fluctuations in detector efficiencies	0.5– 1.0

this averaging it is assumed that σ_n/σ_p approximately scales in x or x' (see Sec. VII). The data of the two experiments were combined separately in order to facilitate a comparison of the two sets of data. Individual values of σ_n and σ_p were normalized to the center of the bin in order to account for the small variation of σ_n/σ_p within a single bin. The σ_n/σ_p ratios are derived from σ_d/σ_p ratio measurements. The measured values for σ_d and σ_p are Poisson-distributed, but their ratio is not.[64] Studies[64] indicate that the quantity $\ln(1+\sigma_n/\sigma_p)$ is approximately Gaussian-distributed. Therefore, the averaging involved forming the weighted geometrical mean of $(1+\sigma_n/\sigma_p)$ for values in each x (or x') bin.

Only random errors (including counting statistics and also charge-monitor, target-density, and rate-dependent fluctuations) are shown in Figs. 21–24. Most systematic errors in the cross sections (solid angle, E and E' calibration, monitor calibration, etc.) cancel in the ratio σ_n/σ_p. Of those which do not cancel, we estimate systematic uncertainties arising from five sources. Uncertainties in the deuteron elastic and quasielastic radi-

TABLE VII. Systematic uncertainties in cross sections.

Source of uncertainty	Percentage uncertainty in σ
A. Overall normalization uncertainties	
a. Calibration of spectrometer acceptance	1.5
b. Calibration of charge monitors	0.5
c. Target-density normalization (hydrogen)	0.4[b]–0.7[a]
d. Target-density normalization (deuterium)	0.7[b]–0.9[a]
e. Target-length determination	0.4[b]–0.6[a]
f. Target impurities	0.1
g. Radiative correction uncertainty	3.0
B. Relative uncertainties	
a. Calibration of incident energy	0.1– 0.8
b. Calibration of E' versus E	0.1– 1.0
c. Acceptance averaging correction	0.0– 1.0
d. Variation with E' of spectrometer acceptance	0.0– 1.0
e. Electron detection efficiency	0.5– 1.0
f. Radiative correction uncertainty	1.0– 5.0

[a] Experiment A only.

[b] Experiment B only.

TABLE VIII. Global-fit parameters.

	Proton	Deuteron	Neutron
$C_1=a^2$	1.642±0.011	1.512±0.009	1.642±0.011[a]
$C_2=b^2$	0.376±0.005	0.351±0.004	0.376±0.005[a]
C_3	0.256	0.477	0.064
C_4	2.178	2.160	0.225
C_5	0.898	3.627	4.106
C_6	−6.716	−10.470	−7.079
C_7	3.756	4.927	3.055

[a] Held equal to value from proton fit.

ative tails arising from lack of knowledge of the neutron form factors at large Q^2 contribute a small error of about 0.002 to σ_n/σ_p. Uncertainties from the remaining four sources are listed separately in Table X. The first column gives the experimental error due to the ±1% uncertainty in the ratio of the number of nuclei in the deuterium target to that in the hydrogen target. The other three columns give errors due to uncertainties in the deuterium smearing corrections. The smearing and unsmearing corrections, which were calculated using the Hamada-Johnston[48] wave function, changed the uncorrected σ_n/σ_p ratios by multiplicative factors of 1.08, 1.07, 1.01, 0.91, 0.74, and 0.40 at x values of 0.31, 0.58, 0.67, 0.73, 0.79, and 0.88, respectively. The uncertainty quoted as "wave function" reflects the change in σ_n/σ_p when other reasonable deuteron wave functions[65] are used (see Appendix C). The uncertainty quoted as "off-shell" is taken to be the full effect of the off-mass-shell correction[63] in the smearing formalism (see Appendix C). This correction is such as to reduce σ_n/σ_p. The uncertainty quoted as "fit" reflects the change in σ_n/σ_p when different parametric functions are used to fit the neutron and proton structure functions which enter into the smearing and unsmearing integrals. The choice $R_n=R_p=0.18$ was used in the process of obtaining the parametric representations of the structure functions. The extracted σ_n/σ_p ratios were insensitive to the kinematic dependence of R. In addition, Glauber corrections are known to be small.[20] Other deuteron corrections cannot be estimated, but are expected to be small (see Appendix B).

TABLE IX. Ratios σ_n/σ_p from experiment A.

x, x'	$\sigma_n/\sigma_p(x)$	$\sigma_n/\sigma_p(x')$
0.085	0.973±0.183	0.968±0.183
0.115	0.892±0.050	0.886±0.049
0.145	0.786±0.035	0.839±0.030
0.175	0.853±0.027	0.804±0.025
0.205	0.774±0.025	0.754±0.025
0.235	0.726±0.025	0.733±0.025
0.265	0.751±0.026	0.704±0.022
0.295	0.687±0.022	0.678±0.022
0.325	0.671±0.023	0.642±0.022
0.355	0.646±0.023	0.638±0.023
0.385	0.633±0.023	0.623±0.025
0.415	0.632±0.023	0.635±0.024
0.445	0.620±0.023	0.561±0.026
0.475	0.570±0.028	0.547±0.028
0.505	0.550±0.028	0.552±0.026
0.535	0.563±0.028	0.534±0.027
0.565	0.535±0.028	0.498±0.036
0.595	0.494±0.033	0.494±0.035
0.625	0.499±0.032	0.451±0.033
0.655	0.455±0.033	0.433±0.036
0.685	0.423±0.052	0.403±0.055
0.715	0.417±0.036	0.319±0.066
0.745	0.318±0.066	
0.775		0.367±0.040[a]
0.805	0.370±0.040[a]	

[a] Data for two intervals combined.

The results of the previous 6° and 10° measurements[27,28] are also shown in Figs. 21–24. The data from the previous experiment were rebinned into small x and x' intervals ($\Delta x=0.03$) as in the two experiments reported here.

E. Combined cross sections

The fine-mesh cross sections shown in Figs. 9–16 were combined into the cross sections of Table V for use in the extraction of R and the structure functions. Only data with $W \geq 1.8$ GeV were used in this process, as data in the resonance region were not sufficiently smooth to permit this averaging. For the proton and deuteron data as many as eight adjacent fine-mesh cross sections $\sigma_i(E,\theta,E_i') \pm \delta\sigma_i(E,\theta,E_i')$ were combined to yield an average cross section $\sigma(E,\theta,E') \pm \delta\sigma(E,\theta,E')$ at average E' according to the formula

$$\sigma(E,\theta,E')=\sigma^f(E,\theta,E')r\,,$$

$$\delta\sigma(E,\theta,E')=\sigma^f(E,\theta,E')\delta r\,,$$

where

TABLE X. Ratios σ_n/σ_p from experiment B.

		Systematic uncertainties				
x, x'	Target	"Wave function"	"Off shell"	"Fit"	$\sigma_n/\sigma_p(x)$	$\sigma_n/\sigma_p(x')$
0.305	0.017	0.001	0.001	0.000	0.647 ± 0.058	0.631 ± 0.038
0.335	0.017	0.002	0.001	0.000	0.663 ± 0.033	0.656 ± 0.031
0.365	0.016	0.002	0.001	0.000	0.620 ± 0.031	0.618 ± 0.031
0.395	0.016	0.002	0.002	0.000	0.643 ± 0.032	0.596 ± 0.028
0.425	0.016	0.003	0.002	0.000	0.555 ± 0.026	0.547 ± 0.023
0.455	0.016	0.004	0.002	0.000	0.565 ± 0.022	0.585 ± 0.021
0.485	0.016	0.004	0.003	0.000	0.594 ± 0.023	0.541 ± 0.020
0.515	0.016	0.005	0.004	0.000	0.536 ± 0.022	0.513 ± 0.020
0.545	0.015	0.005	0.004	0.000	0.503 ± 0.020	0.514 ± 0.020
0.575	0.015	0.006	0.004	0.000	0.523 ± 0.020	0.464 ± 0.019
0.605	0.015	0.006	0.005	0.000	0.472 ± 0.019	0.454 ± 0.019
0.635	0.015	0.007	0.006	0.000	0.460 ± 0.019	0.450 ± 0.020
0.665	0.015	0.008	0.007	0.001	0.454 ± 0.021	0.398 ± 0.019
0.695	0.014	0.010	0.008	0.002	0.431 ± 0.020	0.398 ± 0.021
0.725	0.014	0.012	0.009	0.004	0.376 ± 0.020	0.362 ± 0.020
0.755	0.013	0.014	0.010	0.007	0.391 ± 0.021	0.335 ± 0.023
0.785	0.013	0.015	0.011	0.012	0.337 ± 0.020	0.310 ± 0.024
0.815	0.012	0.016	0.012	0.014	0.304 ± 0.024	0.270 ± 0.026
0.845	0.012	0.018	0.014	0.017	0.281 ± 0.025	0.291 ± 0.041 [a]
0.875	0.012	0.020	0.017	0.020	0.313 ± 0.034	

[a] Data for two intervals combined.

$$r=\frac{\sum_i \frac{r_i^2}{(\delta r_i)^2}}{\sum_i \frac{r_i}{(\delta r_i)^2}}, \qquad \delta r=\left(\frac{\sum_i \frac{r_i}{(\delta r_i)^2}}{r}\right)^{-1/2}, \tag{5.6}$$

using

$$r_i=\sigma_i(E,\theta,E_i')/\sigma^f(E,\theta,E_i')$$

and

$$\delta r_i=\delta\sigma_i(E,\theta,E_i')/\sigma^f(E,\theta,E_i').$$

Here σ^f is the appropriate cross section deter-

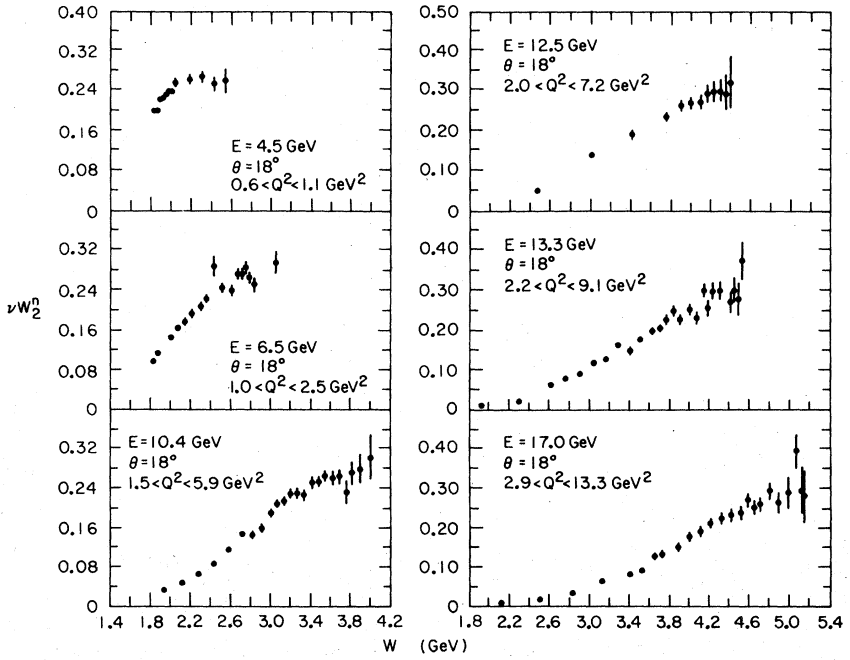

FIG. 21. The quantity νW_2^n extracted from inelastic e-p and e-d cross sections measured at 18° in experiment A.

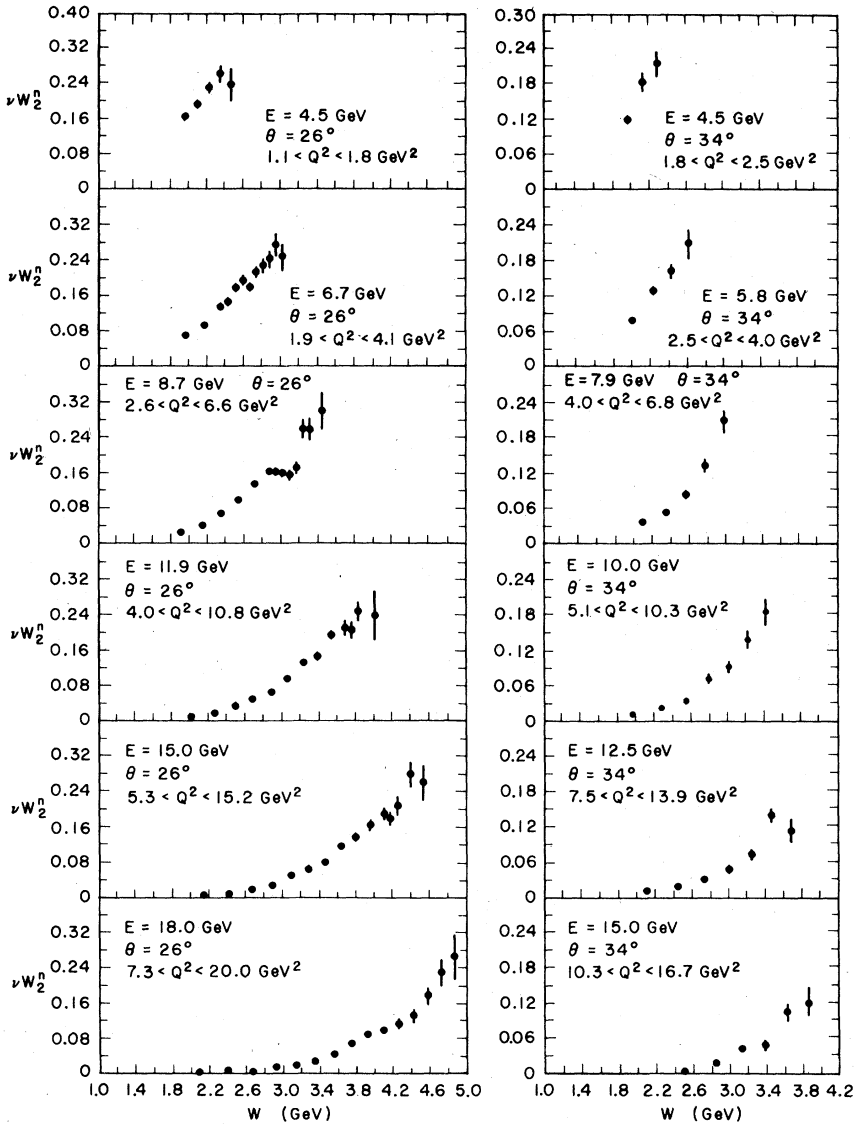

FIG. 22. The quantity νW_2^n extracted from inelastic e-p and e-d cross sections measured at 26° and 34° in experiment A.

mined using the global fit to νW_2 with the assumption $R_p = R_d = R_n = 0.18$ in Eq. (1.5).

Only the errors from counting statistics (see Sec. V B) were used in this averaging procedure. As the measurements of the cross sections were then Poisson-distributed, especially for low-statistics runs, the averaging procedure used [Eq. (5.6)] was the Poisson arithmetic average, according to the maximum-likelihood method. As mentioned in Sec. V B, the random error from equipment fluctuations was added in quadrature to this average error from counting statistics to yield the values of $\delta\sigma$ given in Table V. Where the cross section had already been averaged over the entire spectrometer acceptance before the radiative corrections, no combination had to be done, and only the random error from equipment fluctuations needed to be added in quadrature.

The combined neutron cross sections were obtained in a slightly different manner. Because σ_p, σ_d, and σ_{ps} are Poisson-distributed but $(\sigma_d - \sigma_{ps})$ is not, we could not average $(\sigma_d - \sigma_{ps})$ and then multiply by the average neutron smearing correction to get the average σ_n [see Eq. (5.4)]. Therefore, we formed the neutron smearing correction $s_n = \sigma_n/(\sigma_d - \sigma_{ps})$ for each fine-mesh data point, combined the products $\sigma_n\sigma_d$ and $\sigma_n\sigma_{ps}$ according to the prescription of Eqs. (5.6), and then took the difference of the two products to get the combined value of σ_n. The random errors from equipment

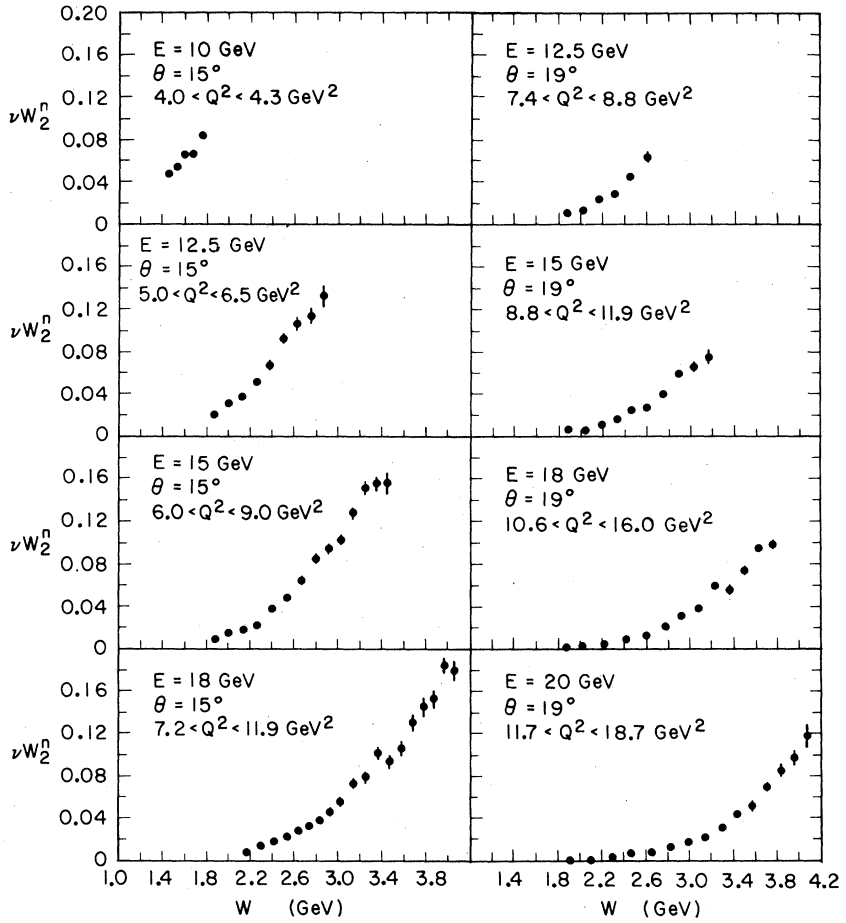

FIG. 23. The quantity νW_2^n extracted from inelastic e-p and e-d cross sections measured at 15° and 19° in experiment B.

fluctuations for both the proton and deuteron were added in quadrature to the average error from counting statistics to yield the values of $\delta\sigma_n(E,\theta,E')$ given in Table V.

F. Normalizations

Although the inelastic e-p and e-d cross sections were measured with much the same apparatus in the two experiments, the use of different targets and differences in the analysis procedures permitted a relative normalization difference between the two experiments. As such normalization differences could have seriously influenced the results for $R=\sigma_L/\sigma_T$, an estimate of them was deemed essential. Two methods were used to estimate the relative normalization factor N_{AB} of experiment B to experiment A, and both gave results consistent with $N_{AB}^p = N_{AB}^d = 1.010$.

In the first method, the inelastic e-p and e-d cross sections measured at 26° and 34° in experiment B were compared with those measured at nearly identical energies and angles in experiment A. At 26°, we had to compare fine-mesh cross sections from experiment B with cross sections that had been averaged over the entire spectrometer acceptance in experiment A. Up to eight adjacent fine-mesh cross sections were combined in the manner of Eq. (5.6) to yield a single cross section for values of E and E' close to those quoted in experiment A. The normalization factor of experiment B to experiment A was then taken, at each common kinematic point, to be

$$N_{AB}(E_A,E'_A,\theta_A)=\left(\frac{\sigma_A(E_A,E'_A,\theta_A)}{\sigma_B(E_B,E'_B,\theta_B)}\right)\left(\frac{\sigma^f(E_B,E'_B,\theta_B)}{\sigma^f(E_A,E'_A,\theta_B)}\right), \tag{5.7}$$

where σ^f is defined as before, and Eq. (5.7) applies for proton and deuteron cross sections. Use of σ^f in Eq. (5.7) eliminates the effects of slight differences in E, E', and θ settings between the two experiments. Averages of these normalization factors for each common value of incident

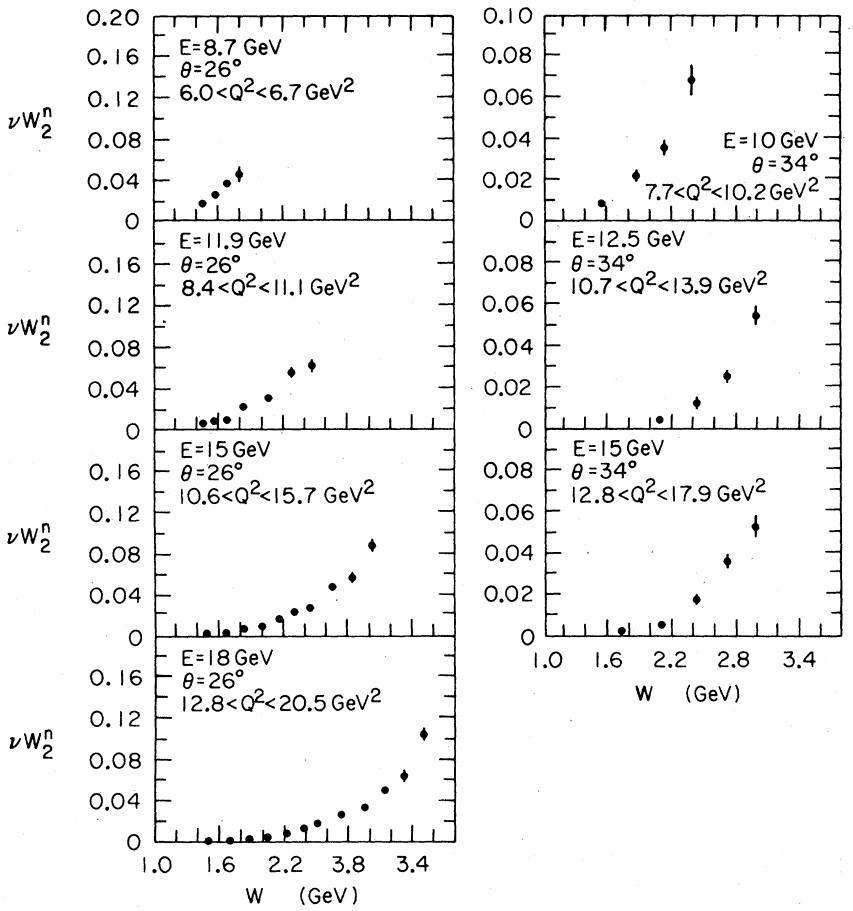

FIG. 24. The quantity νW_2^n extracted from inelastic e-p and e-d cross sections measured at 26° and 34° in experiment B.

energy and angle are presented in Table XI. Only cross sections for $W \geq 1.8$ GeV were used in calculating these factors. The normalization factors for the proton and deuteron were always within 1 standard deviation of their average. If we average over the entire sample of 26° and 34° data, we find $N_{AB}^p/N_{AB}^d = 1.001 \pm 0.013$; hereafter, we take $N_{AB}^p = N_{AB}^d$. The average 34° normalization factors for both the proton and deuteron were more than 1 standard deviation from the overall average.

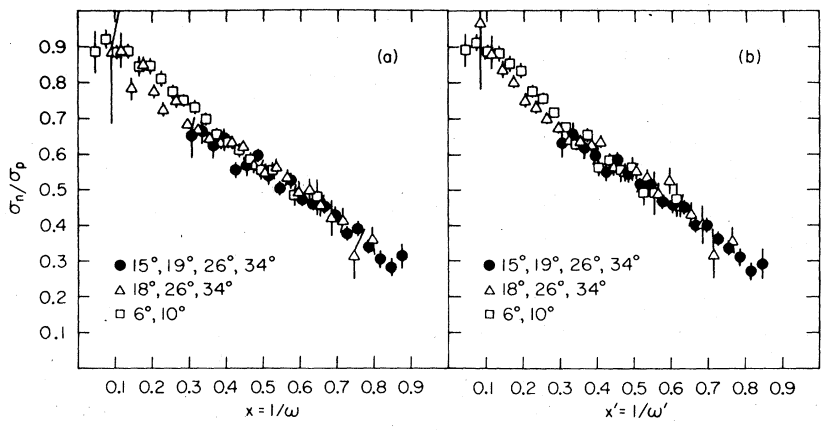

FIG. 25. (a) and (b). Values of σ_n/σ_p as determined from experiments A, B, and C as functions of x and x', respectively.

TABLE XI. Normalization factors.

θ (deg)	E (GeV)	N_{AB}^{p}	N_{AB}^{d}	$\bar{N}_{AB}$
26	8.7	0.985±0.031	1.028±0.024	1.012±0.019
26	11.9	1.043±0.022	1.027±0.017	1.033±0.013
26	15.0	1.009±0.020	1.010±0.014	1.010±0.011
26	18.0	1.015±0.021	1.005±0.015	1.008±0.012
26	all	1.017±0.012	1.015±0.008	1.015±0.006
34	10.0	0.960±0.041	0.953±0.026	0.955±0.022
34	12.5	0.965±0.045	0.994±0.029	0.985±0.024
34	15.0	1.011±0.043	1.028±0.030	1.022±0.025
34	all	0.979±0.025	0.989±0.016	0.984±0.014
all	all	1.010±0.010	1.010±0.007	1.010±0.006

These differences could be traced only to a few abnormally low cross sections in experiment A, however, and were not the general trend of the data. Separate normalization factors for the 26° and 34° data were not clearly warranted. Consequently, the relative normalization of experiment B to experiment A was taken to be the average of the 26° and 34° results, of $N_{AB}^{p}=1.010\pm0.010$ for the proton and $N_{AB}^{d}=1.010\pm0.007$ for the deuteron cross sections. These factors have been included in the cross sections of Table V.

A second estimate of N_{AB} was obtained from a comparison of elastic e-p cross sections measured in the two experiments. Differential elastic e-p cross sections from the two experiments were radiatively corrected according to the method of Tsai.[45] They were then divided by the dipole cross section $(d\sigma/d\Omega)_{dip}$, which was calculated by assuming form-factor scaling and the dipole form factor, $G_{Ep}=G_{Mp}/\mu_p=(1+Q^2/0.71)^{-2}$ in the Rosenbluth equation.[51] Ratios $r(Q^2)$ of measured to dipole differential cross sections are presented in Fig. 26 for the two experiments along with values of $r(Q^2)$ measured[27] in experiment C. A fourth-order-polynomial fit $r_A^f(Q^2)$ to the values of $r_A(Q^2)$ was compared to the three values of $r_B(Q^2)$ measured at 15° and one value measured at 19° in experiment B. The average of $N_{AB}^{p}=r_A^f(Q^2)/r_B(Q^2)$ over all four measurements was $N_{AB}^{p}=1.012\pm0.010$, while the average at 15° only was $N_{AB}^{p}=1.002\pm0.012$. Both numbers are consistent with the normalization factor $N_{AB}^{p}=N_{AB}^{d}=1.010$ derived from the 26° and 34° inelastic comparisons.

A similar method[26] was used to compute the normalization factor N_{AC} for experiment C. Only the elastic e-p cross sections measured at 10° were used, as the systematic uncertainty in the scattering angle[27,66] was too large at 6° to permit a reliable comparison. The polynomial fit $r_A^f(Q^2)$ was compared to seven values of $r_C(Q^2)$ shown in Fig. 26, resulting in an average normalization factor $N_{AC}^{p}=1.019\pm0.011$, where the quoted error is purely random. Systematic uncertainties in N_{AC}^{p} arise from uncertainties that affect the elastic cross sections in a manner different from the inelastic cross sections. These include uncertainties in E and θ (±0.8%), approximations in the radiative corrections (±0.7%), the assumption of form-factor scaling (±0.5%), and differences between the two experiments (±0.6%), in the method of binning the data to calculate $(d\sigma/d\Omega)_{elast}$. Added in quadrature to the random error, these effects led to the result $N_{AC}^{p}=1.019\pm0.017$. A determination of the normalization factor N_{AC}^{d} for the small angle inelastic e-d cross sections from quasielastic e-d cross sections was judged unfeasible due to uncertainties arising both from inelastic background subtractions and from corrections for deuteron binding effects. Therefore, the proton normalization factor was used for the deuteron cross sections of experiment C, $N_{AC}^{d}=1.019$

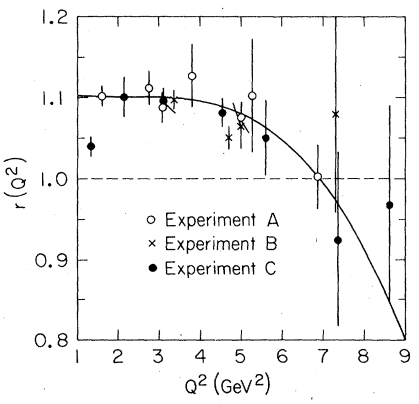

FIG. 26. Ratios, $r(Q^2)$, of the elastic e-p cross sections measured in experiments A, B, and C to elastic cross sections calculated using the dipole form factor in the Rosenbluth equation.

± 0.024, with an additional systematic uncertainty of ± 0.021 added in quadrature to the 0.011 error to account for uncertainties in target lengths and densities.

VI. SEPARATION OF R AND THE STRUCTURE FUNCTIONS

A. Interpolation of the cross sections

The separation of W_1 and W_2 (or equivalently σ_L and σ_T) at fixed (ν, Q^2) required differential cross sections $(d^2\sigma/d\Omega dE')(\nu, Q^2, \theta)$ for at least two values of θ. According to Eq. (1.2), σ_L is the slope and σ_T the $\epsilon = 0$ intercept of a linear fit to

$$\Sigma(\nu, Q^2, \theta) = \frac{1}{\Gamma}\frac{d^2\sigma}{d\Omega dE'} = \sigma_T(\nu, Q^2) + \epsilon(\nu, Q^2, \theta)\sigma_L(\nu, Q^2). \quad (6.1)$$

The structure functions and R are readily calculated from σ_L and σ_T according to Eqs. (1.3) and (1.4). There were, however, only a few kinematic points (ν, Q^2) at which the differential cross sections had been directly measured for two or more values of θ. Consequently, values of Σ and its error were obtained by interpolation of the cross sections measured at each angle to selected kinematic points (ν, Q^2) that fell within the overlaps of two or more of the data triangles measured in experiments A, B, and C. The kinematic region of $Q^2 - W^2$ space spanned by these overlaps of the measured data triangles is shown in Fig. 27. An array of 75 kinematic points (ν, Q^2), chosen to reflect the distribution of measured cross sections, was used in a systematic study of R and the structure functions. As shown in Fig. 27, these points lie at the intersections of contours of constant x $(0.1 \leq x \leq 0.8)$ and constant Q^2 $(1 \leq Q^2 \leq 16\ \mathrm{GeV}^2)$ with $W > 1.8$ GeV. A subset of this x Q^2 array, containing 51 (ν, Q^2) points with $0.2 \leq x \leq 0.8$ and $2 \leq Q^2 \leq 16\ \mathrm{GeV}^2$, was used in a parallel study wherein only cross sections from experiments A and B were used to extract R and the structure functions. Only the results from the full x-Q^2 array are reported here in detail. The results obtained for the restricted x-Q^2 array were consistent with those of the full x-Q^2 array. Previous separations of R and the structure functions using cross sections from experiments A and C have been reported earlier.[24,27] These previous results are consistent with the present results but are superseded by them.

The e-p and e-d cross sections from Table V were used to prepare interpolations at five different values of the scattering angle. As mentioned earlier, all cross sections from experiment B were multiplied by the normalization factor N_{AB} $= 1.010$. In this way, triangles of cross-section data were assembled at $\theta = 15°$, 18°, 19°, 26°, and 34°. In order to extend the accessible kinematic region to $x < 0.2$ and to extend the ranges of Q^2 and ϵ available for $x \geq 0.2$, cross sections measured at 6° and 10° in experiment C were also used in this analysis. These cross sections had been radiatively corrected[27] by the same method as had been used for experiments A and B. Prior to the interpolations, they were multiplied by $N_{AC} = 1.019$ to normalize them to those of experiment A.

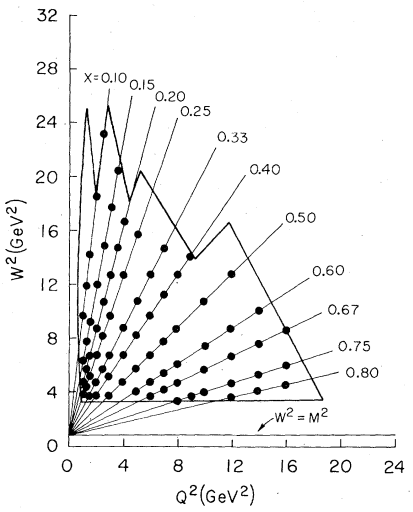

FIG. 27. The kinematic region of Q^2-W^2 space available for the separation of R and the structure functions. Separations were made at the 75 kinematic points (ν, Q^2) shown.

Values of $\Sigma(\nu, Q^2, \theta)$ and its random error were obtained by an interpolation scheme,[46] similar to the method used in the radiative corrections, that made no *a priori* assumptions about the behavior of R. Because this scheme effectively averaged 16 cross-section measurements for each (ν, Q^2, θ), the values of $\Sigma(\nu, Q^2, \theta)$ and its errors were correlated for neighboring kinematic points (ν, Q^2). In practice, these correlations were difficult to remove, and the distribution of kinematic points (ν, Q^2) was chosen to minimize them. As many as five values of Σ for five values of ϵ were available at a given kinematic point (ν, Q^2). In general, the errors of the separated quantities varied inversely as the range $\Delta\epsilon$ of the variable ϵ spanned by the cross sections for fixed (ν, Q^2). In the present separations, $\Delta\epsilon$ ranged from 0.16 to 0.57, while ϵ itself ranged from 0.24 to 0.98.

B. Separation of R_p and R_d

The quantities σ_L and σ_T were available as the parameters of a linear least-squares fit to $\Sigma(\nu, Q^2, \theta)$ versus $\epsilon(\nu, Q^2, \theta)$ at each kinematic point

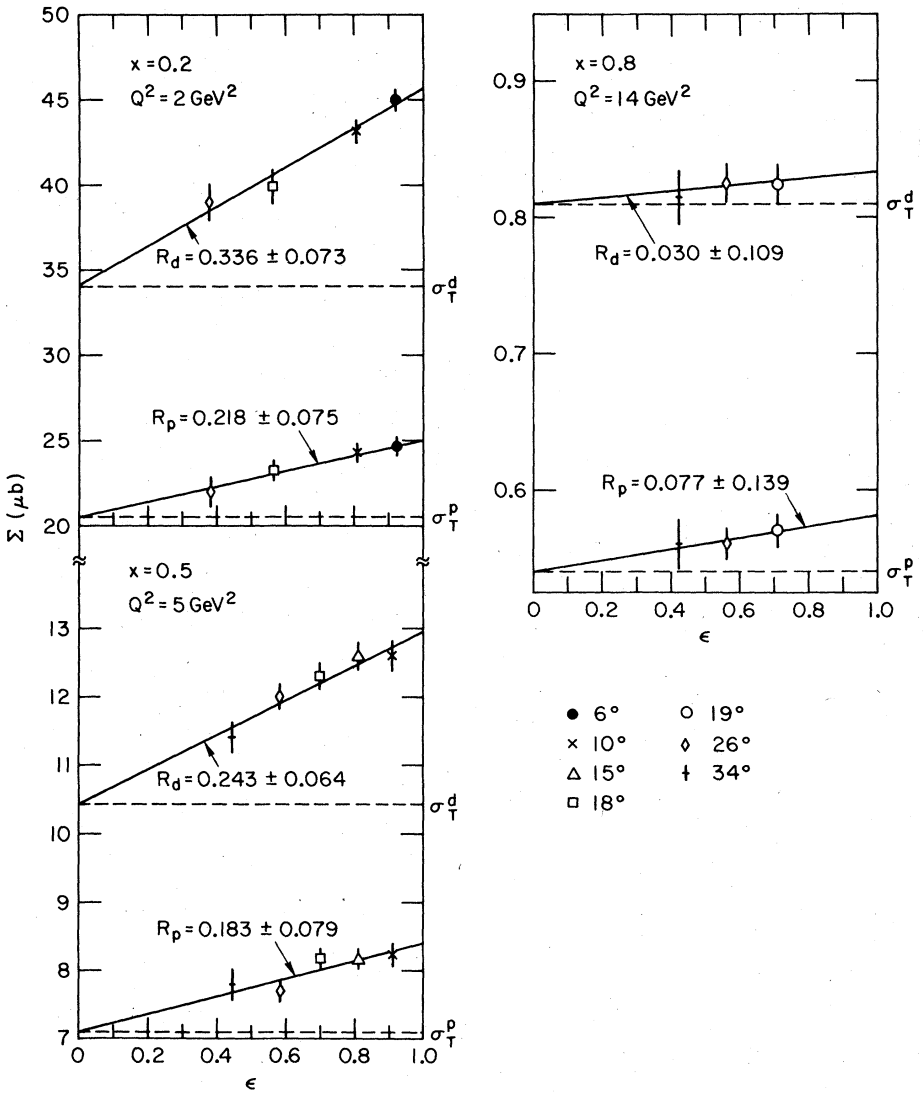

FIG. 28. Sample least-squares fits to $\Sigma(\nu, Q^2, \theta)$ vs $\epsilon(\nu, Q^2, \theta)$ in comparison with data. Σ, ϵ, and the fitting formulas are found in Eqs. (1.2) and (6.1). The quantities R and σ_T are available from the fitting parameters and from them, σ_L.

(ν, Q^2). Sample fits are shown in Fig. 28; in general, the confidence level for these fits was quite good. In only a few instances did χ^2 deviate from the number of degrees of freedom n_D of the fit by more than $(2n_D)^{1/2}$. Values of $R = \sigma_L/\sigma_T$ are presented for the proton in Table XII along with statistical errors and estimates of the systematic uncertainty ΔR_p. The five contributions to the total systematic uncertainty ΔR_p are listed separately in Table XII. The uncertainty ΔR_p^1 arising from the uncertainty of 0.010 in N_{AB}^p was estimated by repeating the separations using instead a normalization factor $N_{AB}^p = 1.020$. A similar procedure was used to estimate the uncertainty ΔR_p^2 arising from the uncertainty of 0.017 in N_{AC}^p. The uncertainty ΔR_p^3 arising from a possible E' dependence of the spectrometer acceptance was estimated[25] by using a redefined acceptance that varied by at most 1% from its nominal value (see Appendix A). The uncertainty ΔR_p^4 due to relative uncertainties in detector efficiencies was estimated by using redefined efficiencies that varied from their nominal values by at most 1% (at $E' = 2$ GeV). The radiative correction uncertainty ΔR_p^5 was estimated by varying all proton cross sections by an amount $\Delta\sigma$ determined according to Eq. (4.7). These five contributions were added in quadrature to obtain the total uncertainty ΔR_p reported in Table XII. The present values of R_p are consistent with those reported earlier[25,27]; much more accurate data

TABLE XII. Separated values of R_p, R_d, and δ with their random errors and systematic uncertainties. The quantities ΔR_p and ΔR_p^j are discussed in the text.

x	Q^2 (GeV^2)	W (GeV)	R_p	ΔR_p	ΔR_p^1	ΔR_p^2	ΔR_p^3	ΔR_p^4	ΔR_p^5	R_d	ΔR_d	δ	$\Delta\delta$
0.10	1.00	3.14	0.175 ± 0.132	0.081	0.0	0.036	0.026	0.023	0.063	0.120 ± 0.093	0.082	−0.022 ± 0.171	0.032
0.10	1.25	3.48	0.338 ± 0.155	0.092	0.0	0.036	0.025	0.022	0.078	0.181 ± 0.118	0.074	−0.135 ± 0.200	0.030
0.10	1.50	3.79	0.302 ± 0.127	0.092	0.0	0.034	0.025	0.020	0.079	0.289 ± 0.112	0.087	−0.012 ± 0.184	0.028
0.10	2.00	4.35	0.442 ± 0.199	0.103	0.0	0.028	0.019	0.018	0.096	0.273 ± 0.130	0.090	−0.123 ± 0.232	0.034
0.10	2.50	4.84	0.880 ± 0.844	0.229	0.0	0.115	0.074	0.070	0.171	0.297 ± 0.449	0.182	−0.456 ± 0.881	0.220
0.15	1.00	2.56	0.408 ± 0.159	0.138	0.0	0.094	0.054	0.055	0.064	0.479 ± 0.161	0.167	0.033 ± 0.237	0.090
0.15	1.25	2.82	0.205 ± 0.108	0.102	0.0	0.069	0.038	0.040	0.051	0.377 ± 0.102	0.148	0.201 ± 0.179	0.088
0.15	1.50	3.06	0.095 ± 0.089	0.077	0.0	0.049	0.027	0.028	0.045	0.359 ± 0.118	0.115	0.276 ± 0.203	0.070
0.15	2.00	3.49	0.321 ± 0.096	0.099	0.0	0.061	0.032	0.034	0.063	0.518 ± 0.129	0.131	0.123 ± 0.185	0.065
0.15	2.50	3.88	0.383 ± 0.175	0.130	0.0	0.088	0.042	0.049	0.070	0.471 ± 0.148	0.167	0.078 ± 0.231	0.091
0.15	3.00	4.23	0.332 ± 0.217	0.124	0.0	0.082	0.038	0.045	0.071	0.252 ± 0.142	0.137	−0.060 ± 0.245	0.075
0.15	3.50	4.55	0.174 ± 0.230	0.110	0.0	0.071	0.032	0.039	0.066	0.317 ± 0.173	0.145	0.149 ± 0.303	0.083
0.20	1.00	2.21	0.146 ± 0.107	0.128	0.0	0.097	0.048	0.055	0.039	0.180 ± 0.093	0.168	0.028 ± 0.146	0.098
0.20	1.25	2.42	0.246 ± 0.118	0.136	0.0	0.104	0.048	0.057	0.045	0.267 ± 0.105	0.171	−0.084 ± 0.147	0.086
0.20	1.50	2.62	0.457 ± 0.140	0.151	0.0	0.115	0.049	0.062	0.058	0.483 ± 0.119	0.191	0.009 ± 0.189	0.109
0.20	2.00	2.98	0.218 ± 0.075	0.085	0.0	0.057	0.031	0.033	0.045	0.336 ± 0.073	0.106	0.074 ± 0.113	0.053
0.20	2.50	3.30	0.071 ± 0.072	0.075	0.0	0.054	0.021	0.028	0.037	0.250 ± 0.090	0.109	0.148 ± 0.143	0.062
0.20	3.00	3.59	0.171 ± 0.111	0.098	0.0	0.073	0.028	0.038	0.043	0.277 ± 0.096	0.134	0.102 ± 0.158	0.079
0.20	3.50	3.86	0.261 ± 0.158	0.109	0.0	0.083	0.027	0.042	0.048	0.465 ± 0.151	0.164	0.202 ± 0.244	0.103
0.20	4.00	4.11	0.127 ± 0.122	0.093	0.0	0.071	0.022	0.035	0.043	0.439 ± 0.129	0.154	0.325 ± 0.209	0.102
0.25	1.00	1.97	0.439 ± 0.186	0.255	0.0	0.206	0.086	0.109	0.055	0.426 ± 0.152	0.325	−0.001 ± 0.249	0.194
0.25	1.25	2.15	0.106 ± 0.113	0.135	0.0	0.109	0.044	0.058	0.033	0.184 ± 0.101	0.197	0.063 ± 0.160	0.116
0.25	1.50	2.32	0.307 ± 0.125	0.155	0.0	0.125	0.047	0.065	0.045	0.378 ± 0.109	0.219	0.048 ± 0.170	0.129
0.25	2.00	2.62	0.233 ± 0.083	0.096	0.0	0.072	0.033	0.039	0.038	0.346 ± 0.082	0.129	0.140 ± 0.134	0.078
0.25	2.50	2.89	0.196 ± 0.117	0.103	0.0	0.083	0.025	0.041	0.037	0.316 ± 0.135	0.146	−0.041 ± 0.176	0.070
0.25	3.00	3.14	0.179 ± 0.090	0.089	0.0	0.067	0.030	0.036	0.036	0.242 ± 0.076	0.106	−0.027 ± 0.118	0.056
0.25	4.00	3.59	0.095 ± 0.113	0.074	0.0	0.055	0.023	0.029	0.033	0.174 ± 0.094	0.102	0.097 ± 0.162	0.063
0.25	5.00	3.98	−0.004 ± 0.085	0.066	0.0	0.049	0.018	0.025	0.031	0.096 ± 0.071	0.093	0.130 ± 0.127	0.058
0.33	1.50	1.97	0.475 ± 0.218	0.284	0.0	0.244	0.071	0.117	0.048	0.489 ± 0.170	0.394	−0.006 ± 0.281	0.233
0.33	2.00	2.21	0.121 ± 0.073	0.095	0.0	0.075	0.034	0.040	0.026	0.173 ± 0.062	0.129	0.034 ± 0.098	0.075
0.33	2.50	2.43	0.079 ± 0.102	0.109	0.0	0.095	0.021	0.043	0.026	0.029 ± 0.103	0.128	−0.149 ± 0.136	0.072
0.33	3.00	2.62	0.177 ± 0.058	0.071	0.0	0.051	0.028	0.029	0.027	0.242 ± 0.049	0.090	0.061 ± 0.079	0.049
0.33	4.00	2.98	0.042 ± 0.059	0.060	0.0	0.044	0.023	0.025	0.022	0.217 ± 0.062	0.088	0.188 ± 0.098	0.053
0.33	5.00	3.30	0.041 ± 0.086	0.066	0.0	0.053	0.018	0.026	0.022	0.307 ± 0.092	0.112	0.282 ± 0.156	0.077
0.33	6.00	3.59	0.687 ± 0.346	0.073	0.0	0.0	0.056	0.026	0.038	0.069 ± 0.153	0.045	−0.600 ± 0.263	0.134
0.33	7.00	3.86	0.365 ± 0.339	0.058	0.0	0.0	0.045	0.022	0.031	0.062 ± 0.188	0.046	−0.309 ± 0.316	0.076

TABLE XII. (*Continued*)

x	Q^2 (GeV^2)	W (GeV)	R_p	ΔR_p	ΔR_p^1	ΔR_p^2	ΔR_p^3	ΔR_p^4	ΔR_p^5	R_d	ΔR_d	δ	$\Delta\delta$
0.40	2.00	1.97	0.140±0.085	0.109	0.0	0.088	0.038	0.047	0.023	0.238±0.077	0.156	0.093±0.125	0.096
0.40	3.00	2.32	0.078±0.054	0.064	0.0	0.048	0.027	0.028	0.019	0.137±0.044	0.083	0.055±0.073	0.047
0.40	4.00	2.62	0.193±0.071	0.071	0.0	0.053	0.029	0.031	0.021	0.195±0.054	0.087	0.000±0.088	0.049
0.40	5.00	2.89	0.106±0.064	0.054	0.004	0.037	0.024	0.024	0.019	0.169±0.055	0.055	0.060±0.090	0.035
0.40	6.00	3.14	0.011±0.058	0.047	0.005	0.034	0.018	0.021	0.017	0.143±0.049	0.066	0.140±0.085	0.040
0.40	7.00	3.37	0.040±0.091	0.048	0.032	0.0	0.024	0.020	0.016	0.166±0.075	0.047	0.131±0.127	0.045
0.40	8.00	3.59	0.166±0.104	0.052	0.033	0.0	0.028	0.022	0.019	0.151±0.074	0.046	0.015±0.127	0.041
0.40	9.00	3.79	0.178±0.208	0.046	0.0	0.0	0.036	0.020	0.019	0.110±0.147	0.044	−0.065±0.248	0.011
0.50	3.00	1.97	0.074±0.060	0.073	0.0	0.057	0.029	0.032	0.014	0.125±0.050	0.094	0.042±0.083	0.057
0.50	4.00	2.21	0.190±0.074	0.067	0.0	0.048	0.032	0.031	0.015	0.181±0.056	0.083	0.002±0.096	0.047
0.50	5.00	2.42	0.183±0.079	0.056	0.006	0.037	0.027	0.028	0.015	0.243±0.064	0.068	0.061±0.106	0.041
0.50	6.00	2.62	0.085±0.062	0.047	0.001	0.032	0.022	0.024	0.012	0.209±0.055	0.066	0.125±0.091	0.040
0.50	7.00	2.81	0.086±0.067	0.048	0.018	0.031	0.019	0.023	0.013	0.176±0.055	0.064	0.094±0.092	0.039
0.50	8.00	2.98	0.040±0.087	0.032	0.007	0.0	0.019	0.021	0.012	0.243±0.081	0.040	0.201±0.134	0.048
0.50	10.00	3.30	0.217±0.130	0.052	0.032	0.0	0.032	0.022	0.013	0.138±0.086	0.044	−0.013±0.158	0.023
0.50	12.00	3.59	0.184±0.150	0.040	0.0	0.0	0.031	0.023	0.013	0.170±0.119	0.040	0.004±0.194	0.033
0.60	5.00	2.05	0.231±0.100	0.058	0.026	0.026	0.031	0.031	0.011	0.058±0.061	0.046	−0.176±0.104	0.042
0.60	6.00	2.21	0.240±0.083	0.057	0.002	0.039	0.026	0.030	0.012	0.108±0.055	0.052	−0.134±0.094	0.036
0.60	7.00	2.36	0.091±0.061	0.050	0.005	0.037	0.019	0.025	0.010	0.110±0.049	0.061	0.020±0.082	0.036
0.60	8.00	2.49	0.149±0.088	0.033	0.006	0.0	0.020	0.024	0.009	0.163±0.072	0.035	0.032±0.114	0.044
0.60	10.00	2.75	0.109±0.081	0.028	0.003	0.0	0.010	0.025	0.008	0.119±0.070	0.029	0.017±0.107	0.046
0.60	12.00	2.98	0.001±0.120	0.030	0.0	0.0	0.022	0.019	0.007	0.120±0.109	0.034	0.127±0.171	0.052
0.60	14.00	3.20	0.034±0.116	0.030	0.0	0.0	0.020	0.021	0.007	0.053±0.099	0.029	0.024±0.155	0.038
0.67	6.00	1.97	0.238±0.130	0.047	0.001	0.019	0.023	0.034	0.009	0.063±0.082	0.037	−0.148±0.146	0.054
0.67	7.00	2.09	0.182±0.081	0.052	0.001	0.037	0.020	0.030	0.008	0.084±0.058	0.047	−0.076±0.101	0.035
0.67	8.00	2.21	0.244±0.093	0.048	0.031	0.0	0.020	0.029	0.007	0.035±0.058	0.032	−0.209±0.097	0.045
0.67	10.00	2.42	0.107±0.088	0.030	0.006	0.0	0.011	0.026	0.008	0.082±0.071	0.028	−0.030±0.110	0.040
0.67	12.00	2.62	−0.016±0.091	0.035	0.023	0.0	0.016	0.020	0.005	0.073±0.080	0.035	0.087±0.126	0.014
0.67	14.00	2.81	0.058±0.111	0.029	0.0	0.0	0.017	0.022	0.005	0.176±0.103	0.032	0.114±0.158	0.051
0.67	16.00	2.98	0.351±0.284	0.036	0.0	0.0	0.002	0.036	0.007	−0.005±0.168	0.026	−0.345±0.263	0.085
0.75	8.00	1.88	0.215±0.187	0.043	0.002	0.0	0.008	0.042	0.006	0.378±0.198	0.053	0.211±0.338	0.135
0.75	9.00	1.97	0.165±0.108	0.033	0.002	0.0	0.003	0.033	0.005	0.122±0.086	0.031	−0.021±0.147	0.057
0.75	10.00	2.05	0.189±0.108	0.033	0.007	0.0	0.015	0.028	0.005	0.071±0.077	0.030	−0.112±0.130	0.044
0.75	12.00	2.21	0.108±0.103	0.035	0.019	0.0	0.015	0.024	0.004	0.098±0.080	0.033	0.007±0.133	0.016
0.75	14.00	2.36	0.100±0.115	0.028	0.0	0.0	0.016	0.023	0.004	0.153±0.101	0.030	0.052±0.155	0.054
0.75	16.00	2.49	0.132±0.114	0.028	0.0	0.0	0.010	0.026	0.004	0.267±0.107	0.032	0.128±0.166	0.057
0.80	12.00	1.97	0.022±0.138	0.026	0.008	0.0	0.009	0.023	0.003	0.152±0.127	0.030	0.140±0.210	0.035
0.80	14.00	2.09	0.077±0.139	0.027	0.0	0.0	0.009	0.025	0.003	0.030±0.109	0.025	−0.064±0.166	0.042
0.80	16.00	2.21	0.142±0.124	0.028	0.0	0.0	0.005	0.028	0.003	0.165±0.104	0.028	−0.014±0.160	0.043

are presented for $\omega \lesssim 2$ than were available before.

Values of R_d are also listed in Table XII; they were extracted from the interpolated deuteron cross sections using the same procedure as used for the proton. The five contributions to the systematic uncertainty in R_d were calculated in the same manner as used for R_p, except that uncertainties of 0.007 and 0.024 in the deuteron normalization factors N^d_{AB} and N^d_{AC} were used. They were added in quadrature to obtain the total uncertainty ΔR_d listed.

The weighted averages of R_p and R_d over the full $x-Q^2$ array provide a rough comparison of these quantities. We find $\bar{R}_p = 0.138 \pm 0.011$, with a total systematic uncertainty $\Delta\bar{R}_p = 0.056$, and $\bar{R}_d = 0.175 \pm 0.009$, with a total systematic uncertainty $\Delta\bar{R}_d = 0.060$. Within the normalization uncertainty of experiment C alone, $\bar{R}_d$ is consistent with being equal to $\bar{R}_p$. When the weighted averages are taken over the restricted x-Q^2 array only, using data from experiments A and B, we find $\bar{R}_p = 0.136 \pm 0.017$ and $\bar{R}_d = 0.137 \pm 0.013$.

A more detailed and accurate comparison of R_p, R_d and R_n was achieved by extracting the quantity $\delta = R_d - R_p$ from the ratio of differential cross sections σ_d/σ_p in a method that exploited the expected small systematic uncertainty in this ratio. From Eq. (1.2) we get[26]

$$\frac{\sigma_d}{\sigma_p} = \frac{\sigma_{Td} + \epsilon\sigma_{Ld}}{\sigma_{Tp} + \epsilon\sigma_{Lp}} = T\frac{1+\epsilon R_d}{1+\epsilon R_p} = T(1+\epsilon'\delta)\,, \tag{6.2}$$

where $T = \sigma_{Td}/\sigma_{Tp}$ and $\epsilon' = \epsilon/(1+\epsilon R_p)$. The physical meaning of Eq. (6.2) is clear: A difference between R_d and R_p results in a slope in σ_d/σ_p plotted versus ϵ' (or, essentially versus ϵ). The connection between R_n and δ is achieved through an expression[20] that exploits the observation that the smearing correction is empirically the same for W_1 and W_2 (see Appendix C)

$$R_d = R_p\left(\frac{1}{1+Z}\right) + R_n\left(\frac{Z}{1+Z}\right), \tag{6.3a}$$

$$R_n = R_d + \delta/Z\,, \tag{6.3b}$$

where $Z = W^n_{1s}/W^p_{1s}$ is the ratio of smeared W^n_1 to smeared W^p_1. In practice, Eq. (6.3b) is not very useful if $\delta \neq 0$, for Z is also an unknown. But if $\delta = 0$, which we find to be consistent with our overall results, then $R_n = R_d$ and $R_n = R_p$. In this manner we can compare R_p, R_d, and R_n, independent of the assumptions about R_n needed to calculate σ_n from σ_d in the impulse approximation.

At each of the 75 kinematic points (ν, Q^2), the quantity δ was extracted as one of the two parameters of a least-squares fit of the form of Eq. (6.2) to interpolated values of σ_d/σ_p versus ϵ'. The interpolations program was almost identical to the one used to interpolate Σ. At each (ν, Q^2) point, the value of R_p in $\epsilon' = \epsilon/(1+\epsilon R_p)$ was taken to be that listed in Table XII. Values of δ and its random error from these fits are reproduced in Table XII along with estimates of the total systematic uncertainty $\Delta\delta$. One contribution to this uncertainty arose from the ambiguity in the appropriate choice of R_p used to calculate ϵ' and ranged from 0.0 to 0.02 in δ. Another uncertainty arose from the uncertainty of 1.3% in the ratio of deuteron to proton normalization factors N^d_{AB}/N^p_{AB} and ranged from 0.01 to 0.12 in δ. A third uncertainty in δ arose from taking the normalization factor N^d_{AC} to be equal to N^p_{AC}, which had been calculated by a comparison of elastic e-p cross sections; this uncertainty ranged from 0.02 to 0.23 in δ. The quadratic sum of these three uncertainties is presented in Table XII as $\Delta\delta$ and is, in general, much smaller than the random error in δ.

The result $\delta = 0$ is consistent with all the data listed in Table XII. Values of δ are typically less than 1 standard deviation, and in only two instances more than 2 standard deviations, different from zero. Weighted averages of δ for each of the 11 values of x are presented in Fig. 29 along with their random errors. Systematic uncertainties in these averages range from 0.03 to 0.08 and are largest for the range $0.15 \leq x \leq 0.33$. No statistically significant deviation from zero can be seen anywhere in these data. When the normalization factor N^d_{AC} was taken to be unity instead of 1.019, the average values of δ in the range $0.10 \leq x \leq 0.50$ were all within 1 standard deviation of zero. The average of δ over the full $x-Q^2$ array, $\bar{\delta} = 0.031 \pm 0.015$, has a total systematic uncertainty of $\Delta\delta = 0.036$ and is consistent with zero. If δ calculated using only cross sections from experiments A and B, its average over the restricted $x-Q^2$ array is $\delta = -0.001 \pm 0.022$. The only suggestion of some nonzero behavior of δ occurs for $W \lesssim 2.5$ GeV and $x \geq 0.60$, where R_d is consistently smaller than R_p. Present estimates of the off-mass-shell corrections to the deuteron smearing

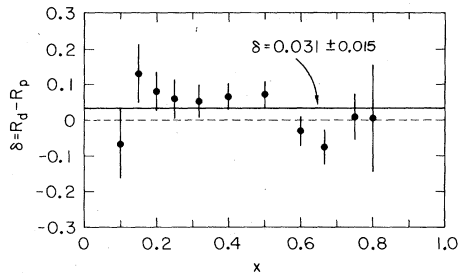

FIG. 29. Average values of the quantity $\delta = R_d - R_p$ for each of the 11 values of x studied. Errors shown are purely random. The systematic error in $\bar{\delta}$ is 0.036.

ratios (see Reference 63 and Appendix C) are much smaller than the errors in R_d and cannot explain this effect. Except for this possible difference at low W, which could be influenced by tails from the nucleon resonances, we conclude that $R_d = R_p$, and hence that $R_n = R_p$, over the full range of the x-Q^2 array.

C. Kinematic variation of R_p and R_d

The behavior of R in the Bjorken limit is an important test of constituent models[6,21] of nucleon structure. In conventional field theories with only spin-$\frac{1}{2}$ charged constituents, R should vanish as $1/Q^2$ in the Bjorken limit.[21,22] More recently, field theories with asymptotic freedom[18] predict that R should vanish as $1/\ln Q^2$. In both cases, the presence of charged spin-0 constituents would be reflected in a nonvanishing contribution to R, i.e., R itself should scale.[23] The kinematic variation of R was, however, difficult to ascertain because of large random errors and systematic uncertainties in the present data. Consequently, two approaches to the study of the kinematic variation of R_p and R_d were used. In the first approach, universal fits were made to the entire body of data for R_p or R_d. In the second approach, individual fits to R_p or R_d were attempted at each of the 11 values of x at which these quantities were available. The interpretation of these fits is discussed in this section.

The results of four least-squares fits to all the data for R_p and R_d are presented in Table XIII. Included in the table are the best-fit parameters, their random errors and systematic uncertainties, and the χ^2 sum for each fit. Systematic uncertainties in the fit parameters arising from the five uncertainties in R_p or R_d were added in quadrature to produce the numbers listed under Δ in Table XIII. When only the R_p or R_d data for $W \geq 2.0$ GeV were used in these fits, the best-fit parameters shifted by less than 1 standard deviation.

The χ^2 for the universal fits to R_p was consistently smaller than the χ^2 for the corresponding fits to the R_d data. This fact probably reflects the fact that the random errors for R_d are smaller, relative to the systematic uncertainties, than those for R_p. In addition to the fits listed in Table XIII, fits of the forms $R = cQ^2$, $R = cQ^2(1-x)^2$, $R = Q^2/\nu^2$ were attempted. These functions provided very poor fits to the data, and are consequently not listed. Except at low $x \lesssim 0.2$, the data for R_p and R_d are inconsistent with a linear rise in Q^2, as required by simple vector-dominance models[13] of inelastic e-N scattering. A constant value still fits the R_p data quite well. The best-fit value $R_p = 0.14 \pm 0.07$ is consistent with the values $R_p = 0.18 \pm 0.10$ and $R_p = 0.16 \pm 0.10$ reported in earlier determinations[7,24] of this quantity over different kinematic ranges. On the basis of χ^2, a constant fit to the R_d data fares rather poorly, but this may reflect only the influence of systematic uncertainties, particularly in the deuteron normalization factor N_{AC}^d. The strict Callan-Gross relation[21] $R = Q^2/\nu^2$ fits both proton and deuteron data very poorly, and the form $R = cQ^2/\nu^2$ is only marginally better. However, a more general spin-$\frac{1}{2}$ prediction[22,23] $R = g(x)Q^2/\nu^2$ provides an excellent representation of the R_p data and a fair representation of the R_d data. Such a deviation from simple Q^2/ν^2 behavior at large ω has been predicted from Regge arguments[22] in the framework of light-cone algebras[21] and deduced[67] from ρ electroproduction data.[68] The fitting function[69] $R = cQ^2/(Q^2+d^2)^2$ ensures that $R \to 0$ as $Q^2 \to 0$, as required by gauge invariance, and vanishes as $1/Q^2$ is the Bjorken limit. It provides excellent fits to both the proton and deuteron data. A similar[69] fit, $R = cQ^2/(Q^2+d^2)$, that vanishes as $Q^2 \to 0$ and approaches a constant in the Bjorken limit, fits the R_p and R_d data with equally good χ^2. However, the best-fit values of d^2 are negative producing singularities

TABLE XIII. Universal fits to R_p and R_d. The best-fit parameters for each fit function are listed along with the total χ^2 of the fits to 75 data points. The quantity Δ represents the systematic uncertainty in each parameter.

Fit function	Proton Best-fit parameter	Δ	χ^2	Deuteron Best-fit parameter	Δ	χ^2
$R = c$	$c = 0.138 \pm 0.011$	0.056	71	$c = 0.175 \pm 0.009$	0.060	107
$R = \frac{Q^2}{\nu^2}\left(c + \frac{d}{x^2}\right)$	$c = 0.392 \pm 0.100$ $d = 0.073 \pm 0.012$	0.152 0.041	63	$c = 0.334 \pm 0.080$ $d = 0.108 \pm 0.010$	0.135 0.056	116
$R = \frac{cQ^2}{(Q^2+d^2)^2}$	$c = 0.861 \pm 0.202$[a] $d^2 = 0.988 \pm 0.388$[a]	0.363[a] 0.229[a]	62	$c = 1.281 \pm 0.167$[a] $d^2 = 1.158 \pm 0.241$[a]	0.399[a] 0.289[a]	73
$R = \frac{c}{1 + d\ln(Q^2/M^2)}$	$c = 0.294 \pm 0.063$ $d = 0.808 \pm 0.358$	0.165 0.237	58	$c = 0.355 \pm 0.045$ $d = 0.665 \pm 0.184$	0.206 0.261	77

[a] In units of GeV^2.

in R_p and R_d at $Q^2=-d^2$, and the fit is not included in Table XIII. The final fit is derived from $R=\alpha/\ln(Q^2/\beta^2)$, with $d=(\ln M^2/\beta^2)^{-1}$ and $c=\alpha^2 d$. While this fit is necessarily singular at $Q^2=\beta^2$, or at $Q^2=0.255$ GeV^2 for the proton and $Q^2=0.196$ GeV^2 for the deuteron, the model is intended to apply in the limit of high Q^2. This function fits the data equally as well as $R=cQ^2/(Q^2+d^2)^2$, and the present data cannot distinguish between an asymptotic $1/Q^2$ and $1/\ln Q^2$ behavior of R in the Bjorken limit. Although these two functional forms fit the data better than the constant fit, we cannot rule out a nonvanishing contribution to R, at least not on the basis of the universal fits to all the present data. For a sample of data restricted to $x \geq 0.25$, the constant, the asymptotic $1/Q^2$ and the $1/\ln Q^2$ functions all fit R_p equally well, while the constant fit is still a poor representation of the data for R_d.

The x-Q^2 array permitted a study of the Q^2 dependence of R_p and R_d for fixed values of x in the range $0.1 \leq x \leq 0.8$. This approach allowed unbiased tests of functional forms that could not be fitted satisfactorily to the overall x dependence of R, and consequently allowed more stringent tests of the behavior of R_p and R_d in the Bjorken limit for various regions of x. The data for R_p and R_d are plotted versus Q^2 in Fig. 30 for the 11 fixed values of x available. The three curves plotted at each x in these figures represent best fits of the functional forms $R=c(x)$, $R=\alpha^2(x)/\ln(Q^2/\beta^2)$, and $R=c(x)Q^2/(Q^2+d^2)^2$, corresponding to three of the universal fits reported in Table XIII.

The two parameters β^2 and d^2 were set equal to the corresponding parameters of the universal fits in Table XIII. The best-fit parameters of these fits are plotted versus x in Fig. 31, and the total χ^2 for the 11 fixed-x fits (64 degrees of freedom) of each function are also given. The solid lines in this figure represent the values of the best-fit parameters of the corresponding universal fits from Table XIII. Fixed-x fits of other functional forms were also attempted. In particular, a form $R=c(x)/Q^2$ fits the R_p data well for $x \geq 0.25$ but has less than 20% confidence for $x \leq 0.2$. The form $R=c(x)Q^2$ is consistent with the data for $x \leq 0.2$, but is a very poor fit at higher x. Over the full range of x, it is difficult to distinguish among the constant, the asymptotic $1/Q^2$, and the $1/\ln Q^2$ fits to R. The relatively large values of χ^2 obtained in the constant universal fits can be seen to be the result of a slow variation of R with x. For both the proton and deuteron, R varies from about 0.3 at low values of x to about 0.1 at the high values of x reported. On the other hand, the success of the universal $1/\ln Q^2$ fit can be attributed to the fact that it accomodates, perhaps fortuitously, this x variation of R_p and R_d quite well. The modified $1/Q^2$ universal fit also represents the low-x, low-Q^2 behavior of R_p and R_d fairly well, and provides an equally good fit as $1/\ln Q^2$ to all the data. In summary, the present data for R_p and R_d are consistent with either a constant, a $1/Q^2$, or a $1/\ln Q^2$ dependence in the Bjorken limit. The present errors for R do not allow us to distinguish among these three functional forms.

The x-Q^2 array also permitted a study of the kinematic variation of νR_p and νR_d for fixed values of x. Light-cone algebras with only spin-$\frac{1}{2}$ charged constituents predict[21,22] that νR should scale, i.e., $\nu R(x,Q^2)=a(x)$. If there are charged spin-0 partons in the nucleon,[23] then $\nu R(x,Q^2)=a(x)+\nu b(x)$, where $b(x)$ is the ratio of spin-0 to spin-$\frac{1}{2}$ contributions[69] to νW_2, in the limit of large Q^2. Other non-spin-$\frac{1}{2}$ contributions[67] to νW_2 would also result in a nonzero value of $b(x)$, as would also be expected in asymptotically free field theories.[70]

In Figs. 32, 33 νR_p and νR_d are plotted versus Q^2 for fixed values of x between 0.1 and 0.8. The solid lines represent least-squares fits of the form $\nu R=a+b\nu=a+(b/2Mx)Q^2$. Best-fit values of $b(x)$ and its random errors and systematic uncertainties are given in Table XIV for the eleven values of x studied. The five contributions to the systematic uncertainty in R_p and R_d also give uncertainties in the parameter b. The quadratic sum of the five such uncertainties in b is reported in Table XIV as Δb, the systematic uncertainly in b.

When these fits were restricted to $W \geq 2.0$ GeV, the best-fit values of b shifted by less than 1 standard deviation, except at $x=0.5$, where b_p shifted from 0.123 ± 0.075 to 0.023 ± 0.114, and b_d shifted from 0.234 ± 0.062 to 0.172 ± 0.089. When fits of the form $\nu R=a+b\nu$ were made to data for the x-Q^2 array restricted to experiments A and B, the results for b_p and b_d agreed with those of Table XIV within their random errors. For $0.25 \leq x \leq 0.80$, b_p is small and consistent with zero, within the random errors quoted. The average of b_p over this range of x is $\bar{b}_p=0.035 \pm 0.036$ with an estimated systematic uncertainty of 0.033. Over this same range of x, b_d is frequently inconsistent with zero, within 2 standard deviations. Its average value over this range is $\bar{b}_d=0.161 \pm 0.030$, with a systematic uncertainty of 0.037. The present results are consistent with the scaling of νR_p in this range of x, indicative of purely spin-$\frac{1}{2}$ constituents, in a parton model of the proton. The error in b, however, allows up to about a 10% spin-0 contribution to νW_2^p. The results are not consistent with scaling of νR_d. They are also consistent with about a 25% spin-0 contribution to νW_2^d. These spin-0 contributions would lead to nonvanishing values of R_p and R_d in the Bjorken limit.[23] Asymptotically free field theories[18] are also consistent with these

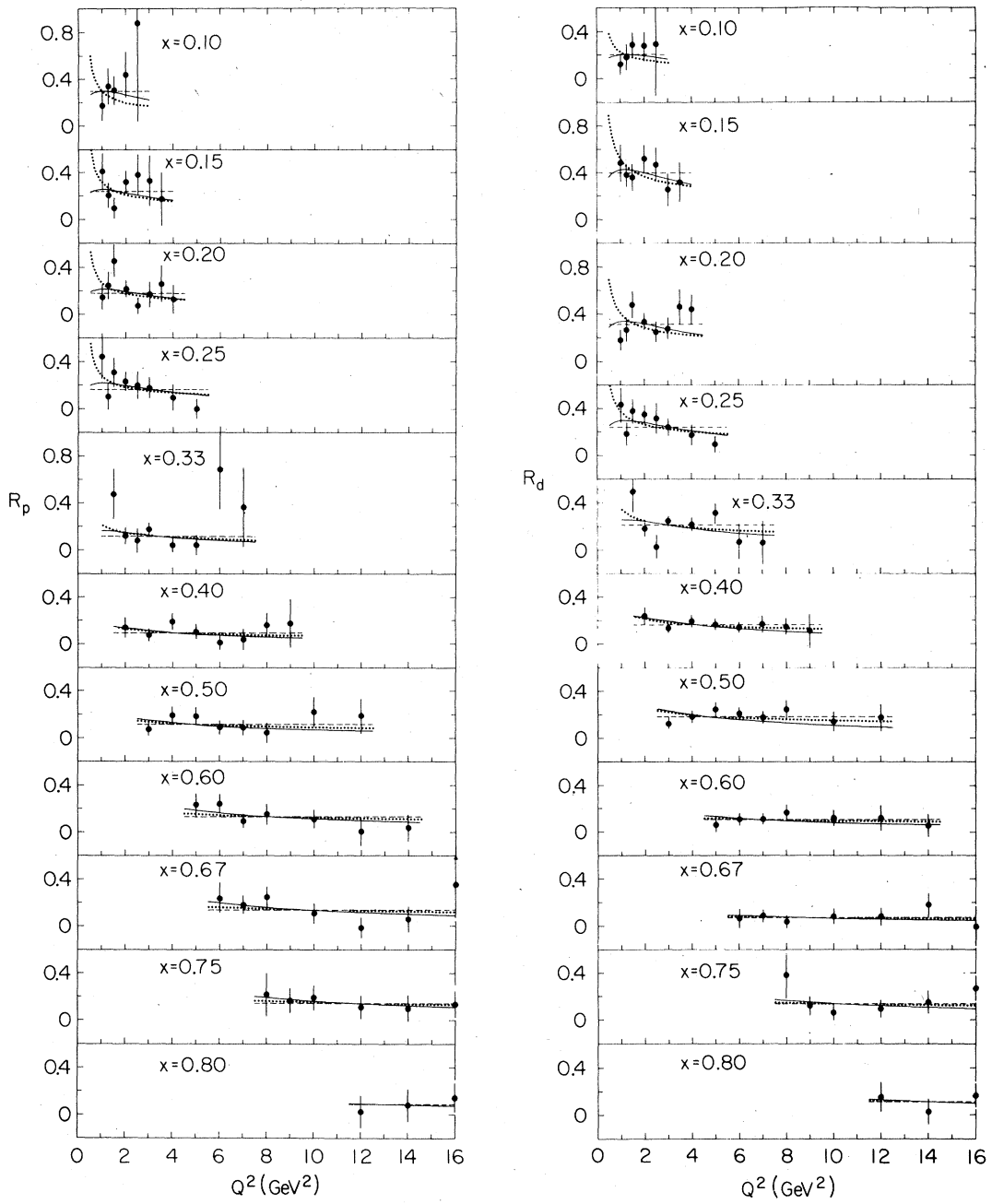

FIG. 30. The values R_p and R_d plotted against x for the 11 values of x studied. Errors shown are purely random. The dashed lines represent constant fits to R_p and R_d at each value of x. The solid lines and dotted lines represent fixed-x fits of the form $R = c(x)Q^2/(Q^2+d^2)^2$ and $R = \alpha^2(x)/\ln(Q^2/\beta^2)$ at each value of x.

results, as they predict[70] a small increment above exact scaling behavior for νR. Large values of b are encountered for $x \lesssim 0.2$, but a considerable portion of the data at these values of x is for $Q^2 \leq 2.0$ GeV^2, and the observed slope may represent only the low-Q^2 turn-on[59] of νW_2. One could argue that the Fermi motion of the nucleons within the deuteron might lead to a nonzero value of b_d, while b_p remained equal to zero. But as discussed in Appendix C, the approximate equality of the smearing ratios for W_1 and W_2 implies that smearing should have little effect upon R_d. Off-mass shell corrections to these smearing ratios are expected to reduce R_d at low Q^2, but these effects are estimated to increase b_d by about 0.01. It is presently unclear whether the behavior of νR_d at

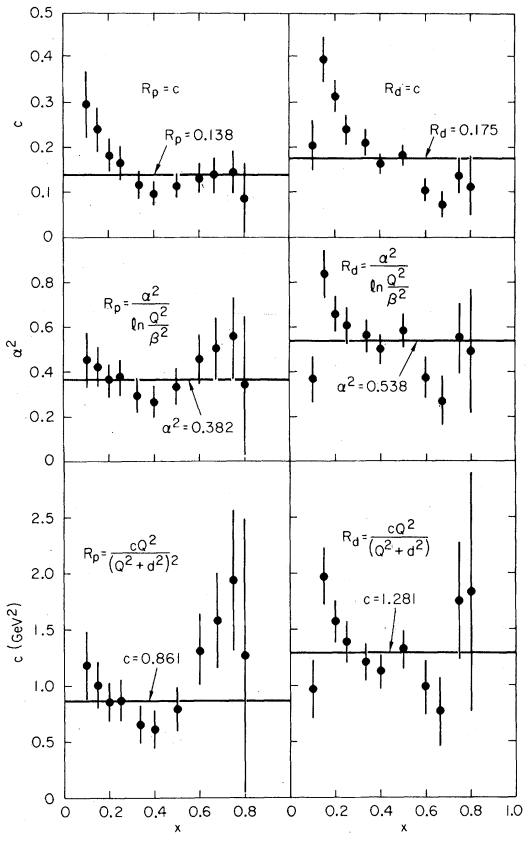

FIG. 31. Best-fit parameters of fixed-x fits to the R_p and R_d data. Errors shown are purely random.

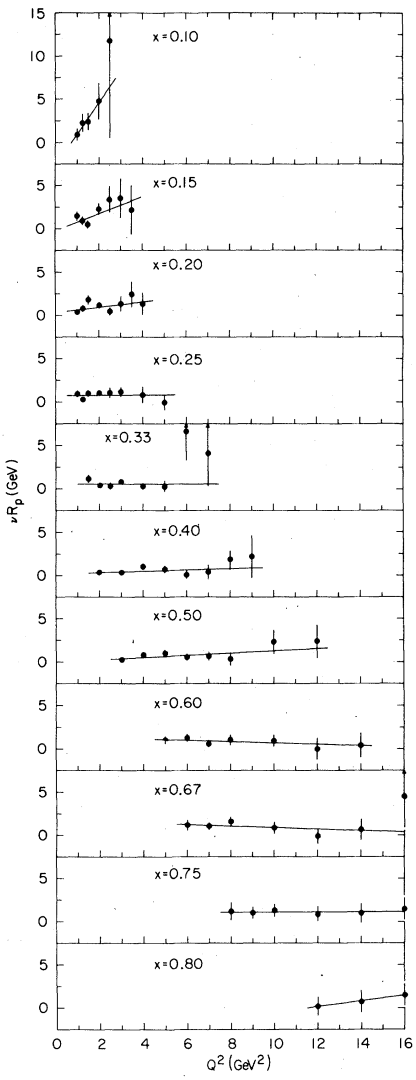

FIG. 32. The quantity νR_p plotted against Q^2 for the 11 fixed values of x studied.

fixed x is indicative of a non-spin-$\frac{1}{2}$ contribution to inelastic e-d scattering or is due to some aspect of deuteron binding not now understood.

Recently, the Callan-Gross relation $R = Q^2/\nu^2$ (i.e., $F_2 = xF_1$) has been assumed in the analysis of neutrino experiments.[71] As indicated earlier, the parton model predicts $R = a(x)/\nu$ for general spin-$\frac{1}{2}$ constituents. The Callan-Gross relation is specifically for *unbound* constituents [i.e., $a(x) = Q^2/\nu = 2Mx$]. We note that as $\nu \to \infty$, $R \to 0$ in either case and the relation $F_2 = xF_1$ is satisfied. Here we present the deviation

$$K = \frac{F_2}{(xF_1)} - 1 = \left(\frac{\nu^2}{Q^2}\right)\left[\frac{1+R}{1+\nu^2/Q^2}\right] - 1 \qquad (6.4)$$

for the Q^2, ν range of this experiment. Figure 34 shows K averaged over Q^2 versus x for the proton and deuteron, and Fig. 35 shows K averaged over x versus Q^2. Significant deviations from Callan-Gross are seen at low x and low Q^2. These deviations are expected and may come from binding effects of spin-$\frac{1}{2}$ constituents, low- and high-Q^2 nonscaling effects, or spin-0 constituents.

D. Separation of the structure functions

At each kinematic point of the x-Q^2 array, the quantities $2MW_1$ and νW_2 were derived from σ_L and σ_T for both proton and deuteron according to Eq. (1.3). The separated values of $F_1(x, Q^2) = 2MW_1(x, Q^2)$ and $F_2(x, Q^2) = \nu W_2(x, Q^2)$ are reported in Table XV, along with the random errors and relative systematic uncertainties in these quantities. Plots of $F_1(x, Q^2)$ and $F_2(x, Q^2)$ versus Q^2 for selected fixed values of x are presented in Figs. 36 and 37 for both the proton and deuteron. The random errors in F_1 and F_2 were computed from the error matrix of the least-squares fit to Σ, and therefore include a contribution from the random error in R at each point. As most of our

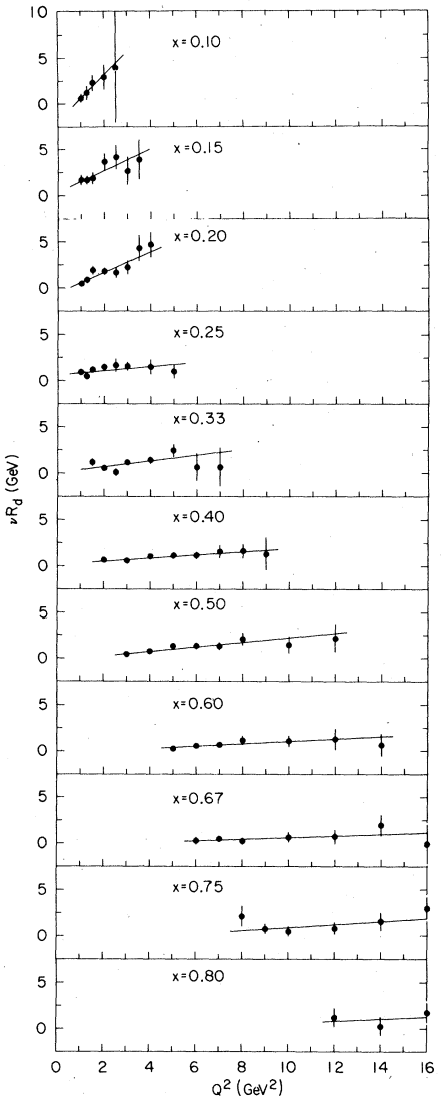

FIG. 33. The quantity νR_d plotted against Q^2 for the 11 fixed values of x studied.

TABLE XIV. Best-fit parameters b and their random errors and systematic uncertainties from least-squares fits of the form $\nu R = a + b\nu$.

x	b_p	Δb_p	b_d	Δb_d
0.10	0.679±0.330	0.130	0.478±0.231	0.109
0.15	0.278±0.166	0.111	0.331±0.145	0.133
0.20	0.118±0.090	0.058	0.415±0.088	0.101
0.25	0.014±0.084	0.033	0.108±0.071	0.037
0.33	0.003±0.098	0.030	0.195±0.086	0.029
0.40	0.055±0.066	0.032	0.129±0.055	0.036
0.50	0.123±0.075	0.034	0.234±0.062	0.039
0.60	−0.087±0.123	0.036	0.148±0.096	0.038
0.67	−0.111±0.148	0.049	0.114±0.116	0.040
0.75	0.009±0.221	0.031	0.233±0.198	0.033
0.80	0.496±0.642	0.049	0.169±0.562	0.045

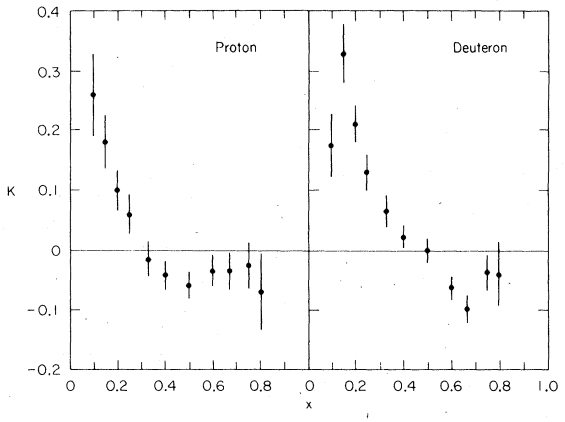

FIG. 34. Values of K, averaged over Q^2, plotted against x for the proton and deuteron. K is defined in Eq. (6.4).

cross-section data were measured at values of ϵ between 0.6 and 0.9, this contribution is, in general, much larger for F_1 (corresponding to $\epsilon = 0$) than for F_2 (corresponding to $\epsilon = 1$). The relative uncertainties, which arise from the normalization uncertainties and from the cross-section uncertainties listed in Table VII, are those which can affect the Q^2 dependence of F_1 and F_2. They were estimated in a manner similar to that used to estimate the uncertainties in R, and were added in quadrature to produce the numbers listed under Δ in Table XV. The relative uncertainty

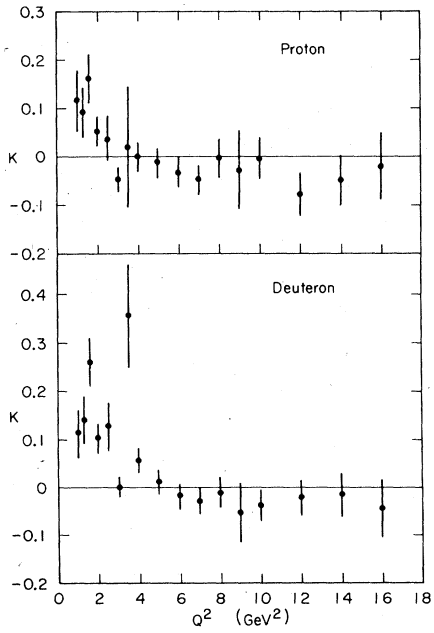

FIG. 35. Values of K, averaged over x, plotted against Q^2 for the proton and deuteron. K is defined in Eq. (6.4).

TABLE XV. Separated values of $2MW_1$ and νW_2 and their random errors and relative systematic uncertainties.

x	Q^2 (GeV^2)	$2MW_1^p$	Δ	νW_2^p	Δ	$2MW_1^d$	Δ	νW_2^d	Δ
0.10	1.00	2.7320 ± 0.2435	0.2168	0.3100 ± 0.0086	0.0088	5.3689 ± 0.3524	0.4173	0.5808 ± 0.0126	0.0206
0.10	1.25	2.5293 ± 0.2333	0.2083	0.3291 ± 0.0092	0.0002	5.3258 ± 0.4165	0.4067	0.6120 ± 0.0154	0.0205
0.10	1.50	2.6576 ± 0.1983	0.2238	0.3381 ± 0.0093	0.0095	5.0837 ± 0.3422	0.4125	0.6402 ± 0.0145	0.0215
0.10	2.00	2.5390 ± 0.2401	0.2242	0.3598 ± 0.0172	0.0099	5.1486 ± 0.3443	0.4315	0.6441 ± 0.0248	0.0225
0.10	2.50	2.3170 ± 0.6479	0.2683	0.4295 ± 0.0737	0.0193	5.2006 ± 0.9577	0.5660	0.6649 ± 0.1090	0.0451
0.15	1.00	1.6898 ± 0.1661	0.1565	0.3308 ± 0.0062	0.0098	2.9340 ± 0.2830	0.2900	0.6032 ± 0.0093	0.0217
0.15	1.25	1.9501 ± 0.1395	0.1574	0.3315 ± 0.0074	0.0101	3.1496 ± 0.1921	0.2917	0.6118 ± 0.0103	0.0230
0.15	1.50	2.1034 ± 0.1369	0.1514	0.3283 ± 0.0068	0.0096	3.2092 ± 0.2393	0.2555	0.6216 ± 0.0101	0.0219
0.15	2.00	1.8090 ± 0.0937	0.1404	0.3448 ± 0.0089	0.0102	2.9493 ± 0.2033	0.2427	0.6459 ± 0.0132	0.0236
0.15	2.50	1.7987 ± 0.1546	0.1513	0.3617 ± 0.0162	0.0143	3.0912 ± 0.2153	0.2792	0.0613 ± 0.0223	0.0330
0.15	3.00	1.8201 ± 0.1803	0.1502	0.3544 ± 0.0249	0.0146	3.5006 ± 0.2277	0.2940	0.6407 ± 0.0336	0.0345
0.15	3.50	1.9293 ± 0.2252	0.1548	0.3321 ± 0.0277	0.0147	3.4415 ± 0.2787	0.2923	0.6649 ± 0.0357	0.0369
0.20	1.00	1.5845 ± 0.1287	0.1575	0.3183 ± 0.0049	0.0089	2.7658 ± 0.1911	0.3209	0.5720 ± 0.0073	0.0197
0.20	1.25	1.4686 ± 0.1173	0.1416	0.3288 ± 0.0061	0.0097	2.5827 ± 0.1845	0.2822	0.5880 ± 0.0085	0.0213
0.20	1.50	1.2762 ± 0.1070	0.1205	0.3399 ± 0.0056	0.0098	2.2135 ± 0.1557	0.2356	0.6000 ± 0.0076	0.0212
0.20	2.00	1.4645 ± 0.0710	0.1029	0.3333 ± 0.0058	0.0093	2.4341 ± 0.1128	0.1784	0.6076 ± 0.0077	0.0205
0.20	2.50	1.6122 ± 0.0776	0.1067	0.3270 ± 0.0076	0.0098	2.5299 ± 0.1466	0.1873	0.5986 ± 0.0108	0.0221
0.20	3.00	1.5177 ± 0.0948	0.1086	0.3394 ± 0.0124	0.0124	2.5064 ± 0.1276	0.1996	0.6113 ± 0.0169	0.0277
0.20	3.50	1.4257 ± 0.1150	0.1036	0.3457 ± 0.0171	0.0132	2.2603 ± 0.1571	0.1900	0.6367 ± 0.0236	0.0303
0.20	4.00	1.4912 ± 0.0967	0.1021	0.3247 ± 0.0156	0.0130	2.2965 ± 0.1345	0.1844	0.6385 ± 0.0218	0.0312
0.25	1.00	1.0798 ± 0.1275	0.1642	0.3184 ± 0.0046	0.0087	1.8854 ± 0.1832	0.3399	0.5509 ± 0.0066	0.0186
0.25	1.25	1.3236 ± 0.1200	0.1383	0.3112 ± 0.0046	0.0088	2.1859 ± 0.1662	0.2872	0.5500 ± 0.0067	0.0191
0.25	1.50	1.1189 ± 0.0962	0.1162	0.3188 ± 0.0042	0.0088	1.8561 ± 0.1320	0.2364	0.5575 ± 0.0058	0.0189
0.25	2.00	1.1714 ± 0.0662	0.0858	0.3253 ± 0.0047	0.0087	1.8545 ± 0.0985	0.1508	0.5623 ± 0.0063	0.0184
0.25	2.50	1.1623 ± 0.0920	0.0872	0.3195 ± 0.0072	0.0095	1.8625 ± 0.1642	0.1633	0.5634 ± 0.0100	0.0206
0.25	3.00	1.1688 ± 0.0612	0.0787	0.3211 ± 0.0086	0.0100	1.9217 ± 0.0848	0.1339	0.5559 ± 0.0113	0.0207
0.25	4.00	1.1873 ± 0.0792	0.0720	0.3082 ± 0.0129	0.0100	1.9741 ± 0.1030	0.1325	0.5493 ± 0.0176	0.0223
0.25	5.00	1.2402 ± 0.0653	0.0716	0.2959 ± 0.0112	0.0103	2.0184 ± 0.0838	0.1273	0.5295 ± 0.0142	0.0236
0.33	1.50	0.7480 ± 0.1035	0.1193	0.2916 ± 0.0038	0.0079	1.2260 ± 0.1298	0.2470	0.4827 ± 0.0053	0.0163
0.33	2.00	0.8939 ± 0.0505	0.0677	0.2794 ± 0.0033	0.0071	1.4293 ± 0.0659	0.1277	0.4676 ± 0.0046	0.0146
0.33	2.50	0.8863 ± 0.0734	0.0749	0.2756 ± 0.0043	0.0076	1.5366 ± 0.1389	0.1451	0.4559 ± 0.0062	0.0157
0.33	3.00	0.8064 ± 0.0316	0.0467	0.2799 ± 0.0039	0.0070	1.2626 ± 0.0401	0.0777	0.4622 ± 0.0051	0.0145
0.33	4.00	0.8449 ± 0.0331	0.0449	0.2674 ± 0.0057	0.0072	1.2266 ± 0.0442	0.0733	0.4534 ± 0.0080	0.0146
0.33	5.00	0.8084 ± 0.0452	0.0435	0.2600 ± 0.0080	0.0078	1.1362 ± 0.0569	0.0750	0.4590 ± 0.0106	0.0164
0.33	6.00	0.5898 ± 0.0765	0.0312	0.3114 ± 0.0243	0.0069	1.2554 ± 0.0927	0.0603	0.4201 ± 0.0301	0.0092
0.33	7.00	0.6487 ± 0.0857	0.0323	0.2795 ± 0.0336	0.0063	1.2306 ± 0.1015	0.0588	0.4124 ± 0.0401	0.0094
0.40	2.00	0.6927 ± 0.0464	0.0578	0.2464 ± 0.0028	0.0062	1.0314 ± 0.0573	0.1054	0.3985 ± 0.0038	0.0118
0.40	3.00	0.6342 ± 0.0250	0.0356	0.2303 ± 0.0032	0.0055	0.9751 ± 0.0299	0.0594	0.3732 ± 0.0042	0.0109
0.40	4.00	0.5570 ± 0.0252	0.0309	0.2331 ± 0.0041	0.0057	0.8831 ± 0.0302	0.0516	0.3700 ± 0.0054	0.0117
0.40	5.00	0.5683 ± 0.0229	0.0272	0.2259 ± 0.0049	0.0054	0.8589 ± 0.0277	0.0433	0.3610 ± 0.0062	0.0097
0.40	6.00	0.5731 ± 0.0228	0.0259	0.2118 ± 0.0044	0.0052	0.8422 ± 0.0257	0.0421	0.3521 ± 0.0054	0.0099
0.40	7.00	0.5430 ± 0.0280	0.0238	0.2091 ± 0.0082	0.0056	0.8108 ± 0.0314	0.0358	0.3501 ± 0.0098	0.0079
0.40	8.00	0.4982 ± 0.0261	0.0218	0.2170 ± 0.0088	0.0058	0.7907 ± 0.0290	0.0343	0.3399 ± 0.0105	0.0079
0.40	9.00	0.4746 ± 0.0401	0.0205	0.2104 ± 0.0202	0.0048	0.7868 ± 0.0476	0.0335	0.3289 ± 0.0246	0.0074
0.50	3.00	0.4129 ± 0.0194	0.0248	0.1714 ± 0.0021	0.0040	0.6160 ± 0.0228	0.0417	0.2679 ± 0.0028	0.0075
0.50	4.00	0.3439 ± 0.0167	0.0182	0.1677 ± 0.0028	0.0037	0.5286 ± 0.0188	0.0302	0.2558 ± 0.0038	0.0072
0.50	5.00	0.3166 ± 0.0164	0.0153	0.1593 ± 0.0029	0.0033	0.4644 ± 0.0183	0.0236	0.2454 ± 0.0036	0.0056
0.50	6.00	0.3181 ± 0.0134	0.0136	0.1505 ± 0.0027	0.0033	0.4516 ± 0.0156	0.0217	0.2380 ± 0.0034	0.0060
0.50	7.00	0.3014 ± 0.0136	0.0135	0.1453 ± 0.0029	0.0031	0.4365 ± 0.0150	0.0210	0.2279 ± 0.0033	0.0055
0.50	8.00	0.2974 ± 0.0159	0.0115	0.1392 ± 0.0047	0.0026	0.4080 ± 0.0176	0.0163	0.2285 ± 0.0056	0.0042
0.50	10.00	0.2555 ± 0.0160	0.0112	0.1429 ± 0.0067	0.0030	0.4063 ± 0.0174	0.0163	0.2124 ± 0.0075	0.0045
0.50	12.00	0.2501 ± 0.0175	0.0095	0.1379 ± 0.0083	0.0033	0.3823 ± 0.0205	0.0143	0.2084 ± 0.0104	0.0048
0.60	5.00	0.1736 ± 0.0114	0.0082	0.1023 ± 0.0018	0.0020	0.2902 ± 0.0130	0.0126	0.1470 ± 0.0023	0.0028
0.60	6.00	0.1601 ± 0.0085	0.0072	0.0983 ± 0.0018	0.0020	0.2542 ± 0.0094	0.0111	0.1395 ± 0.0021	0.0030
0.60	7.00	0.1624 ± 0.0070	0.0068	0.0900 ± 0.0015	0.0020	0.2338 ± 0.0078	0.0106	0.1319 ± 0.0017	0.0033
0.60	8.00	0.1484 ± 0.0081	0.0055	0.0884 ± 0.0022	0.0017	0.2142 ± 0.0093	0.0078	0.1290 ± 0.0026	0.0024

TABLE XV. (*Continued*)

x	Q^2 (GeV^2)	$2MW_1^p$	Δ	νW_2^p	Δ	$2MW_1^d$	Δ	νW_2^d	Δ
0.60	10.00	0.1370±0.0068	0.0047	0.0809±0.0021	0.0016	0.1994±0.0083	0.0067	0.1188±0.0027	0.0022
0.60	12.00	0.1335±0.0081	0.0045	0.0726±0.0046	0.0016	0.1882±0.0097	0.0064	0.1144±0.0056	0.0024
0.60	14.00	0.1252±0.0072	0.0042	0.0712±0.0041	0.0016	0.1807±0.0088	0.0057	0.1047±0.0050	0.0022
0.67	6.00	0.0997±0.0085	0.0042	0.0653±0.0014	0.0012	0.1651±0.0099	0.0065	0.0929±0.0018	0.0017
0.67	7.00	0.0937±0.0051	0.0039	0.0604±0.0011	0.0012	0.1469±0.0060	0.0059	0.0868±0.0013	0.0018
0.67	8.00	0.0861±0.0048	0.0031	0.0597±0.0013	0.0013	0.1392±0.0054	0.0046	0.0804±0.0015	0.0015
0.67	10.00	0.0813±0.0044	0.0028	0.0519±0.0015	0.0009	0.1182±0.0052	0.0039	0.0737±0.0017	0.0013
0.67	12.00	0.0784±0.0043	0.0029	0.0455±0.0019	0.0008	0.1069±0.0050	0.0037	0.0677±0.0021	0.0012
0.67	14.00	0.0699±0.0040	0.0022	0.0444±0.0022	0.0009	0.0960±0.0048	0.0030	0.0677±0.0027	0.0014
0.67	16.00	0.0573±0.0074	0.0018	0.0470±0.0039	0.0010	0.0980±0.0090	0.0029	0.0592±0.0047	0.0012
0.75	8.00	0.0411±0.0051	0.0016	0.0300±0.0010	0.0006	0.0537±0.0064	0.0022	0.0445±0.0012	0.0008
0.75	9.00	0.0389±0.0028	0.0013	0.0279±0.0006	0.0005	0.0580±0.0034	0.0019	0.0400±0.0008	0.0007
0.75	10.00	0.0359±0.0024	0.0012	0.0267±0.0008	0.0005	0.0550±0.0028	0.0018	0.0369±0.0009	0.0006
0.75	12.00	0.0332±0.0020	0.0012	0.0237±0.0009	0.0004	0.0480±0.0023	0.0016	0.0339±0.0009	0.0006
0.75	14.00	0.0294±0.0018	0.0009	0.0213±0.0010	0.0004	0.0415±0.0022	0.0012	0.0314±0.0012	0.0006
0.75	16.00	0.0264±0.0016	0.0008	0.0199±0.0009	0.0004	0.0361±0.0019	0.0011	0.0305±0.0011	0.0006
0.80	12.00	0.0194±0.0018	0.0006	0.0133±0.0006	0.0002	0.0263±0.0020	0.0008	0.0204±0.0007	0.0003
0.80	14.00	0.0169±0.0014	0.0005	0.0125±0.0006	0.0002	0.0252±0.0016	0.0007	0.0179±0.0008	0.0003
0.80	16.00	0.0145±0.0010	0.0004	0.0116±0.0005	0.0002	0.0212±0.0012	0.0006	0.0173±0.0006	0.0003

VII. TESTS OF STRUCTURE-FUNCTION SCALING

A. Introduction

Experimental tests of structure-function scaling are fraught with ambiguity. Apparent deviations from exact scaling may arise from such diverse effects as two-photon exchange, low-Q^2 turn-on[59] of νW_2, s-channel resonance contributions, and nonleading terms in the light-cone expansion of the current commutator. They may obscure genuine scaling deviations predicted by field theories with parton structure,[15,16] anomalous dimensions,[17] and asymptotic freedom,[18] or arising from the production of charmed[72] or colored states.[73] Bjorken's original hypothesis[11] was that $2MW_1(\nu, Q^2)$ and $\nu W_2(\nu, Q^2)$ would scale in the variable $\omega = 2M\nu/Q^2$ (i.e., become functions only of ω) in the limit $\nu \to \infty$, $Q^2 \to \infty$, with ν/Q^2 held fixed. Within the experimental errors, the early data for νW_2^p was consistent with scaling in ω for $Q^2 \geq 1$ GeV^2 and $W \geq 2.6$ GeV. In this experiment, use of the scaling variable $\omega' = 1/x' = \omega + M^2/Q^2 = 1 + W^2/Q^2$

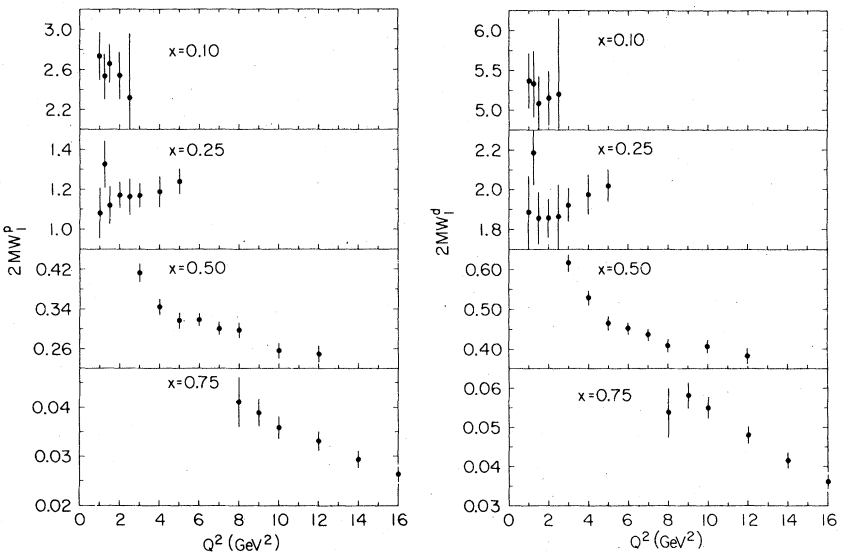

FIG. 36. Separated values of $2MW_1 = F_1(x, Q^2)$ for the proton and deuteron plotted against Q^2 for fixed values of x. The errors shown are purely random.

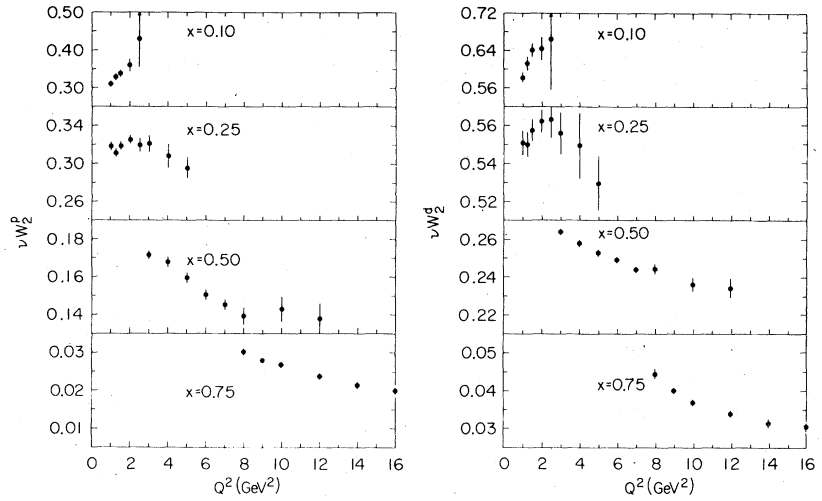

FIG. 37. Separated values of $\nu W_2 = F_2(x, Q^2)$ for the proton and deuteron plotted against Q^2 for fixed values of x. The errors shown are purely random.

extended the range of W for which scaling of νW_2^p was valid down to $W = 1.8$ GeV.[74] Other scaling variables[61,62,75,76] all of which approach ω as $Q^2 \to \infty$, have been proposed to fit the data; they are examined in Sec. VII B. In the remaining scaling tests of this section, only the variables ω and ω' are used and deviations from scaling in these variables are examined. Only data for $Q^2 \geq 2$ GeV^2 and $W \geq 2$ GeV are used in these scaling tests. These restrictions ensured that the tests were influenced neither by the prominent electroproduction resonances nor by the low-Q^2 turn-on of νW_2.

The two independent structure functions $F_1 = 2MW_1(x, Q^2)$ and $F_2 = \nu W_2(x, Q^2)$ for the proton and deuteron, as given in Table XV and plotted in Figs. 36 and 37, were used for the scaling tests reported in Sec. VII A. This method had the advantage that the extracted structure functions were independent of any assumptions about the Q^2 dependence of R. These "separated" data were best suited for a comparison of the Q^2 dependence of the four structure functions $2MW_1^p$, νW_2^p, and $2MW_1^d$, and νW_2^d in the same range of kinematics. This method of extracting the structure functions had the disadvantage of limited precision, as the random error in R at each kinematic point was propagated into the error in the two structure functions. The range of Q^2 and the number of data points available at each x were also somewhat limited in this method.

The second method used to extract the structure functions was similar to that used in earlier scaling tests.[7,20] In this method the structure function νW_2 was extracted from the inelastic-cross-section data using Eq. (1.3), and assuming a functional form for R to be valid throughout the kinematic region in which the cross sections had been measured. Whereas the constant value $R_p = 0.18$ was used to extract νW_2^p in the earlier tests, we used the modified spin-$\frac{1}{2}$ form[70] $R = cQ^2/(Q^2 + d^2)^2$ with proton coefficients taken from Table XIII. This functional form has the two advantages that it fits the R data better than the constant form, and that it satisfies gauge invariance as $Q^2 \to 0$, i.e., $R \to 0$ in that limit. Inelastic e-p, e-d, and e-n cross sections from experiments A and B only (Table V) were used in this method. Cross sections from experiment B were normalized to those of experiment A by the normalization factor $N_{AB} = 1.010$ discussed in Sec. V F. The uncertainty in the extracted values of $2MW_1$ owing to our assumptions about R, was deemed too large in this method, and no results are presented for that structure function. The corresponding uncertainty in νW_2 was always less than the statistical error in $2MW_1$. Because of the statistical accuracy of this large body of data for νW_2, this method was particularly appropriate for a study of the possible functional forms of Q^2-dependent scale-breaking terms in νW_2.

A rough test of scaling is provided by plots of all these "extracted" data for νW_2^p, νW_2^d, and νW_2^n versus x, as in Fig. 38, or versus x', as in Fig. 39. To a fairly good approximation these data describe single functions of x or x', faring better in the second variable. The usefulness of this approach is limited, however, as small deviations (on the order of 10–20%) from exact scaling would not be apparent in these plots. More quantitative scaling tests were provided by fits of the form $\nu W_2 = f(\xi)h(Q^2)$, where ξ is one of the pro-

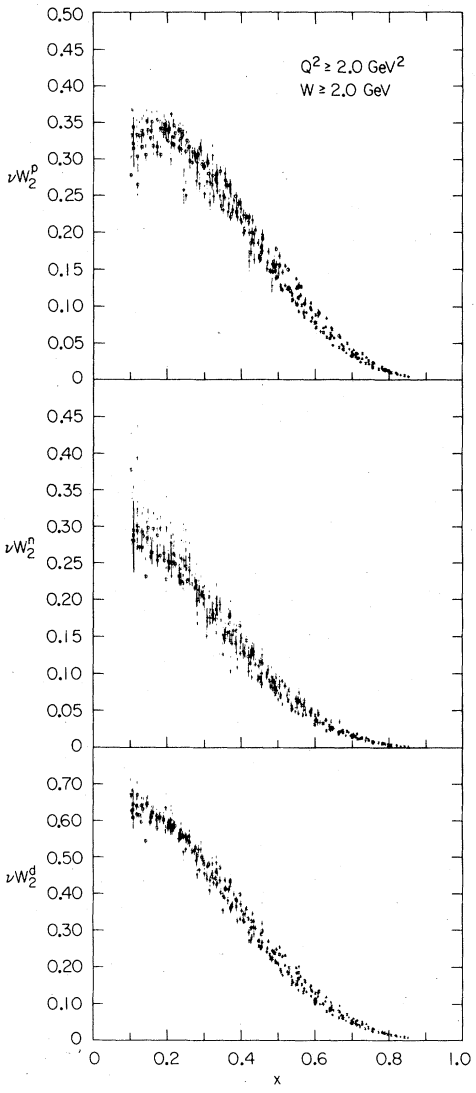

FIG. 38. Values of νW_2^p, νW_2^n, and νW_2^d plotted against x. The errors shown are purely random.

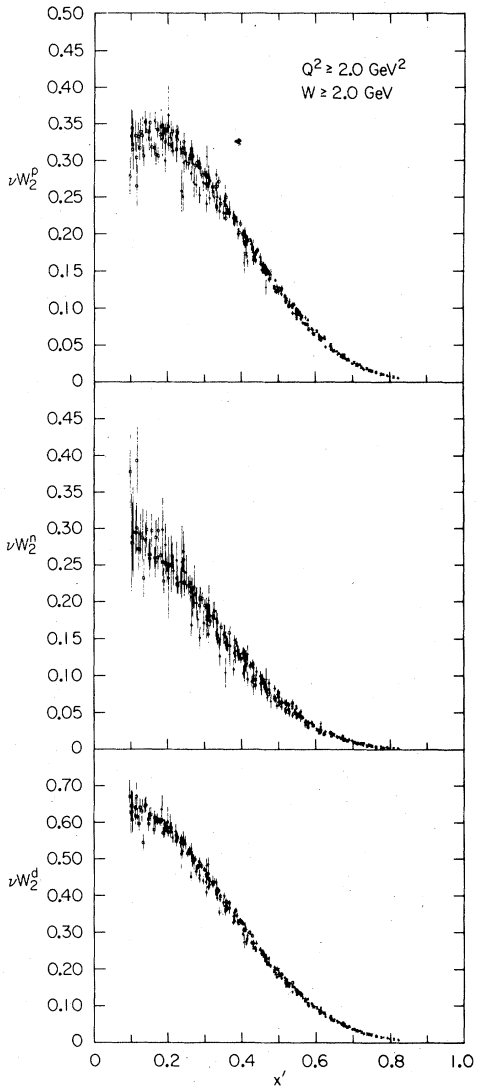

FIG. 39. Values of νW_2^p, νW_2^n, and νW_2^d plotted against x'. The errors shown are purely random.

posed scaling variables, and $h(Q^2)$ is either unity or a scale-breaking function. Such is the procedure used in Sec. VII B, where several proposed scaling variables are compared, and in Sec. VII C, where deviations from scaling of νW_2^p, νW_2^d, and νW_2^n are compared. The disadvantage of such an approach is that the functional form assumed for the Q^2-dependent term $h_i(Q^2)$ must be the same for all values of ξ. This approach is not compatible with certain field-theory models[17,18,77] that predict a rise in the structure functions at low x and a falloff at larger values of x. Deviations from scaling in ω were further examined in Sec. VII D by fitting functions with explicit Q^2-dependent terms to F_1 and F_2 for 11 fixed values of $x = 1/\omega$ in the range $0.1 \leq x \leq 0.8$. The separated $2MW_1$ and νW_2 data of Table XV were ideally suited to this task, but the accuracy of the results was limited by the accuracy of the separated structure functions and the ranges of Q^2 available at each x. More extensive studies of the Q^2 dependence of νW_2 were possible using values of this structure function that had been extracted from interpolated cross sections using the fit $R = cQ^2/(Q^2 + d^2)^2$. The normalized cross section from experiments A and B were first interpolated at fixed E and θ to values of E' corresponding to the 11 values of x used in the x-Q^2 array. These data for $\nu W_2(x, Q^2)$ then permitted extensive tests of the various functional forms proposed for deviations from exact Bjorken scaling.

TABLE XVI. Deviations from scaling in ω, from least-squares fits of the form $F_i(x,Q^2) = f_i(\omega)h_i(Q^2)$ to the separated $2MW_1$ and νW_2 data for $W \geq 2.0$ GeV, $Q^2 \geq 2.0$ GeV^2.

	Fitted data	$h_i(Q^2) = 1 - 2Q^2/\Lambda_i^2$		$h_i(Q^2) = (1+Q^2/\Lambda_i^2)^{-2}$	
		Λ_1^{-2} (GeV^{-2})	Λ_2^{-2} (GeV^{-2})	Λ_1^{-2} (GeV^{-2})	Λ_2^{-2} (GeV^{-2})
p	$0.1 \leq x \leq 0.8$	0.0144 ± 0.0014	0.0141 ± 0.0008	0.0225 ± 0.0038	0.0204 ± 0.0017
p	$0.3 \leq x \leq 0.8$	0.0147 ± 0.0013	0.0144 ± 0.0008	0.0245 ± 0.0040	0.0213 ± 0.0009
d	$0.1 \leq x \leq 0.8$	0.0162 ± 0.0012	0.0118 ± 0.0008	0.0270 ± 0.0039	0.0155 ± 0.0015
d	$0.3 \leq x \leq 0.8$	0.0164 ± 0.0012	0.0125 ± 0.0009	0.0294 ± 0.0043	0.0173 ± 0.0008

B. Comparison of $2MW_1$ and νW_2

The two independent structure functions $F_1 = 2MW_1(x,Q^2)$ and $F_2 = \nu W_2(x,Q^2)$ reported in Table XV were used in the scaling tests reported here. As mentioned earlier only data for $Q^2 \geq 2$ GeV^2 and $W \geq 2$ GeV were used in these tests. Scaling in the two variables $\xi = \omega$ and $\xi = \omega'$ was tested by fitting functions of the form $F_i(x,Q^2) = f_i(\xi)h_i(Q^2)$ to these proton and deuteron data for F_1 and F_2. Here $f_1(\xi) = \sum a_j(1 - 1/\xi)^j$ and $f_2(\xi) = \sum b_j(1 - 1/\xi)^j$, where j ranges from 3 to 7. Three forms for $h_j(Q^2)$ were tested: a constant $h_i(Q^2) = 1$ for exact scaling; the scale-breaking form $h_i(Q^2) = 1 - 2Q^2/\Lambda_i^2$ suggested by constituent models[15,16] wherein $1/\Lambda^2$ is the parton "size," and the propagator form[16,78] $h_i(Q^2) = (1 + Q^2/\Lambda_i^2)^{-2}$ which is expected in some finite-size constituent models[16] as well as in heavy-photon theories.[78] Best-fit values for Λ_i^2 and for the polynomial coefficients a_j and b_j were obtained simultaneously by least-squares fits. Our studies indicated that the results for Λ_1^2 and Λ_2^2 were independent of the functional forms chosen for $f_1(\xi)$ and $f_2(\xi)$. The fits provided a comparison of deviations from scaling in $2MW_1$ and νW_2 for both the proton and the deuteron, independent of assumptions about R. In particular, they permit unbiased tests of models[16] that predict a larger scaling violation for $2MW_1$ than for νW_2.

The best-fit parameters $1/\Lambda_1^2$ and $1/\Lambda_2^2$ of fits in the scaling variable $\xi = \omega$ are presented in Table XVI. Systematic uncertainties in these quantities arise from the same effects that led to the relative uncertainties in F_1 and F_2 listed in Table XV. These systematic uncertainties were added in quadrature and included in the errors quoted. For $\xi = \omega$, the two scale-breaking forms listed in Table XVI provided much better fits than the exact scaling form $F_i(x,Q^2) = f_i(\omega)$. Over the full range of x, the best-fit values for $1/\Lambda_1^2$ and $1/\Lambda_2^2$ were essentially the same for the proton, but were different by about 2 standard deviations for the case of the deuteron. This difference may well have arisen from smearing effects,[20] or resonance contributions[79] at low W, for $1/\Lambda_1^2$ and $1/\Lambda_2^2$ were equal within 1 standard deviation when the deuteron data were restricted to $W \geq 2.6$ GeV. For $0.3 \leq x \leq 0.8$, the proton coefficients for the scale-breaking form $h_i(Q^2) = 1 - 2Q^2/\Lambda_i^2$ are in agreement with the values $1/\Lambda_1^2 = 0.0162 \pm 0.0024$ and $1/\Lambda_2^2 = 0.0134 \pm 0.0013$ obtained earlier[24,26] for $0.33 \leq x \leq 0.67$ using data from experiments A and C. The results for $1/\Lambda_1^2$ in the propagator scale-breaking form are also in agreement with the results of similar fits to recent data[76] for $2MW_1^p$ in the range $0.4 \leq x \leq 0.9$, where a value of $1/\Lambda_1^2 = 0.0233 \pm 0.0008$ was reported. For $x < 0.3$, both the proton and deuteron structure functions differed from scaling behavior in ω by less than 2 standard deviations. A comparison of these fits with the structure-function data is presented in Figs. 40 and 41, where ratios $F_i(x,Q^2)/f_i(\omega)$ have been plotted versus Q^2 at fixed x. The polynomial functions f_i correspond to the structure-function fits of the form $F_i(x,Q^2) = f_i(\omega)(1 - 2Q^2/\Lambda_i^2)$ to all the data in the kinematic range $W \geq 2$ GeV, $Q^2 \geq 2$ GeV^2, $0.1 \leq x \leq 0.8$, as listed in Table XVI. The solid lines represent the best fits to these data of the two scale-breaking forms listed in that table.

The best-fit parameters $1/\Lambda_1^2$ and $1/\Lambda_2^2$ of fits to F_1 and F_2 using the scaling variable $\xi = \omega'$ are presented in Table XVII. Systematic uncertainties in these quantities were estimated in the same manner as they were for Table XVI, and are included in the errors quoted in Table XVII. Except for fits to νW_2^d, the two scale-breaking functions provided better fits to the data than the exact scaling form $F_i(x,Q^2) = f_i(\omega')$. All three functional forms fit the data for νW_2^d with a χ^2 of 0.9 per degree of freedom. The χ^2 for the fits listed in Table XVII ranged from 0.7 to 1.1 per degree of freedom.

For data in the range $0.1 \leq x \leq 0.8$ as noted in Table XVII, the best-fit parameters $1/\Lambda_1^2$ and $1/\Lambda_2^2$ are equal for the proton, within errors; νW_2^p is inconsistent with scaling in ω', while $2MW_1^p$ is barely consistent, at the 2 standard-deviation level. For the range $0.3 \leq x \leq 0.8$, the coefficients for the linear scale-breaking form are consistent with the values $1/\Lambda_1^2 = 0.0049 \pm 0.0035$ and $1/\Lambda_2^2 = 0.0020 \pm 0.0018$ reported earlier[26] for $0.33 \leq x \leq 0.67$ using data from experiments A and

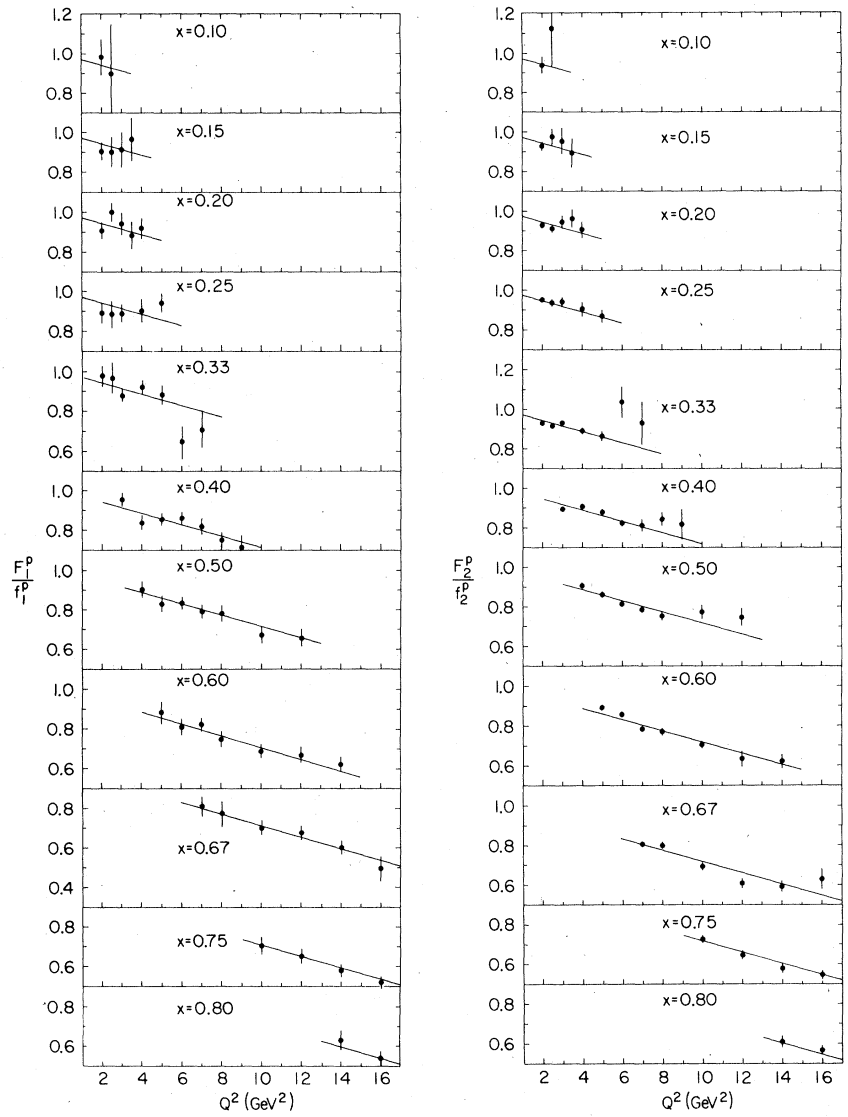

FIG. 40. Ratios of $F_1^p = 2MW_1^p$ and $F_2^p = \nu W_2^p$ to the polynomials $f_1(x)$ and $f_2(x)$ taken from least-squares fits of the form $F_i(x, Q^2) = f_i(x)(1 - 2Q^2/\Lambda_i^2)$ to all the data for $W \geq 2.0$ GeV and $Q^2 \geq 2.0$ (GeV/c)^2 in Table XV.

C. The results for $1/\Lambda_1^2$ in the propagator form are also consistent with the results of similar fits to the recent data for $2MW_1^p$ in the range $0.4 \leq x \leq 0.9$, where a value of $1/\Lambda_1^2 = 0.0078 \pm 0.0006$ was reported.[76] For either range of x, νW_2^d is consistent with scaling in ω', but $2MW_1^d$ is not. However, if we restrict the data to $W \geq 2.6$ GeV the best-fit parameters $1/\Lambda_1^2$ and $1/\Lambda_2^2$ are equal within 1 standard deviation and consistent with zero. In the range $0.1 \leq x \leq 0.3$, no violation of scaling in ω' was observed for either the proton or deuteron structure functions.

For the separated proton structure-function data restricted to the kinematic region ($W \geq 2.0$, $Q^2 \geq 2.0$, $x \geq 0.3$), the results of our scaling tests are unambiguous. Both structure functions are inconsistent with scaling in ω and νW_2^p is inconsistent with scaling in ω'. The structure function $2MW_1^p$ shows a violation of scaling in ω' that is equal to that exhibited by νW_2^p with breakdown parameters that are about the same, but the errors are larger and preclude a completely conclusive result. Over the range of Q^2 ($2.0 \leq Q^2 \leq 16.0$ GeV^2) studied in these tests, we see a 40% violation of scaling in ω and a 15% violation of scaling in ω', for $x \geq 0.3$. For either scaling variable, no evidence is seen for different values of $1/\Lambda_1^2$ and $1/\Lambda_2^2$, even when we restrict $W \geq 2.6$ GeV, and we conclude that they are equal, within the present errors. For the range $0.1 \leq x \leq 0.3$,

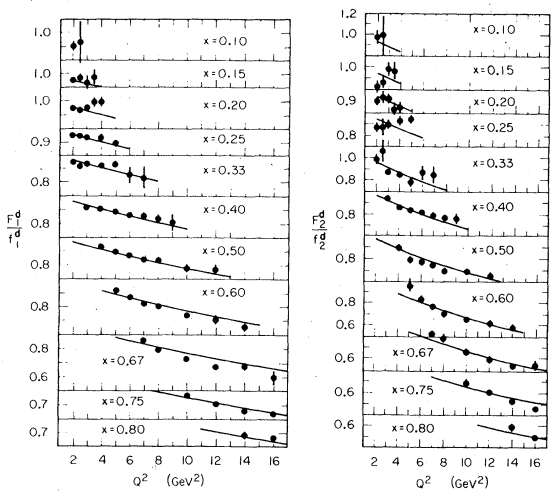

FIG. 41. Ratios of $F_1^d = 2MW_1^d$ and $F_2^d = \nu W_2^p$ to the polynomials $f_1(x)$ and $f_2(x)$ taken from least-squares fits of the form $F_i(x, Q^2) = f_i(x)(1 - 2Q^2/\Lambda_i^2)$ to all the data for $W \geq 2.0$ GeV and $Q^2 \geq 2.0$ (GeV/c)^2 in Table XV.

the two proton structure functions are consistent with scaling in both ω and ω'. The lack of any significant Q^2 dependence in this region, when combined with the observed violation of scaling for $x \geq 0.3$, is consistent with field-theoretic models[77] of nucleon structure.

The interpretation of our results for the deuteron structure functions is not so straightforward. For $x \geq 0.3$, both $2MW_1^d$ and νW_2^d are inconsistent with scaling in ω, with 35–45% scaling violations in the range of Q^2 studied. Over the same range of x, $2MW_1^d$ is inconsistent with scaling in ω', showing a 20% violation, while νW_2^d is consistent with scaling in ω'. For both scaling variables, the apparent difference between $1/\Lambda_1^2$ and $1/\Lambda_2^2$ disappears when the data are restricted to $W \geq 2.6$ GeV, and we can make no firm conclusions about its validity. Uncertainties in the off-mass-shell effects in the smearing corrections are largest at low W, but the magnitudes of these uncertainties, as estimated in Appendix C 2, cannot fully account for the observed difference between $1/\Lambda_1^2$ and $1/\Lambda_2^2$.

C. Comparison of scaling variables

In addition to the scaling variable ω originally suggested by Bjorken,[11] other scaling variables, all of which approach ω as $Q^2 \to \infty$, have been proposed to fit the low-Q^2 structure-function data. The variable $\omega_L = M/[(Q^2+\nu^2)^{-1/2} - \nu]$ has been suggested[61] as the scaling variable appropriate to light-cone algebras. The previously mentioned scaling variable $\omega' = \omega + M^2/Q^2$, which fit the earlier proton structure-function data quite well,[7] has been related to finite-energy sum rules.[74]

A phenomenological scaling variable $\omega_W = (2M\nu + M_a^2)/(Q^2 + M_b^2)$ (where M_a^2 and M_b^2 are fit parameters) that extends scaling of νW_2^p down to the photoproduction limit $Q^2 = 0$, was first suggested by Rittenberg and Rubinstein.[62] In an analysis[75] of previous electroproduction and photoproduction data, it was concluded the $\omega \nu W_2^p$, not νW_2^p, scaled in ω_W, within the experimental errors. Schwinger[80] has proposed a similar scaling variable ω_S, with $M_a^2 = \frac{3}{2}M^2$ and $M_b^2 = \frac{1}{2}M^2$, which are close to the best-fit values of these parameters in the fits to νW_2^p, νW_2^d, and νW_2^n discussed in Sec. VD 3. The scaling variable $\omega_A = \omega + M_A^2/Q^2$, where $M_A^2 = 1.42$ GeV^2, has been used to fit the recent data[76] for $2MW_1^p$.

The quality of scaling in any variable ξ was tested by fitting polynomials of the form $\sum a_j(1 - 1/\xi)^j$, where j ranged from 3 to 7, to the extracted data for νW_2^p, νW_2^d, or νW_2^n shown in Figs. 38 and 39. Only data for $W \geq 2$ GeV and $Q^2 \geq 2$ GeV^2 were used in these least-squares fits, yielding a total of 274 degrees of freedom for the proton data, and 257 for the deuteron and neutron data. Over the full range of x available here ($0.10 \leq x \leq 0.85$), these five-parameter polynomials provided better fits than polynomials with n ranging from 3 to 5. The values χ^2 for these fits, divided by the number of degrees of freedom N_D, are reported in Table XVIII. In the case of the last two scaling variables, ω_A and ω_W, the parameters M_A^2, M_a^2, and M_b^2 were fit simultaneously with the polynomial coefficients, and the number of degrees of freedom accordingly was smaller. The best-fit

TABLE XVII. Deviations from scaling in ω', from least-squares fits of the form $F_i(x, Q^2) = f_i(\omega')h_i(Q^2)$.

	Fitted data	$h_i(Q^2) = 1 - 2Q^2/\Lambda_i^2$		$h_i(Q^2) = (1 + Q^2/\Lambda_i^2)^{-2}$	
		Λ_1^{-2} (GeV^{-2})	Λ_2^{-2} (GeV^{-2})	Λ_1^{-2} (GeV^{-2})	Λ_2^{-2} (GeV^{-2})
p	$0.1 \leq x \leq 0.8$	0.0044 ± 0.0024	0.0054 ± 0.0012	0.0047 ± 0.0030	0.0059 ± 0.0015
p	$0.3 \leq x \leq 0.8$	0.0052 ± 0.0025	0.0055 ± 0.0013	0.0059 ± 0.0031	0.0061 ± 0.0017
d	$0.1 \leq x \leq 0.8$	0.0069 ± 0.0022	0.0009 ± 0.0013	0.0077 ± 0.0029	0.0009 ± 0.0013
d	$0.3 \leq x \leq 0.8$	0.0077 ± 0.0020	0.0017 ± 0.0015	0.0092 ± 0.0031	0.0017 ± 0.0016

TABLE XVIII. χ^2/N_D for various scaling fits to νW_2.

Fit data	N_D	ω	ω'	ω_L	ω_S	ω_A	ω_W
νW_2^p	274	10.05	2.30	4.56	4.56	1.43	1.42
νW_2^d	257	12.97	2.60	5.70	5.95	1.62	1.62
νW_2^n	257	2.33	1.32	1.63	1.68	1.29	1.29

values of M_A^2 obtained were 1.352 ± 0.032 for the proton, 1.294 ± 0.027 for the deuteron, and 1.109 ± 0.075 for the neutron. None of the scaling variables ω, ω', ω_L, or ω_S could provide even adequate fits to νW_2^p or νW_2^d, and only ω' could fit the neutron data with any degree of success. When only data for $W \geq 2.6$ GeV, $Q^2 \geq 2.0$ GeV^2 were used in similar fits, the values of χ^2/N_D were in general smaller, but only ω_A and ω_W could provide adequate fits to all three sets of data. As no random error from the error in R was included in the errors in the structure function νW_2, a χ^2/N_D of 1.3 is judged a "good" fit and χ^2/N_D of 1.5 is judged an "adequate" fit.

Polynomial fits in ω_A, wherein only the fourth and fifth powers of $(1 - 1/\omega_A)$ were used to fit the structure-function data, were also attempted. These fits are identical to those attempted by Atwood[76] for the recent data for $2MW_1$. Results of such fits are presented in Table XIX, where we list M_A^2 and the polynomial coefficients a_4 and a_5, together with the χ^2/N_D of the fits. Such fits to the νW_2^d data are clearly inadequate, but when νW_2^p and νW_2^n are separated and fit independently, adequate fits are obtained. However, the best-fit values of M_A^2 for the proton and neutron are significantly different. Similar results[76] were recently obtained for $2MW_1$. When the fit data are restricted to $W \geq 2.6$ GeV, the best-fit values of M_A^2 change to 1.642 ± 0.048 GeV^2 for the proton and 0.861 ± 0.017 GeV^2 for the neutron. For comparison the value of M_A^2 obtained by Atwood *et al.* in a fit to $2MW_1$ is $M_A^2 = 1.473 \pm 0.042$ GeV^2 for the proton.[76] Our results for νW_2 agree with the results of Atwood *et al.* for $2MW_1$ in that the neutron structure functions appear to scale in ω', while the proton structure functions scale in $\omega_A = \omega + M_A^2/Q^2$ with M_A^2 about equal to 1.5 GeV^2. Adequate two-parameter polynomial fits, for j values of 4 and 5, can be made to both νW_2^p and νW_2^n using such a scaling variable, but this requires M_A^2 to be *different* for the proton and neutron.

D. Deviations from scaling in ω or ω'

Rather than search for new scaling variables that can fit all the data for νW_2, one can parametrize the deviations from scaling in a preselected variable, as was done for the F_1 and F_2 in Sec. VII A. In the same vein, we have made fits of the form $\nu W_2(\nu, Q^2) = f(\xi)h(Q^2)$ to the data for νW_2^p, νW_2^d, and νW_2^n shown in Figs. 38 and 39. As in Sec. VII A, $f(\xi)$ is a five-parameter polynomial in $\xi = \omega$ or $\xi = \omega'$, and $h(Q^2)$ is either the linear scale-breaking form $1 - 2Q^2/\Lambda^2$ or the propagator form $(1 + Q^2/\Lambda^2)^{-2}$. Best-fit values of $1/\Lambda^2$ and the polynomial coefficients were obtained simultaneously by least-squares fits. The results for Λ^2 were independent of the functional form chosen for $f(\xi)$. Although the scale-breaking forms studied cannot vary with ω or ω', this factorization method has the distinct advantage of being a parametrization with greater statistical precision. The same data for νW_2 (with $Q^2 \geq 2$ GeV^2 and $W \geq 2$ GeV) as was used in the previous section are used here, and the following results can be compared directly with those in Tables XVIII and XIX.

For fits in the variable $\xi = \omega$, both linear and propagator scale-breaking forms provide much better fits to νW_2^p and νW_2^d than functions that scale in ω. But the χ^2 for these scale-breaking fits, which ranged from 1.90 to 2.28 per degree of freedom, indicate that the full body of νW_2^p and νW_2^d data cannot be parameterized by either functional form. However, both linear and propagator forms provide good fits to the full body of νW_2^n data, achieving χ^2 of 1.28 and 1.30 per degree of freedom.

The χ^2 for these scale-breaking fits improved markedly when the structure-function data were restricted to $W \geq 2.6$ GeV. The χ^2 per degree of freedom ranged from 1.31 to 1.36 for fits to νW_2^p and νW_2^n, while it ranged from 1.60 to 1.71 for fits to νW_2^d. Best-fit parameters of these fits are

TABLE XIX. Fits in the scaling variable ω_A.

Fit data	N_D	χ^2/N_D	M_A^2 (GeV^2)	a_4	a_5
νW_2^p	276	1.55	1.512 ±0.019	3.371 ±0.022	−3.218 ±0.029
νW_2^d	259	2.33	1.469 ±0.017	4.842 ±0.031	−4.308 ±0.040
νW_2^n	259	1.41	0.792 ±0.048	1.866 ±0.038	−1.561 ±0.049

TABLE XX. Scale-breaking fits to $\nu W_2 = f(\omega)h(Q^2)$ for ($W \geq 2.6$ GeV, $Q^2 \geq 2.0$ GeV^2).

Data	N_D	$h(Q^2)=1-2Q^2/\Lambda^2$ Λ^{-2} (GeV^{-2})	χ^2/N_D	$h(Q^2)=(1+Q^2/\Lambda^2)^{-2}$ Λ^{-2} (GeV^{-2})	χ^2/N_D
νW_2^p	193	0.0092 ±0.0004	1.33	0.0122 ±0.0007	1.36
νW_2^d	183	0.0100 ±0.0003	1.60	0.0133 ±0.0006	1.71
νW_2^n	183	0.0110 ±0.0010	1.31	0.0143 ±0.0018	1.34

presented in Table XX with quoted errors that include both random errors and systematic uncertainties, added in quadrature. These uncertainties arose from uncertainties in R and the measured differential cross sections that were propagated through the extracted values of νW_2 used in these fits.

The linear and propagator scale-breaking forms fit both the νW_2^p and the νW_2^n data equally well. In both cases, the coefficient $1/\Lambda^2$ is less than 2 standard deviations larger for the neutron than for the proton. The relatively poor χ^2 obtained for νW_2^d probably reflects the fact that its Q^2 dependence is a composite of proton and neutron behaviors (and smearing).

Best-fit parameters of scale-breaking fits in the variable $\xi = \omega'$ are presented in Table XXI, along with χ^2/N_D for these fits. The quoted errors are again the quadratic sum of random errors and systematic uncertainties. For both cases of $W \geq 2.0$ and $W \geq 2.6$ GeV the χ^2 for these fits is better than the χ^2 of the ω-scale-breaking fits represented in Table XX. Adequate fits were obtained even for the deuteron data. For $W \geq 2$ GeV, the values of $1/\Lambda^2$ for both linear and propagator scale-breaking fits are, for the proton, within 1 standard deviation of the corresponding values of $1/\Lambda_2^2$ reported in Table XVII. The extracted quantities νW_2^p, νW_2^d, and νW_2^n clearly do not scale in ω'. Even when the kinematic range for the fits is limited to $W \geq 2.6$ GeV, the coefficients $1/\Lambda^2$ are not consistent with zero. No significant conclusions can be made about the relative degrees of scale breaking of the present data for νW_2^p and νW_2^n other than that the breaking is similar for both.

In conclusion, we have made fits of the form $\nu W_2 = f(\xi)h(Q^2)$ to the νW_2^p and νW_2^n data using both scaling variables $\xi = \omega$ and $\xi = \omega'$. Both linear and propagator scale-breaking forms allow good fits to these data. In the case of $\xi = \omega$, the proton data must be restricted to $W \geq 2.6$ GeV in order to obtain a good fit. Adequate fits to νW_2^d can be obtained only for $\xi = \omega'$. Statistically significant scaling violations are observed for fits in either scaling variable to νW_2^p, νW_2^d, and νW_2^n. Over the range of Q^2 included in these tests ($2.0 \leq Q^2 \leq 20.0$ GeV^2), we observe 33–40% deviations from scaling in ω and 14–22% deviations from scaling in ω'. No conclusive evidence can be found for different scaling deviations for the neutron and proton. Scale-breaking fits in the variable $\xi = \omega'$ provide better fits to the proton data than fits with exact scaling in ω_A.

E. Quantum chromodynamics

The strong evidence for scale breaking that we observe in deep-inelastic electron scattering is now seen as well in deep-inelastic muon scattering[81-84] and also in deep-inelastic neutrino scatter-

TABLE XXI. Scale-breaking fits to $\nu W_2 = f(\omega')h(Q^2)$.

Data	N_D	$h(Q^2)=1-2Q^2/\Lambda^2$ Λ^{-2} (GeV^{-2})	χ^2/N_D	$h(Q^2)=(1+Q^2/\Lambda^2)^{-2}$ Λ^{-2} (GeV^{-2})	χ^2/N_D
		(a) $W \geq 2.0$ GeV			
νW_2^p	273	0.0053 ±0.0003	1.30	0.0060 ±0.0004	1.32
νW_2^d	256	0.0048 ±0.0002	1.42	0.0055 ±0.0003	1.44
νW_2^n	256	0.0038 ±0.0009	1.26	0.0042 ±0.0011	1.26
		(b) $W \geq 2.6$ GeV			
νW_2^p	193	0.0052 ±0.0005	1.28	0.0061 ±0.0007	1.28
νW_2^d	183	0.0058 ±0.0004	1.45	0.0067 ±0.0006	1.48
νW_2^n	183	0.0062 ±0.0012	1.28	0.0069 ±0.0017	1.28

ing.[85,86] The muon measurements span a far greater range in Q^2 than ours: well beyond a value of 100 GeV/c^2 as compared to our maximum value of about 20 (GeV/c)^2. Quantum chromodynamics (QCD) can provide an explanation for scale breaking in deep-inelastic lepton-hadron scattering. Because of the particular form of scale breaking predicted from QCD, definitive tests of this model can only be carried out over a much greater range of Q^2 than is reported here. Preliminary data from the present experiment, which are totally consistent with our final cross sections, have been combined with higher-Q^2 results from muon scattering experiments for such comparisons.[82-84] It has been found that QCD gives a good account of scale breaking in ep and μp scattering and also νp and $\bar{\nu} p$ scattering.[86,87]

VIII. SUMMARY AND CONCLUSIONS

We have carried out an experimental study of the neutron and proton deep-inelastic electromagnetic structure functions. The structure functions were extracted from electron-proton and electron-deuteron differential cross sections measured with the SLAC 8-GeV spectrometer in two experiments at laboratory angles of 15°, 18°, 19°, 26°, and 34°, and from data from a prior experiment at 6° and 10° carried out with the 20-GeV spectrometer. We report here on the large-angle (15°–34°) measurements and data analysis.

The experiments using hydrogen targets at the larger angles repeat earlier measurements but with improved statistical accuracy and expanded kinematic range. These measurements were supplemented by matched measurements using deuterium targets. Neutron cross sections were extracted from the deuteron data using an impulse approximation and the measured proton cross sections. Corrections were made for the Fermi motion of the bound nucleons. We were thus able to make a detailed comparison of the inelastic electron-proton and electron-neutron scattering cross sections. The program of measurements allowed more stringent tests of structure-function scaling than earlier measurements. One of the primary objectives of the measurements was the determination of the ratio of neutron to proton cross sections because the measured ratio puts constraints both on parton, and on other, models of nucleon structure.

An additional objective of the experiment was a detailed examination of the angular dependences of the cross sections so as to determine the kinematic variations of R_p and R_d for fixed x, the ratios of the longitudinal to transverse cross sections. The behavior of $R(Q^2)$ for fixed x reflects the spin quantum numbers of those charged partons carrying a fraction x of the nucleon's momentum.

These measurements, covering an extended range of Q^2, confirm that scaling is only an approximate behavior of the structure functions. A study of fits to the data with scale-breaking forms has been made. Over the range of Q^2 of the data, 1.0 to 20.0 GeV^2, we observe deviations from scaling in the scaling variable ω' in the range of 14 to 22%. Deviations in the Bjorken variable ω, for ω in the range 1.3 to 10.0, are as large as 40%, confirming the trend of earlier results. A number of theories, including asymptotic field theories, predict small deviations from scaling aside from the low-Q^2 turn-on of νW_2 scaling. The kinematic range of these data alone is not sufficient to allow us to make a choice among the various models.

The results indicate that the ratio of the neutron to proton inelastic cross sections falls continuously as the scaling variable x approaches 1. The experimental ratio falls to about 0.3 in the neighborhood of $x = 0.85$ and hence is still above the lower limit of 0.25 imposed by the quark-parton model.

From a comparison of the experimental results for R_p and R_d, we find that within experimental errors $R_d = R_p = R_n$ and that their values over the kinematic range are consistent with spin-$\frac{1}{2}$ constituents of the nucleon.

We conclude that the combined results of these experiments are consistent with the predictions of the quark-parton model of the structure of the nucleon over an extended kinematic range, confirming the interpretation of earlier results.

ACKNOWLEDGMENTS

We wish to express our gratitude and appreciation to all members of the Stanford Linear Accelerator Center. We thank Professor W. K. H. Panofsky and the Technical Division under Dr. R. B. Neal for their support in this experiment. Technical support from the Spectrometer Facilities Group, particularly E. Taylor and Dr. C. K. Sinclair. is much appreciated.

We thank Dr. J. R. Johnson and Dr. R. L. Anderson for their help in the setup of the 1.6-GeV spectrometer. The help of K. Stone and Dr. K. Tsipis in the running of the experiment is much appreciated.

We are indebted to the members of SLAC Group A, particularly Dr. E. D. Bloom, Dr. R. L. A. Cottrell, Dr. H. DeStaebler, Dr. C. L. Jordan, Dr. H. Piel, and Dr. R. E. Taylor for use of the 6° and 10° data and for valuable discussions.

Special thanks goes to W. B. Atwood for making available his resonance-fitting procedure and for numerous valuable discussions about deuteron

binding effects.

We thank E. Miller and Dr. R. Verdier for programming assistance. Discussions with Dr. G. Miller and help from M. Mestayer and Dr. Steve Stein of Group A are appreciated. We are indebted to Dr. R. L. Jaffe for illuminating discussions about the interpretation of the σ_L/σ_T measurements.

We are grateful to the M.I.T. Physics Department and Laboratory for Nuclear Science for their support of the M.I.T. collaborators.

This work was supported in part by the Department of Energy under Contract Nos. EY-76-C-02-3069 and EY-76-C-03-0515.

APPENDIX A: ACCEPTANCE OF THE 8-GeV SPECTROMETER

The solid-angle acceptance of the 8-GeV spectrometer was calculated in two primary steps that utilized the SLAC beam-transport program TRANSPORT[88] and a Monte Carlo ray-tracing program initiated by Jordan.[89] Prior to these calculations, a computer model of the spectrometer was formulated; it incorporated ideal dipole and quadrupole magnet elements as well as drift spaces and apertures. The program TRANSPORT used this model to generate matrices of transport coefficients that describe the passage of charged particles through the spectrometer magnet array. The transport coefficients are first- and second-order coefficients in a Taylor-series expansion of the particle coordinates $(x, \theta, y, \phi, z, \delta = \Delta P/P)$ about the spectrometer central ray. In the second step the matrices of transport coefficients were used in the Monte Carlo program to calculate the acceptance of the individual segments of the spectrometer focal planes.

The TRANSPORT model of the 8-GeV spectrometer, the same for all momenta, is listed in Table XXII for $P = 8.0051$ GeV. Negative quadrupole fields indicate vertical focusing; ψ is the pole-face rotation of the bending magnets relative to the central ray. Similar models, with only the magnet field strengths altered, were used at $P = 3.0062$, 6.0091, and 0.0026 GeV, where optics data on the 8-GeV spectrometer were available.[90] Table XXIII lists the magnet field strengths used at these momenta; the numbers in parentheses represent the percentage deviation from the measured field strengths,[90] assuming linearity. The reason for the deviations in the quadrupole strengths is discussed in the following paragraph.

The principal first-order transport coefficients measured in the optics tests are listed in Table XXIV; their estimated accuracy is 1%.[90] When the measured magnet field strengths were used in the above TRANSPORT model, we could not reproduce these measured coefficients. We felt that these discrepancies were caused by the proximity of the magnets to the steel boom of the spectrometer and to each other, resulting in distortion of

TABLE XXII. TRANSPORT model of the 8-GeV spectrometer: $P = 8.0051$ GeV.

1.	Drift from target: 2.295 m
2.	Quadrupole Q81 ($z = 1.034$ m, $a = 13.97$ cm, 7.488 kG)
3.	Drift: 0.352 m
4.	Aperture No. 1 [circle: $(x^2 + (y + 0.24)^2)^{1/2} < 13.02$ cm]
5.	Drift: 0.614 m
6.	Quadrupole Q82 ($z = 1.334$ m, $a = 19.37$ cm, -10.827 kG)
7.	Drift: 0.962 m
8.	$\frac{1}{2}$ of dipole B81 ($z = 1.8135$ m, $\psi = 7.5°$, 19.274 kG, $n = 0$)
9.	Aperture (-19.21 cm $< y <$ 34.47 cm)
10.	$\frac{1}{2}$ of dipole B81 ($z = 1.8135$ m, $\psi = 7.5°$, 19.274 kG, $n = 0$)
11.	Drift: 0.3863 m
12.	Swing mask (normally out)
13.	Drift: 0.5387 m
14.	Dipole B82 ($z = 3.627$ m, $\psi = 7.5°$, 19.274 kG, $n = 0$)
15.	Drift: 0.762 m
16.	Aperture No. 2 [octagon: $\lvert y \rvert < 16.5$ cm, $\lvert x \rvert < 14.5$ cm, and $\lvert y \rvert <$ (24.6 cm)$(1 - \lvert x \rvert/(18.2$ cm))]
17.	Drift: 0.243 m
18.	Quadrupole Q83 ($z = 1.334$ m, $a = 19.37$ cm, -7.332 kG)
19.	Drift: 4.198 m
20.	θ focal plane
21.	Drift: 0.555 m
22.	Momentum focal plane

Total path length $z_{tot} = 21.861$ m

TABLE XXIII. Magnet-field strengths used in TRANSPORT. Units are kG. Quadrupole fields are given at pole tip.

Magnet \ P (GeV)	3.0062	6.0091	8.0051	9.0026
$Q81$	2.788 (−2.1)	5.620 (−1.3)	7.488 (−1.3)	8.365 (−2.0)
$Q82$	−4.013 (2.0)	−8.116 (0.8)	−10.827 (0.6)	−11.986 (2.0)
$B81$	7.238 (0.0)	14.468 (0.0)	19.274 (0.0)	21.675 (0.0)
$B82$	7.238 (0.0)	14.468 (0.0)	19.274 (0.0)	21.675 (0.0)
$Q83$	−2.703 (−0.7)	−5.442 (−1.4)	−7.332 (−2.4)	−8.428 (−4.7)

their fringing fields.[90] In addition, the field strengths and effective magnet lengths were not known better than 1%. Consequently, we made an extensive study of TRANSPORT models, in which several of the available parameters (e.g., field strengths and pole-face rotations) were varied in different combinations until a selected set of transport coefficients agreed with the measured values. We hoped we could simulate the nonideal behavior and better approximate the measured transport coefficients with such an adjusted TRANSPORT model. The final TRANSPORT model chosen had varied the three quadrupole field strengths so that $\langle x|x_0\rangle$, $\langle x|\theta_0\rangle$, and $\langle y|\delta_0\rangle$ (where the subscript 0 denotes values at the target) reproduced the measured values. The best-fit values of the quadrupole field strengths are those listed in Table XXIII.

The criterion for an acceptable TRANSPORT model was that it reproduce solid-angle maps measured in the optics tests. Solid-angle maps were generated from each model using a ray-tracing program developed by Taylor[91]; they were then compared with the measured maps. All TRANSPORT models examined were capable of reproducing some subset of the measured transport coefficients; these were usually chosen to include the two dispersions $\langle x|\theta_0\rangle$ and $\langle y|\delta_0\rangle$, as they directly influence the acceptance. But the various models predicted fairly different results for the solid-angle maps and could be distinguished by this criterion. Comparisons of solid-angle maps were attempted only at $P=8$ GeV; the choice of TRANSPORT model was assumed independent of momentum. We ascertained that the model that best approximated the measured solid-angle maps was the model used in all previous calculations[41,92] of the 8-GeV acceptance: the field strengths of $Q81$, $Q82$, and $Q83$ were varied independently to fit the transport coefficients $\langle x|x_0\rangle$, $\langle x|\theta_0\rangle$, and $\langle y|\delta_0\rangle$. Table XXV lists the principal first-order transport coefficients as obtained using this canonical TRANSPORT model at $P=3.0$, 6.0, 8.0, and 9.0 GeV; these coefficients should be compared with the measured values from Table XXIV.

A Monte Carlo program used matrices of transport coefficients to calculate the solid-angle acceptance $\Delta\theta\Delta\phi\Delta P/P$ of the 8-GeV spectrometer. Acceptances are calculated for each p-θ bin, defined as the intersection of two adjacent θ counters and two adjacent P counters in the spectrometer focal planes; these acceptances were then summed to get the total acceptance. Scattered rays $(x_0, \theta_0, y_0, \phi_0, z_0, \delta_0)$ were generated randomly at the target position; for large N, they were distributed uniformly over a segment $\Delta\theta_0\Delta\phi_0\Delta\delta_0$ that completely overlapped the spectrometer acceptance. The initial volume $\Delta x_0\Delta y_0\Delta z_0$ reflected the target length and beam spot size. The rays were propagated through five successive segments of the spectrometer according to the transport coefficients for that segment. Each ray was re-

TABLE XXIV. Measured transport coefficients. Lengths are in cm; angles in mrad; δ in percent.

Coefficient \ P (GeV)	3.0062	6.0091	8.0051	9.0026
$\langle x\|x_0\rangle$	0.0385	0.0206	0.0277	0.0153
$\langle x\|\theta_0\rangle$	4.5170	4.5468	4.5750	4.5902
$\langle\theta\|x_0\rangle$	−0.1868	−0.2157	−0.1936	−0.2043
$\langle\theta\|\theta_0\rangle$	4.7907	4.8245	4.8576	4.8805
$\langle y\|\phi_0\rangle$	0.0007	−0.0014	−0.0041	−0.0047
$\langle y\|\delta_0\rangle$	−2.9591	−2.9389	−2.9067	−2.8439
$\langle\phi\|\phi_0\rangle$	−1.0740	−1.0757	−1.0769	−1.0787
$\langle\phi\|\delta_0\rangle$	0.0789	0.0857	0.0935	0.1130

TABLE XXV. Transport coefficients from the TRANSPORT model. Lengths are in cm; angles in mrad; δ in percent.

Coefficient \ P (GeV)	3.0062	6.0091	8.0051	9.0026
$\langle x\|x_0\rangle$ [a]	0.0385	0.0206	0.0277	0.0153
$\langle x\|\theta_0\rangle$ [a]	4.5170	4.5468	4.5750	4.5902
$\langle\theta\|x_0\rangle$	−0.1805	−0.1980	−0.1889	−0.2014
$\langle\theta\|\theta_0\rangle$	4.8004	4.8449	4.8942	4.9459
$\langle y\|\phi_0\rangle$	0.0066	−0.0064	−0.0139	−0.0139
$\langle y\|\delta_0\rangle$ [a]	−2.9591	−2.9389	−2.9067	−2.8439
$\langle\phi\|\phi_0\rangle$	−1.0900	−1.0830	−1.0921	−1.1375
$\langle\phi\|\delta_0\rangle$	0.1106	0.1479	0.2074	0.3230

[a] The values for this coefficient are equal to the measured values by definition.

quired to clear 13 different apertures within the spectrometer or was rejected. Actually, only two lead apertures, one behind $Q81$ and the other behind $B82$, determined the solid-angle acceptance. For each P-θ bin, $\Delta\delta$ and $\Delta\theta$ were determined soley by the edges of the counters themselves; $\Delta\delta$ and $\Delta\theta$ were therefore directly related to the measured dispersions $\langle x|\theta_0\rangle$ and $\langle y|\delta_0\rangle$. The $\Delta\phi$ for each p-θ bin was determined by the lead apertures behind $Q81$ and $B82$. The acceptance $(\Delta\theta\Delta\phi\Delta\delta)_{ij}$ of the i-jth P-θ bin was taken to be taken to be

$$(\Delta\theta\Delta\phi\Delta\delta)_{ij} = \frac{N_{ij}}{N}(\Delta\theta_0\Delta\phi_0\Delta\delta_0), \qquad \text{(A1)}$$

where N_{ij} is the number of events falling into this bin and N is the total number of Monte Carlo events.

Three-dimensional computer models of the P and θ hodoscopes permitted a more accurate calculation of acceptances. Each hodoscope was modelled by two parallel, segmented planes that represented the two rows of scintillation counters. Monte Carlo events were binned at each focal plane according to the segments (read counters) of the two planes through which the event passed. In this way "shadowing" effects, which arose from the nonzero divergence and convergence of scattered rays at the focal planes, were adequately simulated. This more faithful representation of the hodoscopes allowed a much more accurate calculation of the acceptances of each P-θ bin. These shadowing effects were quite severe (~20%) for a single bin. Errors of about 1% in the total acceptance resulted if one did not account for these effects. Consequently, this three-dimensional computer model of the hodoscopes is felt to be the primary advantage of the present acceptance calculation.

Monte Carlo acceptance calculations were made at $P = 3.0$, 6.0, 8.0, and 9.0 GeV using the TRANSPORT model of Table XXII with the appropriate magnet field strengths from Table XXIII. Samples of 4×10^5 Monte Carlo events were used, ensuring that 100–500 events fell into each of the 20×54 P-θ bins. The acceptances of the individual bins were somewhat inaccurate statistically, but the total acceptance was well known. The results of these calculations are shown in Table XXVI for two definitions of the spectrometer acceptance. A_2 is the nominal acceptance definition used in the present experiment; it includes only P bins 2–19 and θ bins 2–53. The optics measurements at 3 GeV were somewhat in doubt due to the effects of multiple scattering,[90] and we felt that saturation might be setting in at 9 GeV. Consequently the acceptance for the present experiment was taken to be the average of the 6- and 8-GeV calculations. Δ is the percentage difference of A_2 from the average value. No significance is attached to the P dependence of the acceptance evident in Table XXVI. Calculations with a different TRANSPORT model, which simulated the solid-angle maps almost as well, showed a markedly different momentum dependence. We only conclude that the possible error due to momentum dependence of the acceptance is about ± 0.5%.

Tests of the solid-angle acceptance of the 8-GeV spectrometer were made using the tungsten slits in front of the spectrometer entrance window, before the first quadrupole magnet $Q81$. The verti-

TABLE XXVI. Acceptance of the 8-GeV spectrometer.

P (GeV)	A_1 (10^{-3} msr)	A_2 (10^{-3} msr)	Δ (%)
3.0062	27.01	24.69	−0.92
6.0091	27.37	24.89	−0.12
8.0051	27.32	24.95	+0.12
9.0026	26.76	24.69	−0.92
Average	27.35	24.92	

cally opening ϕ slits can determine $\Delta\phi_{ji}$ independent of the apertures within the spectrometer. As $\Delta\theta_{ji}$ and $\Delta\delta_{ji}$ were already well known from the optics measurements, the ϕ slits allowed an accurate check of the TRANSPORT model calculations. The solid-angle acceptance was calculated by the Monte Carlo program for six different settings of the ϕ slits ranging from fully open to $\Delta\phi = 13$ mrad, where $\Delta\phi_{ij}$ was almost completely determined by the tungsten slits. Experimental runs of $\sim 10^4$ counts at each of these slit settings revealed that (yield/acceptance) was constant within 1%. It was important to correct for $\Delta\phi$ shifts in the effective scattering angle in these calculations, as this effect was about 1% itself. Based upon the results of this solid-angle test and on the quoted 1% accuracy[90] of the optics measurements, we conclude that the acceptance of the 8-GeV spectrometer is accurate to 1.5% and the momentum dependence accurate to $\pm 0.5\%$.

APPENDIX B: RADIATIVE-CORRECTION FORMULAS

We give here the formulas used to correct radiatively the elastic and inelastic cross sections. Discussion of these equations and their application to the data may be found in Sec. VI.

The radiative tail $I_1(E_0, E', \theta, t)$ from elastic e-p scattering was determined from an expression derived by Friedman.[93]

$$I_1(E_0, E', \theta, t) = I_1^B + I_1^A, \tag{B.1}$$

where

$$I_1^B = [1 + 0.58b(l_A + l_B)]\left[\left(\ln\frac{E_{0f}}{E'}\right)^{bl_A}\left(\ln\frac{E_0}{E_c}\right)^{bl_B}\left(\frac{bt_A R_A}{E_{0f} - E'}\sigma(E_0) + v'X(E_0, E', \theta)\frac{P_A}{P_A + P_B}\right)aC_A\right],$$

$$I_1^A = [1 + 0.58b(l_A + l_B)]\left[\left(\ln\frac{E_0}{E_0'}\right)^{bl_B}\left(\ln\frac{E_c'}{E'}\right)^{bl_A}\left(\frac{bt_B R_B}{E_0 - E_0'}\frac{\sigma(E_0')}{[1 - (2E'/M)\sin^2\theta/2]^2}\right.\right.$$
$$\left.\left. + v'X(E_0, E', \theta)\frac{P_B}{P_A + P_B}\right)\beta C_B\right],$$

$$v' = 1 + (v_A + v_B)(\tfrac{1}{2} + \tfrac{1}{2}\ln\eta), \quad P_A = S_A\sigma(E_0)/(E_{0f} - E'), \quad P_B = S_B\sigma(E_0')/\left[(E_0 - E_0')\left(1 - \frac{2E'}{M}\sin^2\frac{\theta}{2}\right)^2\right],$$

$$S_A = \left[\frac{E'}{E_{0f}} + \frac{1}{2}\left(\frac{E_{0f} - E'}{E_{0f}}\right)^2\right], \quad S_B = \left[\frac{E_0'}{E_0} + \frac{1}{2}\left(\frac{E_0 - E_0'}{E_0}\right)^2\right],$$

$$R_A = \left[\frac{E'}{E_{0f}} + \frac{3}{4}\left(\frac{E_{0f} - E'}{E_{0f}}\right)^2\right], \quad R_B = \left[\frac{E_0'}{E_0} + \frac{3}{4}\left(\frac{E_0 - E_0'}{E_0}\right)^2\right],$$

$$a = \frac{1}{(\ln E_0/E_c)^{bl_B}}\left[\left(\ln\frac{E_0}{E_0 - 0.10k}\right)^{bl_B} + bl_B\left(\ln\frac{E_0}{E_0 - 0.20k}\right)^{bl_B}\frac{\sigma(E_0 - 0.20k)}{\sigma(E_0)}\right.$$
$$\left. + \frac{2}{3}bl_B\left(\ln\frac{E_0}{E_0 - 0.45k}\right)^{bl_B}\frac{\sigma(E_0 - 0.45k)}{\sigma(E_0)} + \frac{1}{2}bl_B\left(\ln\frac{E_0}{E_0 - 0.80k}\right)^{bl_B}\frac{\sigma(E_0 - 0.80k)}{\sigma(E_0)}\right],$$

$$k = E_0 - E_c = \frac{E_0 - E_0'}{2},$$

$$\beta = \frac{1}{(\ln E_c'/E')^{bl_A}}\left[\left(\ln\frac{E' + 0.10\rho}{E'}\right)^{bl_A} + bl_A\left(\ln\frac{E' + 0.20\rho}{E'}\right)^{bl_A}\frac{\sigma(E_0' + 0.20k)}{\sigma(E_0')}\right.$$
$$\left. + \frac{2}{3}bl_A\left(\ln\frac{E' + 0.45\rho}{E'}\right)^{bl_A}\frac{(E_0' + 0.45k)}{\sigma(E_0')} + \frac{1}{2}bl_A\left(\ln\frac{E' + 0.80\rho}{E'}\right)^{bl_A}\frac{\sigma(E_0' + 0.80k)}{\sigma(E_0')}\right],$$

$$\rho = E_c' - E', \quad k + E_c - E_0' = (E_0 - E_0')/2, \quad E_c = (E_0 + E_0')/2,$$

$$C_A(l_A, E', E_{0f}) = \left\{1 + bl_A\left[-0.733\,229 + 1.0783\left(\frac{E'}{E_{0f}}\right) + 0.349\,814\left(\frac{E'}{E_{0f}}\right)^2 - 0.636\,089\left(\frac{E'}{E_{0f}}\right)^3\right]\right\}$$
$$\times\left(\frac{1.045(0.99 - E'/E_{0f})}{0.89} + \frac{0.962(E'/E_{0f} - 0.010)}{0.89}\right),$$

$$C_B(l_B, E_0', E_0) = C_A(l_B, E_0', E_0).$$

C_A and C_B were empirical corrections[94] for approximations made in the solution of the diffusion equation for the straggling functions. $X(E_0, E', \theta)$ is the exact tail from internal-bremsstrahlung calculated to lowest order in α according to Mo and Tsai.[43,44]

$$l_A = t_A + v_A/b\,,$$

$$l_B = t_B + v_B/b\,.$$

t_B and t_A are the radiation lengths before and after scattering discussed in Sec. VI B.

$$v_A = v_B = \frac{\alpha}{\pi}\left(\ln\frac{q^2}{m^2} - 1\right),$$

$$b = \tfrac{4}{3}\,,$$

m = the electron mass,

$$E_{0f} = E_0 \Big/ \left[1 + \frac{2E_0}{M}\sin^2\left(\frac{\theta}{2}\right)\right],$$

$$E_0' = E' \Big/ \left[1 - \frac{2E'}{M}\sin^2\left(\frac{\theta}{2}\right)\right],$$

$$E_c = E_c \Big/ \left[1 + \frac{2E_c}{M}\sin^2\left(\frac{\theta}{2}\right)\right].$$

$\sigma(E_0)$ is the elastic-scattering cross section calculated according to the Rosenbluth equation,[95]

$$\sigma(E_0,\theta) = \frac{\alpha^2}{4{E_0}^2}\left(\frac{\cos^2\theta/2}{\sin^4\theta/4}\right)\left(\frac{1}{1+(2E_0/M)\sin^2\theta/2}\right) \times \left(\frac{{G_E}^2 + \tau {G_M}^2}{1+\tau} + 2\tau {G_M}^2 \tan^2\frac{\theta}{2}\right),$$

where

$$\tau = Q^2/4M^2\,,$$

$$G_E = \frac{1}{\mu_p}\,G_M = f_M(Q)(1+Q^2/0.71)^{-2}\,.$$

The function $f_M(Q)$ is a modulating factor that varies about the value of 1.0. It is from a fit by Miller[41] to all previous SLAC elastic e-p data.[29,40]

$$f_M(Q) = \sum_{i=0}^{i=5} a_i \prod_{\substack{j=0 \\ j\neq i}}^{j=5} \frac{Q - Q_j}{Q_i - Q_j}\,, \tag{B2}$$

where $Q = (Q^2)^{1/2}$, and the coefficients a_i are equal to the value of the function $f(Q)$ at $Q = Q_i$,

$$a_0 = 1.000\,,$$

$$a_1 = 1.018\,,$$

$$a_2 = 1.056\,,$$

$$a_3 = 0.836\,,$$

$$a_4 = 0.687\,,$$

$$a_5 = 0.673\,.$$

The quasielastic and elastic tails calculated in the equivalent-radiator (ER) approach were from an expression derived by Sogard.[96] They were calculated for proton, neutron, and deuteron [see Eq. (6.4)] according to

$$\begin{aligned} I_1^{\mathrm{ER}}(E_0,E',\theta,t) = {} & \frac{(1+a)^{b(l_A+l_B)}}{\Gamma(1+bl_A)\Gamma(1+bl_B)}\exp\{-b[l_B\ln(E_0/\Delta)+l_A\ln(E'/\Delta)]\}\frac{d^2\sigma}{d\Omega dE'}(E_0,E',\theta)_{\mathrm{TH}} \\ & + \frac{(1+a)^{bl_A}}{\Gamma(1+bl_A)}\exp[-bl_A\ln(E'/\Delta)]\int_{E_{0_{\min}}}^{E_0-\Delta} dE_0'\,\frac{d^2\sigma}{d\Omega dE'}(E_0',E',\theta)_{\mathrm{TH}} I_e(E_0,E_0',l_B) \\ & + \frac{(1+a)^{bl_B}}{\Gamma(1+bl_B)}\exp[-bl_B\ln(E_0/\Delta)]\int_{E'+\Delta}^{E'_{\max}(E_0')} dE''\,\frac{d^2\sigma}{d\Omega dE''}(E_0,E'',\theta)_{\mathrm{TH}} I_e(E'',E',l_A) \\ & + \int_{E_{0_{\min}}}^{E_0-\Delta} dE' \int_{E'+\Delta}^{E'_{\max}(E_0')} dE''\, I_e(E_0,E_0',l_B)\frac{d^2\sigma}{d\Omega dE''}(E_0',E'',\theta)_{\mathrm{TH}} I_e(E'',E',l_A)\,, \end{aligned} \tag{B3}$$

where

$$I_e(E_0,E',t) = \frac{(1+a)^{bt}}{E_0}\left(\frac{E'}{E_0}\right)^a\left[\frac{[\ln(E_0/E')]^{bt-1}}{\Gamma(bt)}\right]$$

is the Eyges[97] straggling function for which a and b are functions of E'/E_0 found by fitting the bremsstrahlung cross section for this straggling function to the bremsstrahlung cross section according to Bethe and Ashkin.[98]

$$\Delta = 0.001\,E_0/[1+(2E_0/M)\sin^2(\tfrac{1}{2}\theta)]\,.$$

$E'_{0_{\min}}$ and $E'_{\max}(E_0')$ are the minimum E_0' and maximum E'' kinematically permitted. l_A and l_B were defined previously. $(d^2\sigma/d\Omega dE')(E_0,E',\theta)_{\mathrm{TH}}$ is the cross section for quasielastic e-d scattering or is replaced by the elastic e-p or e-n scattering cross sections for the calculation of the elastic e-p and e-n radiative tails. Cross sections for quasielastic e-d scattering were from the method of Durand[52] using S- and D-state Hamada-Johnston wave functions.[48] The elastic cross sections were obtained from the Rosenbluth equation, assuming form-factor scaling.

The expression used in the inelastic radiative

corrections is

$$\frac{d^2\sigma}{d\Omega dE'}(E_0,E',\theta)=C\left[\frac{d^2\sigma}{d\Omega dE'}(E_0,E',\theta)_M-I_2^B-I_2^A\right],$$

where $(d^2\sigma/d\Omega dE')(E,E',\theta)_M$ is the experimentally measured cross section after subtraction of elastic and quasielastic radiative tails, $(d^2\sigma/d\Omega dE')$ is the radiatively corrected cross section,

$$C=[1-(0.58+a)(t_A+t_B)b]\exp(\delta_T+\delta_R)], \tag{B4}$$

$$\delta_T=bt_A\ln(E'/\Delta E')+bt_B\ln(E_0/\Delta E_0),$$

$$\delta_R=\frac{\alpha}{\pi}\left\{\tfrac{28}{9}-\tfrac{13}{6}\ln(q^2/m^2)+[\ln(q^2/m^2)-1][\ln(E_0/\Delta E_0)+\ln(E'/\Delta E')]\right\},$$

$\Delta E_0=\frac{1}{2}$ a bin width in E_0,

$\Delta E'=\frac{1}{2}$ a bin width in E',

$m=$ electron mass,

$a=0.25$

and I_2^B and I_2^A are integrals over the previously corrected data:

$$I_2^B=(1+0.58bL)(\Delta/E_0)^{bl_B}[1+(1-\Delta/E_0)abl_B]\times\int_{E'+\Delta E'}^{E'_{\max}}dE_{0f}[\ln(E_{0f}/E')]^{bl_A}(E_{0f}-E')^{-1}(bt_AR_A+v_Av'S_A)\frac{d^2\sigma}{d\Omega dE'}(E_0,E_{0f},\theta), \tag{B5}$$

$$I_2^A=(1+0.58bL)(\Delta'/E')^{bl_A}[1+(1-\Delta'/E')abl_A]\times\int_{E_{0\min}}^{E_0-\Delta E_0}dE'_0[\ln(E_0/E'_0)]^{bl_B}(E_0-E'_0)^{-1}(bt_BR_B+v_Bv'S_B)\frac{d^2\sigma}{d\Omega dE'}(E'_0,E',\theta), \tag{B6}$$

where

$$L=t_A+t_B+(v_A+v_B)/b,$$

$$v_A=v_B=\frac{\alpha}{\pi}[\ln(q^2/m^2)-1],$$

$$v'=1+\tfrac{1}{2}(v_A+v_B)[1+\ln(\eta)],$$

$$\eta=1+(2E_0/M)\sin^2(\tfrac{1}{2}\theta),$$

$$\Delta=\tfrac{1}{2}\{E_0-E'/[1-(2E'/M)\sin^2(\tfrac{1}{2}\theta)]\},$$

$$\Delta'=\tfrac{1}{2}\{E_0/[1+(2E_0/M)\sin^2(\tfrac{1}{2}\theta)]-E'\},$$

$$R_A=E'/E_{0f}+\tfrac{3}{4}[(E_{0f}-E')/E_{0f}]^2,$$

$$R_B=E'_0/E_0+\tfrac{3}{4}[(E_0-E'_0)/E_0]^2,$$

$$S_A=E'/E_{0f}+\tfrac{1}{2}[(E_{0f}-E')/E_{0f}]^2,$$

$$S_B=E'_0/E_0+\tfrac{1}{2}[(E_0-E'_0)/E_0]^2,$$

and other terms have been defined previously.

The radiative corrections to the measured elastic cross sections used the formula:

$$C(\Delta E')=[(1+1.103t_B)(1+1.103t_A)]\times\exp[a_0+b_0+\delta(\Delta E')], \tag{B7}$$

where

$$a_0=\tfrac{4}{3}t_A\ln(E_0/\eta\Delta E'),$$

$$b_0=\tfrac{4}{3}t_B\ln(E_0/\eta^2\Delta E'),$$

$$\eta=1+\left(\frac{2E_0}{M}\right)\sin^2(\tfrac{1}{2}\theta)$$

and $\delta(\Delta E')$ is calculated following Tsai.[45] $\Delta E'$ is the width of the missing-energy bin to which the correction factor $C(\Delta E')$ is applied to correct for electrons lost from that bin because of radiative energy loss.

APPENDIX C: NUCLEAR-BINDING EFFECTS IN THE DEUTERON

Extraction of neutron differential cross sections from e-d differential cross sections requires corrections for nuclear binding effects in the deuteron. In deep-inelastic electron scattering processes, the most important corrections arise from the Fermi motion of the neutron and the proton.[20] In the following discussion we present an outline of the calculation of the Fermi-motion effects, commonly referred to as "smearing" effects. The method used is derived from the work of Atwood and West.[19] Also discussed are other binding corrections which are expected to be small.

Investigations of deuteron binding corrections[18,19] primarily utilize the incoherent impulse approximation. In this approximation, as shown in Fig. 42, only one nucleon is directly engaged in the scattering process (the interaction nucleon), while the other nucleon (the spectator nucleon) is unaffected. The spectator nucleon is on the mass shell before and after the interaction, while the interaction nucleon is initially off the mass shell and is brought back on to the mass shell by the absorption of the virtual photon. The square of the deuteron scattering matrix elements is then the

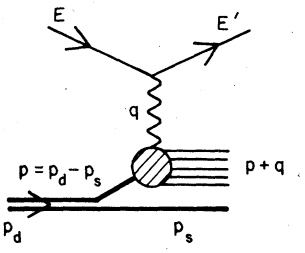

FIG. 42. Feynman diagram for inelastic electron-deuteron scattering.

sum of the squares of the corresponding neutron and proton matrix elements. An evaluation of the amplitude of the process in the diagram of Fig. 42 will yield a relationship between deuteron and corresponding neutron and proton matrix elements. The deuteron electromagnetic tensor $W^d_{\mu\nu}$ is directly related to the square of the invariant matrix element for scattering from deuterium. Atwood and West[19] express the deuteron tensor in terms of off-shell neutron and proton tensors:

$$W^d_{\mu\nu} = \int_0^\infty |f(\vec{p})|^2 (W^p_{\mu\nu} + W^n_{\mu\nu}) d^3p \,, \tag{C1}$$

where

$$W^p_{\mu\nu} = -W^p_1(q^2, W'^2, q\cdot p)\left(q_{\mu\nu} - \frac{q_\mu q_\nu}{q^2}\right) + \frac{W_2(q^2, W'^2, q\cdot p)}{M^2}\left(p_\mu - \frac{q\cdot p}{q^2}q_\mu\right)\left(p_\nu - \frac{q\cdot p}{q^2}q_\nu\right), \tag{C2}$$

with an analogous expression for $W^n_{\mu\nu}$. Here $p = p_d - p_s$ is the off-shell four-momentum of the interacting nucleon, and p_s is the four-momentum of the on-shell spectator nucleon. The momentum p_d is the four-momentum of the target deuteron. We define the 3 direction to be the direction of the virtual photon's momentum $q = (0, 0, q_3, \nu)$ in the laboratory system. In the laboratory system we also have $p_d = (0, 0, 0, M_d)$, where M_d is the deuteron mass; and $p = (p_x, p_y, p_3, p_0) = (\vec{p}, p_0) = (-\vec{p}_s, p_0)$, where $p_0 = M_d - (p_s^2 + M^2)^{1/2}$. The square of the mass of the interacting nucleon's final state is $(W')^2 = (p+q)^2$.

The off-shell structure functions W_1 and W_2 in Eq. (C2) depend on the three independent invariants $Q^2 = -q^2$, $(W')^2$ and $\nu' = q\cdot p/M$ (defined such that all three are positive-definite). The three variables are independent because the interacting nucleon is off the mass shell and p^2 is variable.

The quantity $|f(\vec{p})|^2$ is the momentum distribution of the nucleon within the deuteron. By making a correspondence with elastic e-d scattering, West[19] identifies $|f(\vec{p})|^2$ with the square of the nonrelativistic deuteron wave function in momentum space $|\phi(\vec{p})|^2$. The quantity $|\phi(\vec{p})|^2$ is spherically symmetric and can be directly expressed in terms of the S-wave and D-wave components of the nonrelativistic deuteron wave function.

$$|f(\vec{p})|^2 = |\phi(|\vec{p}|)|^2 = |U_p(\vec{p})|^2 + |W_p(\vec{p})|^2 \equiv |f(|\vec{p}|)|^2 . \tag{C3}$$

The S-wave component is

$$U_p(\vec{p}) = \left(\frac{1}{2\pi^2}\right)^{1/2} \int_0^\infty \frac{U(r)}{r} j_0(|\vec{p}|r) r^2 dr \,;$$

the D-wave component is

$$W_p(\vec{p}) = \left(\frac{1}{2\pi^2}\right)^{1/2} \int_0^\infty \frac{W(r)}{r} j_2(|\vec{p}|r) r^2 dr \,.$$

The Hamada-Johnston wave function[48] was used in the calculation of smearing connections for these experiments.

The tensor equation (C1) yields 16 separate dependent equations, one for each component. Examination of the various tensorial components yields the following two equations:

$$W^p_{1s} = \int_0^\infty |f(\vec{p})|^2 [W_1(Q^2, W'^2, \nu') + W_2(Q^2, W'^2, \nu')] \frac{|\vec{p}|^2 - p_3^2}{2M^2} d^3p \,, \tag{C4}$$

$$W^p_{2s} = \int_0^\infty |f(\vec{p})|^2 \left[\left(1 - \frac{p_3 Q^2}{M\nu' q_3}\right)^2 \left(\frac{\nu'}{\nu}\right)^2 + \frac{|\vec{p}|^2 - p_3^2}{2M^2}\left(\frac{Q^2}{q_3^2}\right)\right] W_2(Q^2, \nu', W'^2) d^3p \,,$$

where W^p_{1s} and W^p_{2s} are smeared proton structure functions. Similar expressions are obtained for the smeared neutron struction functions W^n_{1s} and W^n_{2s}. The deuteron structure functions are taken to be the sum of the corresponding smeared proton and neutron structure functions.

$$W^d_1(Q^2, \nu) = W^p_{1s}(Q^2, \nu) + W^n_{1s}(Q^2, \nu) \,,$$
$$W^d_2(Q^2, \nu) = W^p_{2s}(Q^2, \nu) + W^n_{2s}(Q^2, \nu) \,. \tag{C5}$$

We define the following "smearing ratios" of structure functions:

$$S_{p1}=W_1^p/W_{1s}^p\,,\quad S_{p2}=W_2^p/W_{2s}^p\,,$$
$$S_{n1}=W_1^n/W_{1s}^n\,,\quad S_{n2}=W_2^n/W_{2s}^n\,. \tag{C6}$$

The smeared and unsmeared structure functions can be combined according to Eq. (1.1) to form smeared and unsmeared differential cross sections ($\sigma_{ps},\sigma_{ns},\sigma_p,\sigma_n$). The smearing ratios (or smearing corrections) for the cross sections are defined in an analogous way:

$$S_p=\frac{\sigma_p}{\sigma_{ps}}\,,\quad S_n=\frac{\sigma_n}{\sigma_{ns}}\,, \tag{C7}$$

and $U=S_n/S_p$ is defined as the unsmearing correction.

1. Identification of off-shell structure functions

The off-shell structure functions are identified[20] with the on-shell structure functions for the same Q^2 and $(W')^2=W^2$. The Fermi motion does not change the effective Q^2 of the interaction because the four-momentum transfer is determined by the electron's kinematics and is independent of whether the initial nucleon is on or off the mass shell. However, conservation of energy requires that the effective W is dependent on the off-shell kinematics, as energy is required to bring the nucleon back on to the mass shell. Some distinct features of the structure functions are directly dependent on the final-state mass. For example, the distinction between quasielastic and inelastic electron-deuteron scattering is determined by whether the final state of the interacting nucleon is a single nucleon or contains pions. The off-shell structure functions must vanish at pion threshold ($W'=M+m_\pi$, where m_π is the pion mass). Also, the resonance spectra are described by functions of W for on-mass-shell structure functions. They should be described by the same functions of W' for off-shell structure functions if the resonance masses are to be the same. The off-shell structure functions were defined in terms of on-shell structure functions as follows:

$$\begin{aligned} W_1(Q^2,W'^2,\nu')\big|_{\text{off shell}} &\equiv W_1(Q^2,W'^2)\big|_{\text{off shell}} \\ &\equiv W_1(Q^2,W^2)\big|_{\text{on shell}}\,, \\ W_2(Q^2,W'^2,\nu')\big|_{\text{off shell}} &\equiv W_2(Q^2,W'^2)\big|_{\text{off shell}} \\ &\equiv W_2(Q^2,W^2)\big|_{\text{on shell}}\,. \end{aligned} \tag{C8}$$

In our analysis, according to the above definitions, the off-shell structure functions were described by the universal fit [given in Sec. V C, Eq. (51)], as follows:

$$W_2\big|_{\text{off shell}}=\frac{A(W',Q^2)f(\tilde\omega_w)}{\tilde\nu\,\tilde\omega}\,,$$
$$W_1\big|_{\text{off shell}}=\left(\frac{1+\tilde\nu^2/Q^2}{1+R}\right)W_2\big|_{\text{off shell}}\,, \tag{C9}$$

where

$$\tilde\omega_w=\frac{2M\tilde\nu+a^2}{Q^2+b^2}\,,$$

$$\tilde\omega=\frac{2M\tilde\nu}{Q^2}\,,$$

and

$$\tilde\nu=\frac{W'-Q^2-M^2}{2M}\,;$$

for R, we used $R_p=R_n=0.18$. These structure functions correspond to the case of no off-shell corrections.

In order to get some idea of possible off-shell corrections, the smearing expressions [Eq. (C4)] were investigated[20,63] in the limit $Q^2\to 0$, where the longitudinal virtual photoabsorption cross section for the deuteron σ_{Ld} must vanish according to gauge invariance. It has been shown[20,63] that the smearing expressions do not yield a vanishing σ_{Ld} as $Q^2\to 0$ unless small off-shell corrections are applied to the structure functions. As $Q^2\to 0$, Eq. (C4) become

$$\begin{aligned} W_1^d(Q^2,\nu)&=\int|f(\vec p)|^2[W_1^p(Q^2,W')+W_1^n(Q^2,W')]d^3p\,, \\ W_2^d(Q^2,\nu)&=\int|f(\vec p)|^2\left(\frac{\nu'}{\nu}\right)^2 \\ &\quad\times[W_2^p(Q^2,W')+W_2^n(Q^2,W')]d^3p\,. \end{aligned} \tag{C10}$$

Now, from Eqs. (1.3) in the limit $Q^2\to 0$,

$$\sigma_{Ld}=\frac{4\pi^2\alpha}{\nu}\left(\frac{\nu^2}{Q^2}W_2^d(\nu,Q^2)-W_1^d(\nu,Q^2)\right)\,. \tag{C11}$$

Combining Eqs. (C10) and (C11) we get

$$\lim_{\substack{Q^2\to 0\\ \nu\ \text{fixed}}}\sigma_{Ld}=\frac{4\pi^2\alpha}{\nu}\int|f(\vec p)|^2\left\{\left[\frac{\nu'}{Q^2}W_2^p(Q^2,W')-W_1^p(Q^2,W')\right]+\left[\frac{\nu'^2}{Q^2}W_2^n(Q^2,W')-W_1^n(Q^2,W')\right]\right\}d^3p\,. \tag{C12}$$

The above expression does not yield a vanishing σ_{Ld} as $Q^2 \to 0$ because the on-shell structure functions as defined by Eq. (C9) do not vanish for that particular combination of off-shell variables. The necessary limiting behavior is

$$\lim_{\substack{Q^2\to 0 \\ \nu \text{ fixed}}} \sigma_{Lp}\alpha\left[\frac{\nu'^2}{Q^2} W_2^p(Q^2,\nu') - W_1^p(Q^2,\nu')\right] = 0 \qquad \text{(C13a)}$$

or

$$\lim_{\substack{Q^2\to 0 \\ \nu \text{ fixed}}} \sigma_{Lp}\alpha\left[\frac{\tilde{\nu}^2}{Q^2} W_2^p(Q^2,W') - W_1^p(Q^2,W')\right] = 0 . \qquad \text{(C13b)}$$

So it appears that a simple correspondence between on-shell structure functions and off-shell structure functions does not yield a physical result at $Q^2 = 0$. This defect can be corrected by the application of off-shell corrections. However, the W dependence of the off-shell structure functions must remain invariant in order to maintain the proper threshold and resonance positions. One method to accomplish this end is a mixed variable approach wherein we factor out the resonance and threshold behavior in the $A(W, Q^2)$ part of the fit to the structure functions, as was already done in Eq. (C9). In the mixed variable approach the off-shell $A(W, Q^2)$ is then $A(W', Q^2)$, while $\tilde{\nu}$ is replaced by ν' in Eq. (C9). The constraint at $Q^2 = 0$ is satisfied as implied by Eq. (C13a). Another way to satisfy this constraint is to apply multiplicative off-shell corrections to the structure functions which will make σ_{Ld} vanish at $Q^2 = 0$ by yielding Eq. (C13b) in that limit. For example, we define two possible off-shell corrections.

Off-shell correction A:

$$W_2^p(Q^2,W',\nu')|_{\text{off shell}} = \left(\frac{\tilde{\nu}}{\nu'}\right)^2 W_2^p(Q^2,W)|_{\text{on shell}} ,$$
$$W_1^p(Q^2,W',\nu')|_{\text{off shell}} = W_1^p(Q^2,W)|_{\text{on shell}} . \qquad \text{(C14)}$$

Off-shell correction B:

$$W_2^p(Q^2,W',\nu')|_{\text{off shell}} = W_2^p(Q^2,W)|_{\text{on shell}} ,$$
$$W_1^p(Q^2,W',\nu')|_{\text{off shell}} = \left(\frac{\nu'}{\tilde{\nu}}\right)^2 W_1^p(Q^2,W)|_{\text{on shell}} . \qquad \text{(C15)}$$

Note that any definition which yields off-shell correction A or off-shell correction B, or a linear combination of them, will also work. The three off-shell corrections that were discussed [mixed variables (MX), A, and B] vanish as $Q^2 \to \infty$ because in that limit $\tilde{\nu} \to \nu'$.

The nominal smearing ratios used in our analysis were the average between the ratios obtained from the calculation using no off-shell corrections (C9) and the ratios obtained using the mixed-variable approach. The error in the smearing ratio due to the uncertainties in the off-shell corrections was taken to be the difference between the nominal smearing ratio and the ratio obtained with no off-shell corrections. The uncertainties in the extracted σ_n/σ_p values due to uncertainties in the off-shell corrections are given in Table X along with the other errors. Values of the nominal smearing ratios for W_1 and W_2 for the neutron and proton are presented in Table XXVII for the kinematic points (x, Q^2) used in the extraction of R and the structure functions. Smearing ratios for various off-shell corrections are presented in Table XXVIII for representative values of (x, Q^2).

2. Deuteron wave functions

There are phenomenological nonrelativistic wave functions[65,75] other than the Hamada-Johnston wave functions[48] which can also be used. These wave functions should describe all known properties of the deuteron such as its binding energy, magnetic and quadrupole moment, the $n-p$ phase shifts, and the measured elastic $e-d$ form factors.[49] The elastic $e-d$ measurements[49] indicate that the Hamada-Johnston wave function[48] (HJ) and the Reid soft-core (RSC) and hard-core (RHC) wave functions[65] are in best agreement with the measured form factors. The Feshbach-Lomon (FL) and the Hulthén hard-core (HHC) wave functions are in lesser agreement with the measured form factors. The Hulthén (no-core) wave function is in poor agreement with those measurements. The momentum distributions obtained from some of these wave functions are shown in Fig. 43. The smearing ratios calculated using these wave functions are presented for comparison in Table XXVIII.

3. Effects of smearing on R

As is evident from Table XXVII, the smearing corrections for W_1 and W_2 are nearly the same, i.e., $S_{p1} \cong S_{p2}$ and $S_{n1} \cong S_{n2}$. A straightforward derivation[20] shows that in that case the smeared and unsmeared values of R are equal and R_n can be directly extracted from the measured hydrogen and deuterium data by the following expression:

$$R_d = R_p\left(\frac{1}{1+Z}\right) + R_n\left(\frac{Z}{1+Z}\right) \qquad \text{(C16)}$$

or

$$R_n = R_d + \frac{\delta}{Z} , \qquad \text{(C17)}$$

where $\delta = R_d - R_p$ and $Z = W_{1ns}/W_{1ps} = (W_{1n}/W_{p1}) \times (S_{n1}/S_{p1})$ is the smeared neutron-to-proton ratio for the W structure function. The above expression implies that if we find that $R_d = R_p$ (i.e.,

TABLE XXVII. Nominal smearing ratios.

x	Q^2 (GeV^2)	S_{p1}	S_{p2}	S_{n1}	S_{n2}	x	Q^2 (GeV^2)	S_{p1}	S_{p2}	S_{n1}	S_{n2}
0.100	1.0	1.015	1.012	1.017	1.014	0.400	4.0	1.028	1.028	1.028	1.028
0.100	1.25	1.015	1.012	1.017	1.014	0.400	5.0	1.027	1.028	1.027	1.027
0.100	1.5	1.015	1.013	1.017	1.015	0.400	6.0	1.027	1.028	1.027	1.027
0.100	2.0	1.015	1.013	1.017	1.015	0.400	7.0	1.028	1.028	1.027	1.027
0.100	2.5	1.015	1.013	1.017	1.015	0.400	8.0	1.028	1.028	1.027	1.027
0.150	1.0	1.016	1.013	1.018	1.015	0.400	9.0	1.028	1.028	0.027	1.027
0.150	1.25	1.016	1.013	1.018	1.015	0.500	3.0	1.033	1.035	1.032	1.034
0.150	1.5	1.016	1.014	1.018	1.016	0.500	4.0	1.031	1.032	1.029	1.031
0.150	2.0	1.016	1.015	1.018	1.016	0.500	5.0	1.030	1.031	1.028	1.029
0.150	2.5	1.016	1.015	1.018	1.017	0.500	6.0	1.030	1.030	1.027	1.028
0.150	3.0	1.017	1.015	1.018	1.017	0.500	7.0	1.029	1.030	1.026	1.027
0.150	3.5	1.017	1.016	1.018	1.017	0.500	8.0	1.029	1.029	1.026	1.026
0.200	1.0	1.019	1.016	1.021	1.018	0.500	10.0	1.028	1.029	1.025	1.025
0.200	1.25	1.018	1.016	1.020	1.018	0.500	12.0	1.028	1.028	1.024	1.024
0.200	1.5	1.018	1.016	1.020	1.018	0.600	5.0	1.025	1.027	1.019	1.021
0.200	2.0	1.018	1.016	1.020	1.018	0.600	6.0	1.026	1.028	1.019	1.021
0.200	2.5	1.018	1.017	1.020	1.019	0.600	7.0	1.025	1.027	1.017	1.019
0.200	3.0	1.018	1.017	1.020	1.019	0.600	8.0	1.024	1.025	1.016	1.017
0.200	3.5	1.019	1.018	1.020	1.019	0.600	10.0	1.022	1.023	1.013	1.014
0.200	4.0	1.019	1.018	1.020	1.019	0.600	12.0	1.020	1.020	1.010	1.011
0.250	1.0	1.024	1.022	1.026	1.024	0.600	14.0	1.019	1.020	1.009	1.010
0.250	1.25	1.021	1.019	1.023	1.021	0.667	6.0	1.014	1.017	1.003	1.006
0.250	1.5	1.021	1.019	1.022	1.021	0.667	7.0	1.013	1.013	1.000	1.003
0.250	2.0	1.020	1.019	1.022	1.021	0.667	8.0	1.012	1.014	0.998	1.001
0.250	2.5	1.020	1.019	1.022	1.021	0.667	10.0	1.009	1.011	0.994	0.995
0.250	3.0	1.020	1.020	1.022	1.021	0.667	12.0	1.006	1.007	0.989	0.991
0.250	4.0	1.021	1.020	1.022	1.021	0.667	14.0	1.003	1.004	0.986	0.987
0.250	5.0	1.021	1.020	1.022	1.022	0.667	16.0	1.001	1.002	0.983	0.984
0.333	1.5	1.029	1.028	1.030	1.029	0.750	8.0	0.968	0.971	0.943	0.947
0.333	2.0	1.025	1.025	1.026	1.026	0.750	9.0	0.973	0.976	0.946	0.950
0.333	2.5	1.025	1.024	1.026	1.025	0.750	10.0	0.968	0.970	0.939	0.942
0.333	3.0	1.025	1.024	1.025	1.025	0.750	12.0	0.965	0.967	0.933	0.936
0.333	4.0	1.025	1.024	1.025	1.025	0.750	14.0	0.960	0.962	0.926	0.929
0.333	5.0	1.025	1.025	1.025	1.025	0.750	16.0	0.955	0.957	0.920	0.922
0.333	6.0	1.025	1.025	1.025	1.025	0.800	12.0	0.915	0.918	0.871	0.874
0.333	7.0	1.025	1.025	1.025	1.025	0.800	14.0	0.906	0.909	0.858	0.862
0.400	2.0	1.032	1.032	1.032	1.033	0.800	16.0	0.900	0.903	0.850	0.853
0.400	3.0	1.028	1.028	1.028	1.029						

$\delta = 0$) then it follows that $R_n = R_p$. It also follows that the uncertainty in the extracted R_n is largest at small ω because in that region the neutron-to-proton ratio is small.

On the other hand, if $S_{p1} \neq S_{p2}$ then smearing affects R and the smeared value of $R_p(R_{ps})$ will not be equal to R_p. As was discussed in Appendix C 1, possible off-shell corrections to the structure functions could be different for W_1 and W_2 and yield values of S_{p1} which are different from S_{p2}. The difference between the smeared and unsmeared values of R_p is then

$$\gamma_p = R_{ps} - R_p = \left(\frac{S_{p1}}{S_{p2}} - 1\right)(1 + R_p) \tag{C18}$$

and

$$R_d = R_{ps}\left(\frac{1}{1+Z}\right) + R_{ns}\left(\frac{Z}{1+Z}\right). \tag{C19}$$

Representative values of γ_p, calculated using our fit to the proton data under the assumption $R_p = 0.18$, are given in Table XXIX along with various possible off-shell corrections. These values can be taken as the estimate of the possible changes in R_p due to off-shell effects in the deuteron. Uncertainties in the wave function do not affect R because they influence W_1 and W_2 in the same way.

4. Other deuteron corrections

Other deuteron corrections which were neglected in our incoherent impulse approximation are the subject of this section. The incoherent impulse

TABLE XXVIII. Smearing ratios for off-shell corrections.

		No off-shell corr		Various off-shell corrections						Various wave functions			
x	Q^2 (GeV^2)	SP_1^0 (HJ)	SP_2^0 (HJ)	SP_1^{MX} (HJ)	SP_2^{MX} (HJ)	SP_1^A (HJ)	SP_2^A (HJ)	SP_1^B (HJ)	SP_2^B (HJ)	SP_2^0 (RSC)	SP_2^0 (RHC)	SP_2^0 (FL)	SP_2^0 (HHC)
0.100	1.0	1.017	1.009	1.013	1.014	1.017	1.019	1.007	1.009	1.008	1.010	1.011	1.007
	1.5	1.016	1.011	1.014	1.014	1.016	1.017	1.010	1.011	1.009	1.012	1.013	1.008
	2.5	1.016	1.013	1.014	1.015	1.016	1.017	1.012	1.013	1.011	1.014	1.014	1.010
0.150	1.0	1.019	1.009	1.014	1.017	1.019	1.023	1.005	1.009	1.008	1.010	1.011	1.007
	2.0	1.018	1.013	1.015	1.016	1.018	1.020	1.011	1.013	1.011	1.014	1.014	1.009
	3.5	1.018	1.015	1.016	1.016	1.018	1.019	1.014	1.015	1.013	1.016	1.016	1.011
0.200	1.0	1.022	1.012	1.016	1.020	1.022	1.028	1.004	1.012	1.010	1.012	1.014	1.008
	2.5	1.020	1.016	1.016	1.018	1.020	1.022	1.013	1.016	1.013	1.016	1.017	1.011
	4.0	1.020	1.017	1.017	1.019	1.020	1.021	1.016	1.017	1.015	1.018	1.018	1.013
0.250	1.0	1.027	1.017	1.021	1.027	1.028	1.037	1.006	1.017	1.014	1.018	1.019	1.013
	3.0	1.023	1.019	1.018	1.021	1.023	1.025	1.016	1.019	1.014	1.019	1.020	1.014
	5.0	1.023	1.020	1.020	1.021	1.023	1.024	1.018	1.020	1.018	1.021	1.021	1.015
0.333	1.5	1.033	1.026	1.025	1.031	1.033	1.042	1.015	1.026	1.023	1.026	1.027	1.020
	4.0	1.027	1.024	1.022	1.025	1.027	1.031	1.021	1.024	1.021	1.025	1.025	1.018
	7.0	1.027	1.025	1.023	1.025	1.027	1.029	1.023	1.025	1.022	1.026	1.025	1.019
0.400	2.0	1.036	1.031	1.027	1.033	1.037	1.046	1.021	1.031	1.028	1.032	1.032	1.024
	5.0	1.031	1.028	1.024	1.027	1.031	1.034	1.024	1.028	1.026	1.029	1.028	1.022
	9.0	1.030	1.028	1.026	1.027	1.030	1.032	1.026	1.028	1.026	1.029	1.028	1.022
0.500	3.0	1.040	1.036	1.027	1.034	1.040	1.048	1.027	1.036	1.033	1.037	1.037	1.029
	7.0	1.033	1.031	1.025	1.028	1.033	1.037	1.028	1.031	1.029	1.032	1.031	1.026
	12.0	1.030	1.029	1.025	1.027	1.030	1.033	1.027	1.029	1.027	1.030	1.029	1.025
0.600	5.0	1.033	1.031	1.018	1.024	1.033	1.040	1.023	1.031	1.029	1.032	1.031	1.026
	8.0	1.029	1.028	1.018	1.022	1.029	1.034	1.023	1.028	1.027	1.029	1.029	1.025
	14.0	1.022	1.022	1.015	1.018	1.022	1.025	1.019	1.022	1.021	1.022	1.023	1.020
0.667	6.0	1.023	1.022	1.005	1.012	1.023	1.031	1.014	1.022	1.021	1.023	1.023	1.019
	10.0	1.015	1.015	1.002	1.007	1.016	1.020	1.010	1.015	1.014	1.015	1.016	1.014
	16.0	1.006	1.005	0.996	0.999	1.006	1.009	1.002	1.005	1.005	1.005	1.007	1.007
0.750	8.0	0.978	0.978	0.957	0.964	0.979	0.986	0.970	0.978	0.979	0.973	0.981	0.981
	12.0	0.973	0.973	0.956	0.961	0.974	0.979	0.967	0.973	0.975	0.973	0.977	0.980
	16.0	0.962	0.962	0.948	0.952	0.962	0.967	0.958	0.962	0.964	0.961	0.967	0.971
0.800	12.0	0.926	0.926	0.903	0.910	0.926	0.933	0.919	0.926	0.929	0.925	0.932	0.938
	14.0	0.917	0.917	0.896	0.902	0.917	0.923	0.910	0.917	0.921	0.915	0.923	0.930

approximation is expected to work best at large values of Q^2. Most corrections to the impulse approximation are expected to be small in the Q^2 range of this experiment (1 to 20 GeV^2). Similar discussions of corrections to the impulse approximation in the case of inelastic e-d scattering are given in Refs. 19 and 20.

1. Glauber-type[99] shadowing corrections. This is a multiple-scattering correction which occurs because one nucleon may shadow the other. It is important in hadronic scattering where cross sections are large. In hadronic reactions this correction is typically[19] 5% even at asymptotic energies. In electron scattering the double scattering is presumably electromagnetic and therefore suppressed[19] by a factor of α. Calculations[20] show that in that case the correction is less than 0.1% at an incident electron energy of 20 GeV. Vector dominance[13,100] allows a virtual photon to propagate as a hadron such that the second scattering is hadronic and therefore not suppressed. However, simple vector-dominance models[13,101] also predict large shadowing in electron scattering from high-A nuclei. These predictions are in disagreement with experiment.[100] Experimentally, no shadowing was observed in the electroproduction experiment even at Q^2 values as low as 0.25 GeV^2. These experiments indicate that shadowing will also be small in the deuteron. Further refinements[102] of the vector-dominance model yield

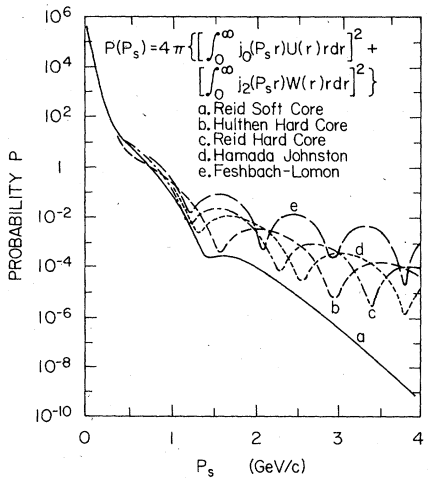

FIG. 43. Momentum distributions in the deuteron for five different wave functions.

shadowing corrections for high-A nuclei markedly smaller than those of the old vector-dominance model. The new theories predict little shadowing at high Q^2 and small ν. Therefore, even within vector-dominance theories the shadowing correction in deuterium is expected to be small in the Q^2 range of this experiment.

2. *Interference terms and coherent effects.* These corrections have been estimated[20] to be on the order of $F_d^2(Q^2)$, the square of the wave-function part of the deuteron form factor, which is negligible in the Q^2 range of this experiment.

3. *Meson currents in the deuteron.* These corrections arise from the fact that the deuteron wave function probably contains a small amplitude for the deuteron to exist as two nucleons and one or more pions, a nucleon and a nucleon isobar state and other such states. These corrections are

TABLE XXIX. Typical values of γ_p.

x	Q^2 (GeV^2)	γ_p^{nom}	γ_p^0	γ_p^{MX}	γ_p^{A}	γ_p^{B}
0.100	1.0	0.004	0.009	−0.002	−0.002	−0.003
	1.5	0.003	0.006	−0.001	−0.001	−0.002
	2.5	0.002	0.004	−0.001	−0.001	−0.001
0.150	1.0	0.004	0.011	−0.003	−0.004	−0.005
	2.0	0.002	0.006	−0.002	−0.002	−0.002
	3.5	0.001	0.003	−0.001	−0.001	−0.001
0.200	1.0	0.004	0.012	−0.005	−0.007	−0.009
	2.5	0.002	0.005	−0.002	−0.003	−0.003
	4.0	0.001	0.003	−0.001	−0.002	−0.002
0.250	1.0	0.003	0.012	−0.006	−0.010	−0.013
	3.0	0.001	0.005	−0.003	−0.003	−0.003
	5.0	0.001	0.003	−0.002	−0.002	−0.002
0.330	1.5	0.001	0.008	−0.007	−0.010	−0.012
	4.0	0.001	0.004	−0.003	−0.004	−0.004
	7.0	0.000	0.002	−0.002	−0.002	−0.002
0.400	2.0	−0.001	0.006	−0.007	−0.010	−0.011
	5.0	−0.001	0.003	−0.004	−0.004	−0.004
	9.0	0.000	0.002	−0.002	−0.002	−0.002
0.500	3.0	−0.001	0.004	−0.007	−0.010	−0.010
	7.0	−0.001	0.002	−0.004	−0.004	−0.004
	12.0	−0.001	0.001	−0.002	−0.002	−0.003
0.600	5.0	−0.003	0.002	−0.007	−0.008	−0.009
	8.0	−0.002	0.001	−0.005	−0.005	−0.005
	14.0	0.001	0.001	−0.003	−0.003	−0.003
0.667	6.0	−0.004	0.001	−0.008	−0.008	−0.009
	10.0	−0.002	0.001	−0.005	−0.005	−0.006
	16.0	0.002	0.001	−0.004	−0.004	−0.004
0.750	8.0	−0.005	0.000	−0.009	−0.009	−0.009
	12.0	−0.004	0.000	−0.007	−0.007	−0.007
	16.0	−0.003	0.000	−0.005	−0.005	−0.005
0.800	12.0	−0.005	0.000	−0.009	−0.008	−0.009
	14.0	−0.004	0.000	−0.008	−0.008	−0.008
	16.0	−0.004	0.000	−0.007	−0.007	−0.007

known to be small in elastic e-d scattering,[50] and in quasielastic e-d scattering,[103] and probably contribute only at large ω.

4. *Off-mass-shell corrections to the nucleon structure functions.* Some estimates of these corrections have been made in this appendix. The error arising from uncertainties in these corrections has been included in our final errors.

5. *Final-state-interaction effects.* These effects are known to be small at large Q^2 for quasielastic e-d scattering.[50,52,104,105] These effects are only important when the relative momentum between the outgoing final particles is small. In the deep-inelastic case, these effects are expected to be small[20] because of the large energy and momentum transfers that are involved.

6. *Relativistic corrections to the deuteron wave function.* The practical relativistic bound-state problem is still in a rather crude state. It is possible that the phenomenological nonrelativistic deuteron wave functions that we use may include relativistic effects in a phenomenological way because they are fitted to data. There have also been suggestions[19] that the deuteron wave function contains high-momentum components in larger than expected amounts. The existence of a large amplitude for high momentum means that if those high-momentum wave functions were used in the extraction of σ_n from present deuterium data then σ_n would be smaller than the cross section extracted with standard deuteron wave functions. The extracted neutron cross section is small in the small-ω region; therefore, the inclusion of a large amplitude for high-momentum components will result in a neutron cross section which is extremely small (i.e., $\sigma_n/\delta_p \approx 0$) or even negative. There is no convincing evidence at present for the existence of a large amplitude for high-momentum components in the deuteron wave function. Experiments in which the spectator momentum distribution in deuteron quasielastic hadronic processes is measured[106] can account for the observed distribution within models based on conventional wave functions and including Glauber and final-state corrections.

Recently, theoretical studies[107,108] of the deuteron wave function in the infinite-momentum frame have indicated that relativistic corrections may decrease the smearing ratio $S_p = \sigma_p/\sigma_{ps}$ by a small fraction which varies from 1.5% at $X = 0$ to 3% at $X = 0.8$. These corrections are such as to *decrease* the final extracted neutron cross section over the entire range of X, and bring the ratio σ_n/σ_p down closer to the quark model limit of 0.25.

---

*Present address: Department of Physics, University of Rochester, Rochester, New York 14627.
†Present address: Stanford Linear Accelerator Center, Stanford, California 94305.
‡Present address: Fermi National Accelerator Laboratory, Batavia, Illinois 60510.
§Present address: Department of Physics and Astronomy, Vanderbilt University, Nashville, Tennessee 37235.
‖Present address: c/o Cheshire Books, 514 Bryant Street, Palo Alto, California 94301.
¶Present address: Enrico Fermi Institute, University of Chicago, Chicago, Illinois 60637.

[1]Recent tests of quantum electrodynamics in e^+e^- interactions are reviewed by B. Richter, in *Proceedings of the XVII International Conference on High-Energy Physics, London, 1974,* edited by J. R. Smith (Rutherford Laboratory, Chilton, Didcot, Berkshire, England, 1974). Also J.-E. Augustin *et al.*, Phys. Rev. Lett. 34, 233 (1975); B. L. Beron *et al.*, *ibid.* 33, 663 (1974); H. Newman *et al.*, *ibid.* 32, 483 (1974); M. Bernardini *et al.*, Phys. Lett. 45B, 510 (1973).
[2]R. W. McAllister and R. W. Hofstadter, Phys. Rev. 102, 851 (1956); M. R. Yearian and R. W. Hofstadter, *ibid.* 110, 552 (1958).
[3]See the rapporteur's talk by G. Weber, in the *Proceedings of the Third International Symposium on Electron and Photon Interactions at High Energies, Stanford, 1967* (Clearing House of Federal Scientific and Technical Information, Washington, D.C., 1968); also see the talk by R. E. Taylor in the same Proceedings and Ref. 29.
[4]*Electron Scattering and Nuclear and Nucleon Scattering*, edited by Robert Hofstadter (Benjamin, New York, 1963).
[5]E. D. Bloom *et al.*, Phys. Rev. Lett. 23, 930 (1969); M. Breidenbach *et al.*, *ibid.* 23, 935 (1969); see also Ref. 46.
[6]R. P. Feynman, in *High Energy Collisions, Proceedings of the Third International Conference, Stony Brook, 1969,* edited by C. N. Yang *et al.* (Gordon and Breach, New York, 1969); also *Photon-Hadron Interactions* (Benjamin, New York, 1972).
[7]G. Miller *et al.*, Phys. Rev. D 5, 528 (1972); also Ref. 41.
[8]J. S. Poucher *et al.*, Phys. Rev. Lett. 32, 118 (1974).
[9]S. D. Drell and J. D. Walecka, Ann. Phys. (N.Y.) 28, 18 (1964).
[10]L. N. Hand, Phys. Rev. 129, 1834 (1963); see also L. N. Hand, Ph.D. thesis, Stanford University, 1961 (unpublished).
[11]J. D. Bjorken, Phys. Rev. 179, 1547 (1969).

[12]J. W. Moffat and V. G. Snell, Phys. Rev. D 3, 2848 (1971).
[13]J. J. Sakurai, Phys. Rev. Lett. 22, 981 (1969).
[14]G. Domokos, S. Kovesi-Domokos, and E. Schonberg, Phys. Rev. D 3, 1184 (1971).
[15]M. S. Chanowitz and S. D. Drell, Phys. Rev. Lett. 30, 807 (1973); Phys. Rev. D 9, 2078 (1974); M. Pavkovic, Phys. Lett. 46B, 435 (1973).
[16]G. B. West and P. Zerwas, Phys. Rev. D 10, 2130 (1974).
[17]K. G. Wilson, Phys. Rev. 179, 1499 (1969); G. Parisi, Phys. Lett. 43B, 207 (1973).
[18]H. Georgi and H. D. Politzer, Phys. Rev. D 9, 416 (1974); D. J. Gross and F. Wilczek, *ibid.* 9, 980 (1974); D. J. Gross, Phys. Rev. Lett. 32, 1071 (1974).
[19]G. B. West, Ann. Phys. (N.Y.) 74, 464 (1972); W. B. Atwood and G. B. West, Phys. Rev. D 7, 773 (1973).
[20]A. Bodek, Ph.D. thesis, Massachusetts Institute of Technology, available as M.I.T. Report No. LNS-COO-3069-116, 1972 (unpublished).
[21]C. G. Callan and D. J. Gross, Phys. Rev. Lett. 22, 156 (1969).
[22]K. T. Mahanthappa and Tsu Yao, Phys. Lett. 39B, 549 (1972); J. E. Mandula, Phys. Rev. D 8, 328 (1973).
[23]J. F. Gunion and R. L. Jaffe, Phys. Rev. D 8, 3215 (1973).
[24]Previously reported in A. Bodek *et al.*, Phys. Rev. Lett. 30, 1087 (1973); E. M. Riordan *et al.*, *ibid.* 33, 561 (1974); and E. M. Riordan *et al.*, Phys. Lett. 52B, 249 (1974); see also Refs. 20 and 26.
[25]A. Bodek *et al.*, Phys. Lett. 51B, 417 (1974).
[26]E. M. Riordan, Ph.D. thesis, Massachusetts Institute of Technology, available as M.I.T. Report No. LNS-COO-3069-176, 1973 (unpublished).
[27]Reference 8. For a complete listing of cross sections as well as more detail, see J. S. Poucher *et al.*, Stanford Linear Accelerator Report No. SLAC-PUB-1309 (unpublished); J. S. Poucher, Ph.D. thesis, Massachusetts Institute of Technology, 1971 (unpublished).
[28]The 6 and 10 degree inelastic *e-p* and *e-d* measurements were made by a collaboration of physicists from MIT and SLAC Group A. The members of that collaboration are the authors of Ref. 8.
[29]P. N. Kirk *et al.*, Phys. Rev. D 8, 63 (1973); D. H. Coward *et al.*, Phys. Rev. Lett. 20, 292 (1968); see also Ref. 40.
[30]R. B. Neal, *The Stanford Two-Mile Accelerator* (Benjamin, New York, 1968).
[31]R. S. Larsen and D. Horelick, in *Proceedings of the Symposium on Beam Intensity Measurements, Daresbury, 1968,* edited by V. W. Horton and S. A. Lowndes (Daresbury Nuclear Physics Laboratory, Daresbury, Lancashire, England, 1968); also available as Stanford Linear Accelerator Center Report No. SLAC-PUB-398, 1968 (unpublished).
[32]D. Yount, Nucl. Instrum. Methods 52, 1 (1967).
[33]J. W. Mark and W. B. Pierce, IEEE Trans. Nucl. Sci. NS-18, 806 (1971).
[34]R. Anderson *et al.*, Nucl. Instrum. Methods 66, 328 (1968); J. R. Johnson, Stanford Linear Accelerator Center Report No. SLAC-PUB-124, 1970 (unpublished).
[35]Bubble Chamber Group Selected Cryogenic Data Notebook, compiled by J. R. Jensen *et al.*, Brookhaven National Laboratory Report No. BNL-10200, 1966 (unpublished).
[36]H. W. Wooley *et al.*, J. Res. Natl. Bur. Stand. (U.S.) 41, 379 (1948).
[37]A. Bodek, Nucl. Instrum. Methods 109, 603 (1973).
[38]K. L. Brown, Stanford Linear Accelerator Report No. SLAC-PUB-75, 1967 (unpublished).
[39]L. Mo and C. P. Peck, Stanford Linear Accelerator Center Report No. SLAC-TN-65-29, 1965 (unpublished).
[40]P. N. Kirk, Ph.D. thesis, Massachusetts Institute of Technology, 1968 (unpublished).
[41]G. Miller, Ph.D. thesis, Stanford University, 1970, available as Stanford Linear Accelerator Center Report No. SLAC-PUB-129, 1971 (unpublished).
[42]L. C. Maximon, Rev. Mod. Phys. 41, 193 (1969).
[43]L. W. Mo and Y. S. Tsai, Rev. Mod. Phys. 41, 205 (1969).
[44]Y. S. Tsai, in *Proceedings of the International Conference on Nuclear Structure, 1963,* edited by R. Hofstadter and L. I. Schiff (Stanford University Press, Stanford, California, 1964), p. 221; see also Y. S. Tsai, Stanford Linear Accelerator Center Report No. SLAC-PUB-848, 1971 (unpublished) and Ref. 45.
[45]Y. S. Tsai, Phys. Rev. 122, 1898 (1961).
[46]M. Breidenbach, Ph.D. thesis, Massachusetts Institute of Technology, 1969, available as M.I.T. Report No. LNS-MIT-2098-635, 1970 (unpublished).
[47]From Particle Data Group, Phys. Lett. 50B, 1 (1974).
[48]T. Hamada and J. D. Johnston, Nucl. Phys. 34, 382 (1962).
[49]J. Elias *et al.*, Phys. Rev. 177, 2075 (1969).
[50]M. Sogard, Ph.D. thesis, Massachusetts Institute of Technology, 1970 (unpublished).
[51]M. N. Rosenbluth, Phys. Rev. 79, 615 (1950).
[52]L. Durand III, Phys. Rev. 115, 1020 (1959); also 123, 1393 (1961).
[53]R. Wilson, in *Proceedings of the 1971 International Symposium on Electron and Photon Interactions at High Energies, Cornell, 1971,* edited by N. B. Mistry (Laboratory of Nuclear Studies, Cornell University, Ithaca, New York, 1972); see also Ref. 3.
[54]E. A. Allton, Phys. Rev. 135B, 570 (1964).
[55]J. D. Bjorken, Ann. Phys. (N.Y.) 24, 201 (1963).
[56]C. Jordan and M. Mestayer, private communications.
[57]S. Hartwig *et al.*, Lett. Nuovo Cimento 12, 30 (1975) and references therein. See also N. Meister and D. R. Yennie, Phys. Rev. 130, 1210 (1973).
[58]L. Rochester *et al.*, Phys. Rev. Lett. 36, 1284 (1976).
[59]S. Stein *et al.*, Stanford Linear Accelerator Report No. SLAC-PUB-1528, 1975 (unpublished) and Phys. Rev. D 12, 1884 (1975).
[60]W. B. Atwood and S. Stein, private communications; see also Ref. 61.
[61]A form similar to that used by Atwood and Stein was first proposed by M. Breidenbach and J. Kuti, Phys. Lett. 41B, 345 (1972).
[62]V. Rittenberg and H. R. Rubinstein, Phys. Lett. 35B, 501 (1972); see also Ref. 76.
[63]A. Bodek, Phys. Rev. D 8, 2331 (1973).
[64]A. Bodek, Nucl. Instrum. Methods 117, 613 (1974); see also A. Bodek, Stanford Linear Accelerator

Center Report No. SLAC-TN-74-2, 1974 (unpublished).
[65]R. V. Reid, Jr., Ann. Phys. (N.Y.) 50, 411 (1968); H. Feshbach and E. Lomon, *ibid.* 29, 19 (1964); L. Hulthén and M. Sugawara, in *Handbuch der Physik*, edited by S. Flügge (Springer, Berlin, 1957), Vol. 39, p. 1.
[66]A quadrupole magnet in the 20-GeV spectrometer had been slightly askew during the 6° measurements of experiment C. A correction of θ to account for this skewing changed the scattering angle from 6.000° to 5.988°, but the uncertainty in this procedure was too severe to permit use of the 6° elastic e-p cross sections in the calculation of the normalization factor. E. Bloom and J. S. Poucher, private communication.
[67]J. J. Sakurai, Phys. Rev. Lett. 30, 245 (1973).
[68]For a review of ρ electroproduction data, see the talk by K. Berkelman, in *Proceedings of the Sixteenth International Conference on High Energy Physics, 1972*, edited by J. D. Jackson and A. Roberts (National Accelerator Laboratory, Batavia, Ill., 1973), Vol. 4, p. 41.
[69]R. Jaffe, private communication.
[70]D. V. Nanopoulos and G. G. Ross, Phys. Lett. 58B, 105 (1975).
[71]T. Eichten *et al.*, Phys. Lett. 46B, 274 (1973).
[72]M. K. Gaillard and B. W. Lee, Rev. Mod. Phys. 47, 277 (1975).
[73]G. C. Fox, in *Neutrino – 78*, proceedings of the International Conference on Neutrino Physics and Astrophysics, Purdue University, edited by E. C. Fowler (Purdue Univ., West Lafayette, Indiana, 1978); I. Hinchliffe and C. H. Llewellyn Smith, Nucl. Phys. B128, 93 (1977).
[74]E. D. Bloom and F. J. Gilman, Phys. Rev. D 4, 2901 (1971).
[75]F. W. Brasse *et al.*, Nucl. Phys. B39, 421 (1972).
[76]W. B. Atwood, Ph.D. thesis, Stanford University, available as Stanford Linear Accelerator Center Report No. SLAC-PUB-185, 1975 (unpublished); and W. B. Atwood *et al.*, Phys. Rev. Lett. 64B, 479 (1976).
[77]See Ref. 17 and also Wu-Ki Tung, Phys. Rev. Lett. 35, 490 (1975); Phys. Rev. D 12, 3613 (1975).
[78]T. D. Lee, Phys. Today 25 (No. 4), 23 (1972); also CERN Report No. 73-15, 1973 (unpublished).
[79]For example, the behavior of R_n at the position of the elastic peak is expected from local-duality arguments to be $R_N \to (4M^2/Q^2)\ (G_E^2/G_M^2) = 0$ if $G_E^2(Q^2) = 0$. See Refs. 23 and 74. Similar arguments could be made for R_N at values of W close to the resonance region.
[80]J. Schwinger, Proc. Natl. Acad. Sci. U.S.A. 72, 1 (1975).
[81]C. Chang *et al.*, Phys. Rev. Lett. 35, 901 (1975).
[82]H. L. Anderson *et al.*, Phys. Rev. Lett. 38, 1450 (1977).
[83]B. A. Gordon *et al.*, Phys. Rev. Lett. 41, 615 (1978).
[84]R. C. Ball *et al.*, Phys. Rev. Lett. 42, 866 (1979).
[85]I. Karliner and J. D. Sullivan, Phys. Rev. 18, 3202 (1978).
[86]See especially G. C. Fox, Ref. 73, for an extensive discussion.
[87]H. L. Anderson *et al.*, Phys. Rev. Lett. 40, 1061 (1978).
[88]K. L. Brown, SLAC Report No. SLAC-75, 1967 (unpublished).
[89]C. Jordan, private communication.
[90]D. H. Coward, private communication.
[91]E. Taylor, private communication.
[92]D. H. Coward and G. C. Hartman, SLAC Group A Internal Report, 1968 (unpublished).
[93]J. I. Friedman, private communication.
[94]R. A. Early, private communication; see also R. A. Early, Nucl. Instrum. Methods 109, 93 (1973).
[95]M. N. Rosenbluth, Phys. Rev. 79, 615 (1956).
[96]M. R. Sogard, Ph.D. thesis, Massachusetts Institute of Technology, 1970 (unpublished).
[97]L. Eyges, Phys. Rev. 76, 264 (1949); also 77, 81 (1950).
[98]H. Bethe and J. Ashkin, in *Experimental Nuclear Physics*, edited by E. Segrè (Wiley, New York, 1953).
[99]R. J. Glauber, Phys. Rev. 100, 242 (1955); V. Franco and R. J. Glauber, *ibid.* 142, 1195 (1966).
[100]W. R. Ditzler, Ph.D. thesis, Massachusetts Institute of Technology, 1972 (unpublished). See also S. Stein *et al.*, Phys. Rev. D 12, 1884 (1975); and J. Eickmeyer *et al.*, Phys. Rev. Lett. 36, 289 (1976).
[101]S. J. Brodsky and J. Pumplin, Phys. Rev. 182, 1794 (1969).
[102]D. Schildknecht, Nucl. Phys. B66, 398 (1973).
[103]J. E. Elias, Ph.D. thesis, Massachusetts Institute of Technology, 1970 (unpublished).
[104]I. J. McGee, Phys. Rev. 158, 1500 (1967); 161, 1640 (1967).
[105]F. H. Renard, J. Tran Thanh Van, and M. Le Bellac, Nuovo Cimento 38, 552 (1965); 38, 565 (1965); 38, 1688 (1965).
[106]G. Alberi, M. A. Gregorio, and Z. D. Thome, Phys. Lett. 45B, 490 (1973).
[107]L. I. Frankfurt and M. I. Strickman, Phys. Lett. 65B, 51 (1976); also Leningrad Nuclear Physics Institute Report No. 238, 1976 (unpublished) and Report No. 173, 1975 (unpublished).
[108]P. V. Landshoff and J. C. Polkinghorne, Phys. Rev. D 18, 153 (1978).